

# Force-, Heat- and Electron-Induced Switching of Single Molecules on Metal Surfaces

Tautomerization of Porphycene  
Investigated with Scanning Probe Microscopy

Im Fachbereich Physik  
der Freien Universität Berlin  
eingereichte Dissertation

**Janina N. Ladenthin**

Oktober 2016





Diese Arbeit entstand zwischen Juli 2013 und Oktober 2016 in der Arbeitsgruppe von Dr. Takashi Kumagai in der Abteilung Physikalische Chemie des Fritz-Haber-Instituts der Max-Planck-Gesellschaft unter der Betreuung von Prof. Dr. Martin Wolf.

Erstgutachter: Prof. Dr. Martin Wolf

Zweitgutachterin: Prof. Dr. Katharina J. Franke

Datum der Disputation: 19.12.2016

---

---

## Abstract

In this thesis, single-molecule tautomerization on metal surfaces are studied. Tautomerization is a structural conversion between two or more isomeric forms of a molecule. Tautomerization is related to many important chemical and biological processes and combined studies of spectroscopic experiments with quantum chemical calculations have provided detailed insights into the correlation between a molecular structure and tautomerization dynamics for an isolated molecule, but the study on single-molecule tautomerization in condensed phase where the local environment could have a crucial impact has been scarce so far. In this research low-temperature scanning probe microscopy is used to investigate the tautomerization of single porphycene molecules on copper surfaces. Porphycene is a structural isomer of porphyrin with similar chemical properties but relatively strong hydrogen bonds in the inner cavity, which makes this molecule an intriguing model for studying hydrogen bond dynamics. Using scanning tunneling microscopy (STM) and atomic force microscopy (AFM) the thermally-, electron-, and force-induced tautomerization of porphycene on copper surfaces were investigated and the mechanisms of the tautomerization processes were elucidated at the single-molecule level.

On the Cu(111) surface the hot carrier-induced *trans* to *cis* tautomerization and the thermally induced backward reaction were investigated with an STM. The hot carrier-induced process was observed not only in molecules underneath the STM tip, but also in molecules in a distance of up to 100 nm away from the tip. This nonlocal reaction is rationalized by traveling hot carriers along the surface and a more efficient transportation occurs for hot electrons traveling through the surface state than for hot holes. Additionally, a coupling between the surface state and the molecular adsorption was found to lead to a characteristic coverage dependence of the nonlocal tautomerization efficiency.

On the Cu(110) surface the force-induced *cis* to *cis* tautomerization was investigated with AFM. The reaction was induced merely by bringing the tip closer to a molecule, suggesting that the interaction between the tip apex and the molecule triggers the process. Force spectroscopy revealed the force needed to induce the tautomerization and quantified a fraction of nano-Newton. Density functional theory simulations revealed that the tip proximity distorts the potential landscape along the tautomerization coordinate and significantly reduces the activation barrier. It was found that the tautomerization could not be induced by a Xe terminated tip, demonstrating the importance of the chemical nature of the tip to trigger the reaction via the distortion of the potential landscape.

---

---

## Kurzfassung

In dieser Arbeit wird die Tautomerisierung einzelner Moleküle auf Metalloberflächen untersucht. Tautomerisierung ist eine strukturelle Anpassung zwischen zwei oder mehr Isomeren eines Moleküls und ist in vielen wichtigen chemischen und biologischen Prozessen involviert. Spektroskopische Experimente und quantenchemische Rechnungen lieferten einen detaillierten Einblick in die Zusammenhänge zwischen der Molekülstruktur und der Dynamik der Tautomerisierung eines isolierten Moleküls. Bisher gibt es jedoch nur wenige Untersuchungen der Tautomerisierung von einzelnen Molekülen in der kondensierten Phase, wobei hier die lokale Umgebung einen entscheidenden Einfluss haben kann. In dieser Arbeit wird Tieftemperatur-Rastersondenmikroskopie angewendet, um die Tautomerisierung von einzelnen Porphycenmolekülen auf Kupferoberflächen zu erforschen. Porphycen ist ein Isomer von Porphyrin mit ähnlichen chemischen Eigenschaften, aber relativ starken Wasserstoffbrückenbindungen im Inneren des Moleküls, die Porphycen zu einem interessanten Modell für die Dynamik von Wasserstoffbrückenbindungen machen. Die temperatur-, elektronen- und kraftinduzierte Tautomerisierung sowie die zugrundeliegenden Mechanismen wurden mit Rastertunnelmikroskopie (STM) und Rasterkraftmikroskopie (AFM) untersucht.

Die *trans* zu *cis* Tautomerisierung durch heiße Ladungsträger und die thermisch induzierte Rückreaktion wurden auf der Cu(111) Oberfläche mit STM erforscht. Der durch heiße Ladungsträger induzierte Prozess wurde nicht nur unter der STM Spitze beobachtet, sondern auch in Molekülen bis zu 100 nm weit entfernt. Diese nichtlokale Reaktion kann durch die Fortbewegung heißer Ladungsträger entlang der Oberfläche erklärt werden. Elektronen bewegen sich dabei effizienter fort als Löcher, indem sie den Cu(111)-Oberflächenzustand nutzen. Zusätzlich wurde eine Wechselwirkung zwischen dem Oberflächenzustand und der Adsorption der Moleküle nachgewiesen, die zu einer Abhängigkeit der nichtlokalen Tautomerisierungseffizienz von der Molekülbedeckung führt.

Die kraftinduzierte *cis* zu *cis* Tautomerisierung wurde mit AFM auf Cu(110) untersucht. Die Reaktion wurde ausschließlich von der Annäherung der Spitze hervorgerufen, was die Wechselwirkung zwischen Spitze und Molekül als Auslöser nahelegt. Kraftspektroskopie ermittelte die zum Auslösen der Reaktion benötigte Kraft auf einen Bruchteil von Nanonewton. Dichtefunktionaltheorie-Simulationen zeigten, dass die Spitze die Potentiallandschaft entlang der Tautomerisierungscoordinate deformiert und die Aktivierungsbarriere erheblich reduziert. Die Tautomerisierung kann nicht durch ein Xenonatom an der Spitze ausgelöst werden, wodurch die Bedeutung der chemischen Reaktivität der Spitze demonstriert wird.

---

---

## List of abbreviations

**AFM** Atomic Force Microscope / Atomic Force Microscopy

**CPD** Contact Potential Difference

**DFT** Density Functional Theory

**DOS** Density of States

**HOMO** Highest Occupied Molecular Orbital

**IETS** Inelastic Electron Tunneling Spectroscopy

**LDOS** Local Density of States

**LUMO** Lowest Unoccupied Molecular Orbital

**LT-STM** low-temperature Scanning Tunneling Microscope

**MEP** Minimum Energy Path

**NC-AFM** non-contact Atomic Force Microscopy

**NEB** Nudge Elastic Band

**STM** Scanning Tunneling Microscope / Scanning Tunneling Microscopy

**STS** Scanning Tunneling Spectroscopy

**ZPE** Zero Point Energy

---



# Contents

<b>Abstract</b>	<b>v</b>
<b>Kurzfassung</b>	<b>vii</b>
<b>List of abbreviations</b>	<b>ix</b>
<b>1 Introduction</b>	<b>1</b>
<b>2 Study of single-molecule tautomerization on surfaces</b>	<b>5</b>
2.1 Tautomerization in a single-molecule studied by LT-STM . . . . .	5
2.1.1 Tautomerization . . . . .	5
2.1.2 Tautomerization as single molecular switch . . . . .	6
2.1.3 Naphthalocyanine on a NaCl bilayer on Cu(111) . . . . .	7
2.1.4 Phthalocyanine on Ag(111) . . . . .	7
2.1.5 Porphyrin derivative on Ag(111) . . . . .	9
2.2 Porphycene - model for hydrogen atom transfer via hydrogen bonds	11
2.3 Porphycene tautomerization on Cu(110) studied by LT-STM . . .	13
2.3.1 Vibrationally induced tautomerization via inelastic electron tunneling . . . . .	14
2.3.2 Thermally induced tautomerization . . . . .	16
2.3.3 Control of tautomerization by STM manipulation . . . . .	16
<b>3 Scanning Probe Microscopy (SPM) Techniques</b>	<b>19</b>
3.1 Scanning Probe Microscopy (SPM) . . . . .	19
3.2 Scanning Tunneling Microscopy (STM) . . . . .	20
3.2.1 Working principle of an STM . . . . .	20
3.2.2 Tunneling model of Tersoff and Hamann . . . . .	21
3.2.3 Scanning Tunneling Spectroscopy (STS) . . . . .	23
3.2.4 Inelastic Electron Tunneling Spectroscopy (IETS) . . . . .	25
3.3 Atomic Force Microscopy (AFM) . . . . .	27

3.3.1	Working principle of an AFM . . . . .	27
3.3.2	Forces in AFM . . . . .	27
3.3.3	Chemical forces - Morse potential model . . . . .	28
3.3.4	Van der Waals forces - London dispersion force . . . . .	28
3.3.5	Operation modes - static and dynamic AFM . . . . .	29
3.3.6	Non-contact AFM (NC-AFM) . . . . .	30
3.3.7	Sader Jarvis Method . . . . .	31
3.3.8	Electrostatic forces and Contact Potential Difference (CPD) . . . . .	32
3.4	Experimental setup . . . . .	35
3.4.1	Setup of the UHV chambers . . . . .	35
3.4.2	SPM head . . . . .	37
3.4.3	SPM tips . . . . .	38
3.4.4	AFM setup with the $q^+$ -sensor . . . . .	39
3.4.5	Sample preparation . . . . .	40
<b>4</b>	<b>Hot carrier-induced tautomerization</b>	<b>41</b>
4.1	Introduction . . . . .	42
4.1.1	Nonlocal reactions induced by STM . . . . .	42
4.1.2	Hot carrier-induced reactions on metal surfaces . . . . .	42
4.1.3	Influence of the surface state on adsorbed molecules and vice versa . . . . .	43
4.1.4	Motivation for Cu(111) as metal substrate . . . . .	44
4.2	Porphycene on a Cu(111) surface . . . . .	45
4.3	Vibrationally induced tautomerization of porphycene . . . . .	46
4.4	Thermally induced tautomerization of porphycene . . . . .	48
4.5	Hot carrier-induced nonlocal tautomerization . . . . .	49
4.5.1	Tautomerization next to step edges . . . . .	51
4.5.2	Tautomerization induced through conductive clusters . . . . .	52
4.5.3	Tip-sample distance dependence of the tautomerization . . . . .	54
4.5.4	Efficient hot carrier transport through the surface state . . . . .	54
4.6	Coverage dependence of the nonlocal tautomerization . . . . .	56
4.7	Summary . . . . .	61
<b>5</b>	<b>Force-induced tautomerization in a single molecule</b>	<b>63</b>
5.1	Introduction . . . . .	64
5.1.1	Mechanochemistry . . . . .	64
5.1.2	Atomic scale force detection with AFM . . . . .	66
5.1.3	Model system for force-induced tautomerization . . . . .	67

---

5.2	Force-induced <i>cis</i> to <i>cis</i> tautomerization . . . . .	68
5.2.1	Reproducibility of the tautomerization spectra . . . . .	71
5.2.2	Influence of small bias voltage and tunneling current on the tautomerization . . . . .	72
5.2.3	Effect of long-range electrostatic force on the tautomerization	74
5.3	Force map of porphycene . . . . .	75
5.3.1	Position adjustment of the force map . . . . .	77
5.4	Potential curves in position dependence . . . . .	79
5.5	Xe terminated tip . . . . .	81
5.6	DFT calculations of porphycene . . . . .	83
5.7	Mechanism of the force-induced tautomerization . . . . .	85
5.7.1	Importance of the NH bond . . . . .	85
5.7.2	Minimum energy path (MEP) . . . . .	87
5.8	DFT calculations with a Xe terminated tip . . . . .	91
5.9	Summary . . . . .	93
<b>6</b>	<b>Summary and Outlook</b>	<b>95</b>
	<b>Bibliography</b>	<b>99</b>
	<b>Publications</b>	<b>115</b>
	<b>Presentations</b>	<b>116</b>
	<b>Acknowledgments</b>	<b>119</b>



# Chapter 1

## Introduction

This thesis investigates tautomerization, a conformational switching of a molecule through transfer of atom(s) within the molecule. The most common form of tautomerization involves transfer of hydrogen atom(s) between different binding sites within the molecule such as keto  $\leftrightarrow$  enol and imine  $\leftrightarrow$  amine transformations. Upon tautomerization the molecules change not only the structure but also the properties. For instance, tautomerization can reversibly change the color of a molecule depending on their environment, as for example the acidity of a solution, because different tautomeric forms may exhibit different electronic states [1]. Tautomerization has been a long-standing research topic as it can be found in the pioneering work by Claisen in the late 19th century [2] and plays an important role in chemistry and biology [3, 4]. Tautomerization is associated to chromism and important biological processes as the binding to other molecules could be influenced by tautomeric states and a biologically active molecule cannot be connected to a specific receptor in the worst case. Therefore, tautomerization is under investigation to cause the presence of mutagenic transformations of the DNA [5–10] and plays a crucial role in pharmaceutical drug design [11–15].

Tautomerization has been studied intensively in the gas phase, in solution, and in the solid state with spectroscopic methods such as rotational-vibrational spectroscopy [16, 17], fluorescence spectroscopy [16, 18], and nuclear magnetic resonance spectroscopy [19]. Although these studies have provided quantitative insights into the tautomeric structure and tautomerization dynamics, the influence of the local environment on the tautomeric state remains poorly understood at the single-molecule level. In this thesis tautomerization on a surface is studied with SPM. The local probing capability of an SPM allows us to directly study tautomerization within a single molecule.

In recent years switching of single molecules on surfaces has attracted increasing attention in the field of nanotechnology as a switch in molecular devices in which individual molecules act as function unit [20]. Tautomerization could be one of the promising candidates for such a switching module, but tautomerization behavior in molecules anchored on surfaces was not explored in detail. Recently, STM has been used to investigate single-molecule tautomerization on surfaces [21–25]. Free-base naphthalocyanine [21], phthalocyanine [22], and a porphyrin derivative [23] have been reversibly switched between different tautomeric forms. The molecule studied in this thesis is porphycene, which is a structural isomer of porphyrin. Porphycene and porphyrin exhibit similar chemical properties [26], but a rectangular inner cavity of porphycene results in the formation of strong hydrogen bonds, which lead to a reduced tautomerization barrier and a faster tautomerization rate [27] compared to porphyrin [28]. Recent STM studies of porphycene on Cu(110) showed a vibrationally and thermally induced reversible *cis* to *cis* tautomerization with an activation barrier of about 170 meV [24]. Furthermore, by placing an adatom at different positions nearby a single porphycene molecule the tautomerization rate could be modified in a controlled way [25], demonstrating a crucial impact of the local environment on the process at the atomic scale.

In this thesis the influence of the local environment on the tautomerization behavior will be studied further and two additional excitation mechanisms will be introduced: the nonlocal hot carrier-induced tautomerization and the force-induced tautomerization. In the nonlocal excitation, reactions can be induced very efficiently in areas up to tens of nm away from the STM tip. This will be beneficial in future applications to operate molecular switches at the same time within a defined local area. A hot carrier-induced reaction is also related to other surface processes. For instance, a photochemical reaction on metal surfaces is induced through hot carrier generation followed by its attachment to adsorbates [29]. Therefore, a detailed knowledge of hot carrier-induced processes and the elucidation of environmental impacts will also contribute to the further understanding of photochemical reactions on metal surfaces. Although several studies on hot carrier-mediated reactions using STM have been reported [30–33], the role of the surface state in hot carrier transportation and the influence of the molecular coverage have not been investigated in detail. In this thesis the hot carrier induced tautomerization of porphycene is investigated on a Cu(111) surface that has a surface state above  $-0.4\text{ V}$  with respect to the Fermi level [34].

---

The second part of this thesis investigates the force-induced tautomerization of a single porphycene on Cu(110). The tuning of the tautomerization using an adatom manipulation nearby a porphycene molecule [25] implied the possibility to control the potential landscape of the tautomerization coordinate with a precision on the atomic scale. However, this raises the important questions - whether as an extreme case of manipulation, the modification of the atomic scale environment can induce a tautomerization and which interaction forces arise due to such a local change in the environment. An NC-AFM can investigate the interactions between the molecule and an approaching tip, whereby the tip simultaneously causes the modification of the potential landscape along the tautomerization coordinate.

The thesis consists of the following chapters:

**Chapter 2** introduces the porphycene molecule as a model system for tautomerization. A general introduction of tautomerization is followed by a description of previous studies of single-molecule tautomerization on surfaces using LT-STM and recent results of porphycene on Cu(110).

**Chapter 3** outlines the basic physical and experimental working principles of the STM and AFM and introduces the experimental set up.

**Chapter 4** describes the experimental results on the tautomerization of porphycene molecules on a Cu(111) surface. First, the vibrationally and thermally induced tautomerization of single porphycene molecules is discussed. Followed by the description of the nonlocal hot carrier-induced tautomerization of porphycene. Here, the influence between the molecular coverage and the surface state and vice versa and their effect to the hot carrier-induced tautomerization is investigated.

**Chapter 5** describes the force-induced tautomerization of a single porphycene molecule on a Cu(110) surface by an AFM tip. Detailed force spectroscopy measurements with sub-Ångström spatial resolution quantify the interaction forces between the tip and the molecule and reveal in combination with DFT simulations the mechanism of the force-induced tautomerization. Furthermore, a Xe terminated tip is used to investigate the importance of the chemical nature of the tip for the reaction.

**Chapter 6** summarizes the key findings of this thesis and gives an outlook.





## Chapter 2

# Study of single-molecule tautomerization on surfaces

### 2.1 Tautomerization in a single-molecule studied by LT-STM

#### 2.1.1 Tautomerization

Tautomerization is defined as the intramolecular transfer of atom(s) or functional group(s) to another isomer in an organic molecule, as special case of isomerism the two tautomers have different structural skeletons, electronic density distributions and chemical properties [3, 35]. Tautomerization usually appears very fast and reversible, leading to a very environment sensible equilibrium between the tautomers [3, 35]. The most common form of tautomerization is an intra molecular hydrogen atom transfer, the so-called prototropic tautomerization, which will be studied in the research in this thesis.

Tautomerization is an important process in chemistry and biology [3, 4] and has a long research history as can be seen by one of the pioneer works by Claisen in 1896 [2]. Tautomers have been named the "chameleons of chemistry" [3], a tautomer can adjust its chemical structure immediately in a new environment and back to its original state under the initial conditions, resulting in new chemical, biological and physical properties, which represent the fascinating possibilities of tautomerization. Furthermore, tautomerization is directly associated with chromism, as for example under new environmental conditions the color of a compound can be changed by the occupation of other electronic states, due to a modified HOMO-LUMO gap for a different tautomeric form. As the molecules

can react to different stimuli, for example, photochromism, thermochromism, and solvatochromism can be observed [1]. In biochemistry major and minor tautomers can have different biological properties, e.g. the ability to bind to a specific acceptor/receptor in a biological system. DNA for instance is build up from bases which have tautomeric forms and since the discovery of its structure, the possible influence of minor tautomers for mutagenic transformations of the DNA have been investigated [5–10]. Due to the importance of tautomerization for biochemical processes, it also plays a role in future pharmaceutical drug design [11]. In pharmaceutical drug research recent investigations revealed tautomerization as a factor for the effectiveness of the anti-HIV drug KP1212; by the use of multiple tautomeric forms the drug causes mutagenic transformations in the replication of the virus up to a level that causes a viral population collapse [14, 15].

### 2.1.2 Tautomerization as single molecular switch

Recently, tautomerization has gained increasing attention in nanoscale science as a single molecular switch. In order to use a single molecular switch as an electronic compound, it needs to be integrated into the electronic device [20]. The contact of a single molecule to a metallic nanoelectrode could be realized by STM atomic manipulation of single metal atoms to atomic chains, contacting the molecule [36] or by an STM tip induced on surface polymerization of nanowires [37, 38], which chemically bound to functional molecules [39]. To ensure a stable contact of the single molecular switch to the nanoelectrodes, the molecular frame should be preserved upon switching the molecule. In contrast to single molecular switches which drastically change their conformation, e.g. azobenzene [40], tautomerization opens the possibility for controlled, reversible and stable switching while maintaining the molecular frame. Recent theoretical simulations predict possible applications of single molecule tautomerization switches contacted to nanoelectrodes as on-off conductance switch [41, 42], negative differential resistance switch [43] or spin transport switch in a spin filtering device [44]. For the experimental realization of single molecule switching devices, the controlled tautomerization of single molecules in influence of their local environment is a key factor. And a first step towards the operation and design of single molecule switching devices would be a detailed knowledge about the possibility to observe and remotely induce single molecule tautomerization on surfaces. For these investigations LT-STM proved to be a good tool as recent experiments of free-base naphthalocyanine [21], phthalocyanine [22], and a porphyrin derivative [23] demonstrated.

### 2.1.3 Naphthalocyanine on a NaCl bilayer on Cu(111)

The first demonstration of single molecule tautomerization was shown by P. Liljeroth and co-workers for the reversible *trans-trans* tautomerization in naphthalocyanine (see figure 2.1a) on a NaCl bilayer (and ultra thin RbI and Xe layers) on Cu(111) [21]. The LUMO and HOMO of the molecule were observed by  $dI/dV$  spectroscopy at around  $0.8\text{ V}$  and  $-1.7\text{ V}$  (see figure 2.1b). As the ultra thin insulating layer of NaCl decouples the molecular orbitals from the underlaying metal substrate, the almost pristine molecular orbitals can be directly imaged by the STM at the corresponding bias voltage with a molecule functionalized STM tip (see figures 2.1c, d). The STM images were in good agreement with simulated images by DFT. The positions of the inner hydrogen atoms can be identified in the two fold symmetric STM image of the LUMO. As shown in figures 2.1d and 2.1e, the hydrogen atoms are located at the single-lobe sides and the nodal planes are observable at the bare nitrogen sides. The tautomerization can be induced by application of a bias voltage above the LUMO resonance with the STM tip above the molecule (see figures 2.1d, f); at voltages around the LUMO resonance the tautomerization could not be induced. A rotation of the molecule could be ruled out by successful switching of the molecule next to step edges and neighboring molecules. The current dependence of the switching revealed a one electron process and the tautomerization rate showed a nearly exponential voltage dependence (see figure 2.1h), but the detailed switching mechanism remains unclear.

### 2.1.4 Phthalocyanine on Ag(111)

Sperl and co-workers reported tautomerization of phthalocyanine (see figure 2.2a) on a metal Ag(111) surface [22]. The molecules show a two-fold symmetry with lower appearing ligands along the  $[1\bar{1}0]$  surface direction, indicating a saddle-shaped distortion of the molecule (see figure 2.2b). Reversible tautomerization can be induced by an STM voltage pulse above the center of the molecule with a threshold voltage of  $1.6\text{ V}$ , as shown in figures 2.2b and 2.2c. The molecule can be deprotonated by a voltage pulse above a threshold voltage of  $3\text{ V}$ , leaving a single H atom in the cavity (see figure 2.2d). This single H atom can be tautomerized by a voltage pulse above a threshold of  $2.5\text{ V}$  between two opposite positions (see figures 2.2d, e) but could not be switched to the two ligands along the  $[1\bar{1}0]$  surface direction.

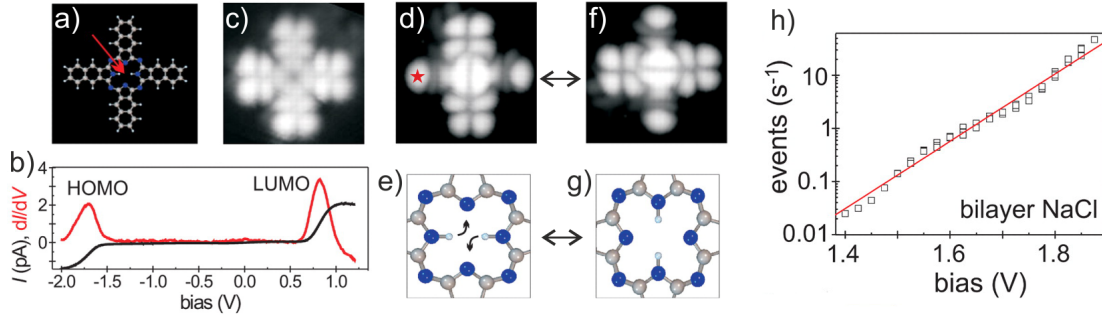


Figure 2.1: Naphthalocyanine on a NaCl bilayer on Cu(111). a) Structure model of the naphthalocyanine molecule (to scale with c, d and f). The arrow indicates the H atoms in the inner cavity which are along the horizontal arms. b) STS of the naphthalocyanine molecule. c, d) STM images of the HOMO at  $-1.6$  V (c) and LUMO at  $0.65$  V (d) measured with a molecule-terminated tip (current  $1$  pA). e) Structural model of the position of the inner cavity H atoms of d). f, g) STM image of the LUMO and structural model of the H atoms after the voltage pulse induced tautomerization. h) Voltage dependence of the tautomerization rate at a tunneling current of  $1$  pA fitted with an exponential slope of  $165$  mV/decade. (From Liljeroth *et al.* Science, 317:1203, 2007 [21]. Reprinted with permission from AAAS. Adapted with permission of the author.)

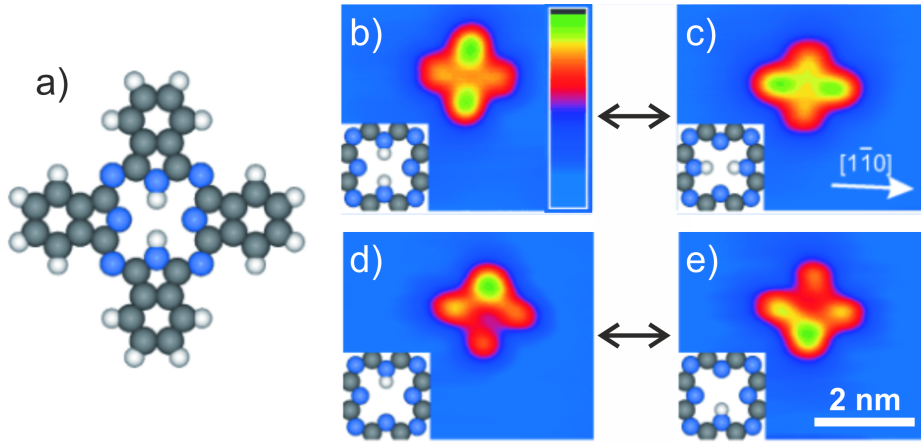


Figure 2.2: Phthalocyanine on Ag(111). a) Structural model of the phthalocyanine (Pc) molecule. b-e) STM images of the phthalocyanine molecule on Ag(111) at  $7$  K. The inner cavity H atoms are sketched in the structural models in the insets. b, c) The tautomerization of 2H-Pc can be induced by a voltage pulse of  $1.6$  V. d) STM image after deprotonation of 2H-Pc to 1H-Pc by a voltage pulse of  $3$  V. d, e) Tautomerization of 1H-Pc with a voltage pulse of  $2.5$  V. (Adapted from Sperl *et al.* [22] with permission from John Wiley and Sons.)

### 2.1.5 Porphyrin derivative on Ag(111)

Auwärter and co-workers showed the tautomerization of free-base tetraphenylporphyrin (2H-TPP) on a Ag(111) surface [23]. The macrocycle geometry of the molecule on the surface is determined by a saddle-shape with pairs of opposite pyrrole rings tilted upwards ( $\alpha$ -pyr) and downwards ( $\kappa$ -pyr), as shown in figures 2.3a and 2.3b. The H atoms in the inner cavity are located at opposite positions and can be tautomerized between the  $\alpha$ - and  $\kappa$ -pyrrole rings (see figures 2.3c, d). A rotation of the macrocycle can be excluded, as it would induce a rotation of the phenyl legs, which show stable appearance on high resolution STM images after switching the molecule. A deprotonation of the 2H-TPP to 1H-TPP could be induced by a voltage pulse of 2 V and the single H can be tautomerizes between

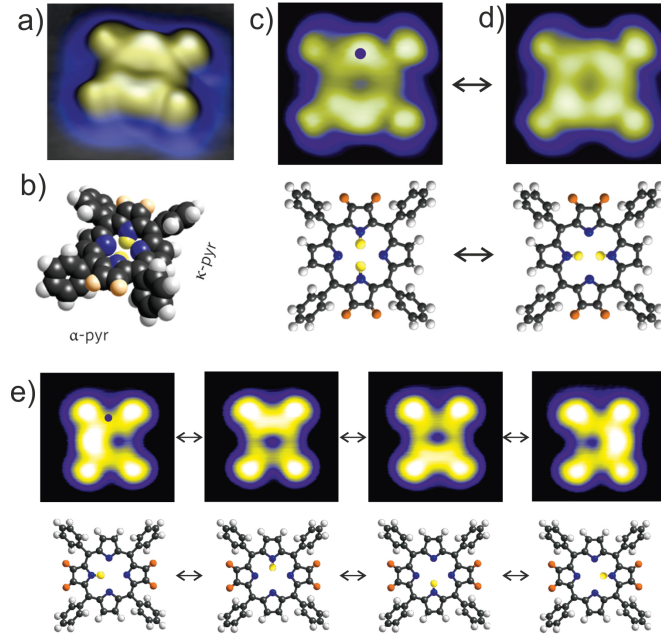


Figure 2.3: Tetraphenylporphyrin (TPP) on Ag(111). a) Pseudo three-dimensional high resolution STM image of 2H-TPP on the Ag(111) surface. b) Structural model of the adsorbed molecule. A saddle-shaped deformation results from the inequivalent pairs of pyrrole rings labeled as  $\alpha$ -pyrrole ( $\alpha$ -pyr) which are pointing away from the surface, marked in orange, and the  $\kappa$ -pyrrole ( $\kappa$ -pyr). c, d) STM images and structural models of the 2H-TPP molecule with the two inner cavity H atoms at the  $\alpha$ -pyrrole rings (c) and  $\kappa$ -pyrrole rings (d) (Image parameter:  $I = 0.1 \text{ nA}$ ;  $V = -0.2 \text{ V}$ ). e) STM images and structural models of the four possible states of the deprotonated 1H-TPP molecule with one inner cavity H atom. (Adapted by permission from Macmillan Publishers Ltd: Nature Nanotechnology [23], copyright 2012.)

the four states (see figure 2.3e), which can be observed as four conductance levels by placing the STM tip in an antisymmetric position above the molecule. The current and voltage dependence of the tautomerization rate of the 2H-TPP and deprotonated 1H-TPP was determined to get an insight into the mechanism. The current dependence exhibits a one-electron process (see figure 2.4a) and the voltage shows a symmetric dependence for positive and negative polarity and a threshold voltage of  $\pm 0.5$  V (see figure 2.4b), indicating an excitation of the tautomerization via an inelastic electron tunneling process. The tautomerization rates for the 2H-TPP and deprotonated 1H-TPP show the same characteristics, suggesting the same mechanism for both tautomerization processes, which would agree to a switching via an intermediate state for the two H atoms of the 2H-TPP.

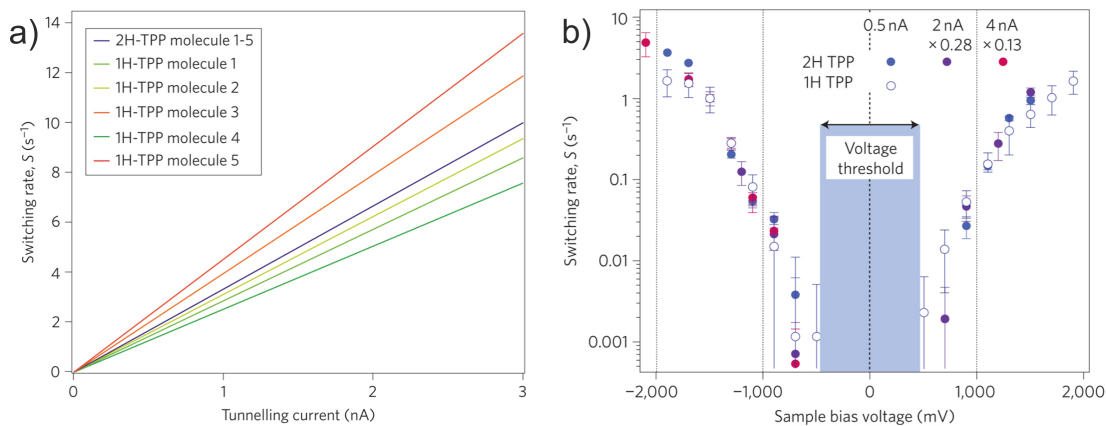


Figure 2.4: Current and voltage dependence of the tautomerization rate of TPP on Ag(111). a) Current dependence of the tautomerization rate for the 2H-TPP and five 1H-TPP molecules. b) Voltage dependence of the tautomerization rate for 2H-TPP and 1H-TPP. (Adapted by permission from Macmillan Publishers Ltd: Nature Nanotechnology [23], copyright 2012.)

## 2.2 Porphycene - model for hydrogen atom transfer via hydrogen bonds

Porphycene, see figure 2.5a, is a planar and aromatic molecule and a structural isomer of porphin (free-base porphyrin), see figure 2.5b, with comparable chemical properties [26]. In contrast to porphin, porphycene has a rectangular inner cavity leading to strong hydrogen bonds. Figure 2.5c and 2.5d depict structural sketches of the inner cavities of porphycene and porphin. In porphycene the rectangular cavity has dimensions of  $2.6 \times 2.8 \text{ \AA}$  [26], a NH bond length of  $1.1 \text{ \AA}$  and  $1.6 \text{ \AA}$  [45], and a very straight alignment of the  $\text{NH}\cdots\text{N}$  hydrogen bonded system with an bonding angle of  $152^\circ$  [45], resulting in strong hydrogen bonds in the inner cavity. These dimensions are very different in comparison to porphin, which has a  $2.9 \times 2.9 \text{ \AA}$  [46] square cavity with a NH bond lengths of  $1.0 \text{ \AA}$  and  $2.3 \text{ \AA}$  [45], and a hydrogen bond angle of  $116^\circ$  [45].

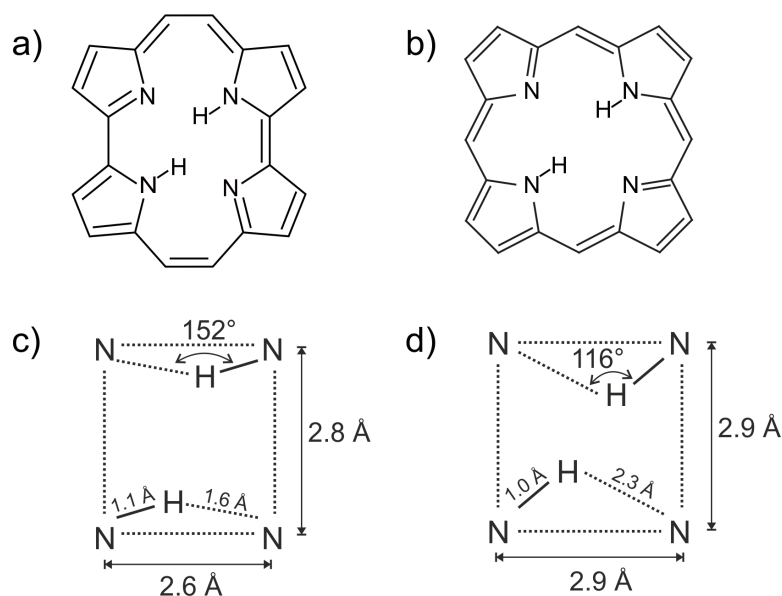


Figure 2.5: Chemical structure and inner cavity geometry of porphycene and porphin. a) Chemical structure of porphycene and b) porphin and schematically sketch of the inner cavity geometry of c) porphycene and d) porphin.

The porphycene can in principle exist in three different double degenerate arrangements of the two H atoms in the inner N cavity of the molecule, the so-called tautomers, tautomeric forms or states, as shown in figure 2.6. The H atoms can be located at opposite N atoms in the *trans* state (see figure 2.6a), or at neighboring N atoms in the *cis-1* and *cis-2* states (see figures 2.6b and c).

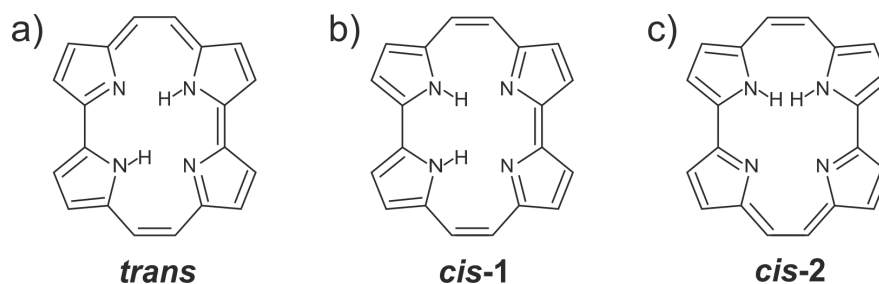


Figure 2.6: Porphycene tautomers. a) Porphycene in the *trans*, b) *cis-1* and c) *cis-2* tautomeric state.

In the gas phase the *trans* and *cis-1* state were calculated to have a comparable total energy with the *trans* state as energetically favorable [47,48]. Due to steric hindrances, the *cis-2* state has a much higher energy and can be considered as unstable [47,49]. Therefore, the *cis-1* tautomeric state will be referred to as *cis* state in the following of this thesis.

Porphycene has a rapid tautomerization rate of  $(5.8 \pm 0.3) \times 10^{11} \text{ s}^{-1}$  in ethylene glycol solution at a temperature of 293 K [27], which is a result of the strong H bonds in the inner cavity. In comparison, porphyrin has a tautomerization rate of around  $1 \times 10^4 \text{ s}^{-1}$  at 290 – 295 K [28]. Investigations of the tautomerization of porphycene derivatives have revealed that the H bond strength in the inner cavity is a dominant factor for determining the tautomerization rate [50]. These results confirm the importance of the H bond strength for the tautomerization rate and open the possibility to tune the tautomerization rate of porphycene by a distinct design of the inner cavity geometry and H bond strength in porphycene derivatives.



## 2.3 Porphycene tautomerization on Cu(110) studied by LT-STM

Previous studies in our research group by T. Kumagai and co-workers investigated porphycene molecules on a Cu(110) surface by LT-STM and DFT simulations [24, 25], which will be summarized in this section. On the Cu(110) surface, the porphycene molecules adsorb isolated (do not cluster or form islands) with the long molecular axis along the  $[\bar{1}\bar{1}0]$  surface direction and show a crescent-shaped protrusion in the STM image (see figure 2.7b), suggesting a *cis* tautomeric state (see figure 2.7a). DFT simulations reveal that the *cis* tautomer is energetically favorable adsorption state on the Cu(110) surface (see figure 2.7c-f), even though the *trans* tautomeric state is slightly favorable in the gas phase [47, 48]. The simulations show that the crescent of the protrusion results from the hydrogen atoms at this side of the molecular cavity.

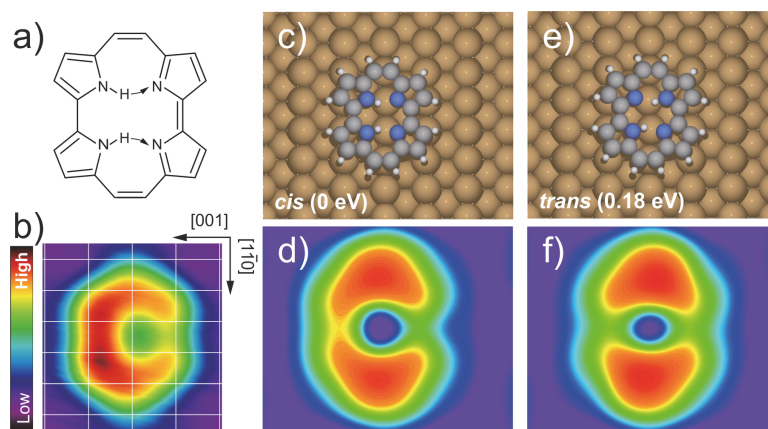


Figure 2.7: Porphycene on Cu(110) a) Chemical structure of the porphycene molecule. b) STM image of a single porphycene molecule on a Cu(110) surface at 5 K (image parameters:  $V = 100\text{ mV}$ ;  $I_t = 10\text{ nA}$ ; image size:  $1.49 \times 1.42\text{ nm}^2$ ). c) DFT simulated optimized structure of porphycene on Cu(110) - the *cis* tautomeric state. d) DFT simulated STM image of the structure in c). e) DFT simulated optimized *trans* tautomeric state of porphycene on Cu(110). f) DFT simulated STM image of the structure in e). (Adapted by permission from Macmillan Publishers Ltd: Nature Chemistry [25], copyright 2014.)

### 2.3.1 Vibrationally induced tautomerization via inelastic electron tunneling

At low bias voltages of around 50 to 100  $mV$ , the molecular protrusion is imaged static (see figure 2.8b), but at higher bias voltage as 190  $mV$  the STM image shows sudden contrast changes (see figure 2.8c); their amount increases with increasing bias voltage, leading to a fuzzy appearing porphycene molecule at 290  $mV$  (see figure 2.8d). The porphycene tautomerizes reversible between the two mirror symmetric *cis* tautomeric states (see figure 2.8a). A rotation of the molecule can be excluded as this tautomerization is also observed at step edges and next to neighboring molecules.

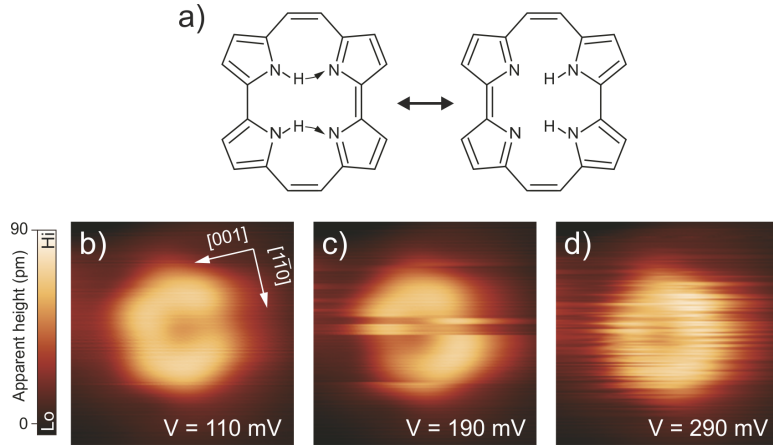


Figure 2.8: STM imaging of the *cis* to *cis* tautomerization. a) Chemical structure of the two degenerate *cis* tautomeric states. b-d) STM images of porphycene in voltage dependence. The sudden contrast changes in c) and d) correspond to the reversible *cis* to *cis* tautomerization during the image scan (image parameters: bias voltage is indicated in the images,  $I_t = 5 nA$ ; temperature:  $T = 5 K$ ; image size:  $2 \times 2 nm^2$  scan speed:  $9 s/image$ ). (Reprinted figure with permission from Kumagai *et al.*, Phys. Rev. Lett., 111:246101, 2013 [24]. Copyright 2013 by the American Physical Society. Adapted with permission of the author.)

The tautomerization can also be induced by applying a high bias voltage pulse over the porphycene molecule. The bias voltage dependence of the tautomerization rate shows a threshold voltage of around 150  $meV$  and symmetric voltage dependence for positive and negative bias voltages (see figure 2.9a) and the current  $I$  dependence of the tautomerization rate  $R$  follows the power law  $R \propto I^N$  with  $N$  the number of the electrons inducing the process (see figure 2.9b), suggesting an excitation of molecular vibrations via an inelastic electron tunneling process as origin of the tautomerization. For a vibration induced tautomeriza-

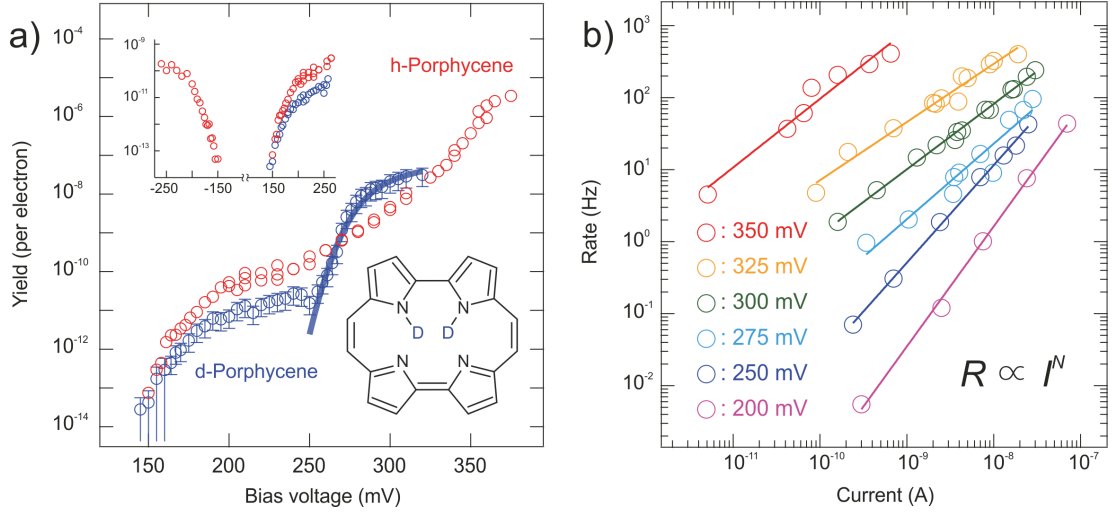


Figure 2.9: Vibrationally induced tautomerization. a) Voltage dependence of the tautomerization yield for h-porphycene and d-porphycene. b) Current dependence of the tautomerization yield for h-porphycene and d-porphycene. (Reprinted figure with permission from Kumagai *et al.*, Phys. Rev. Lett., 111:246101, 2013 [24]. Copyright 2013 by the American Physical Society. Adapted with permission of the author.)

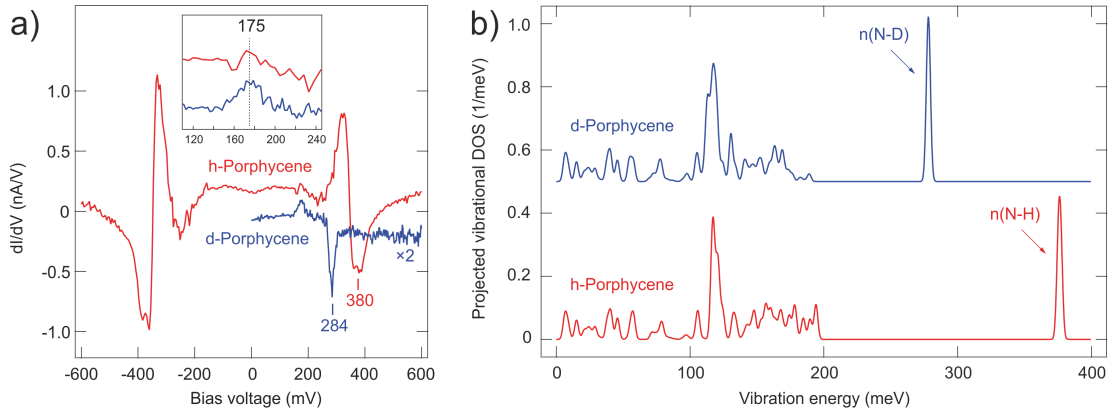


Figure 2.10: Vibration spectra of h-porphycene and d-porphycene. a)  $dI/dV$  spectra of h-porphycene and d-porphycene (Cu surface backward subtracted). b) Calculated projected density of states for h-porphycene and d-porphycene on Cu(110), the corresponding DFT optimized structure is shown in figure 2.7c. The displacements of the two inner cavity H atoms and the four N atoms are in-plane projected and the discrete vibrational modes Gaussian broadened by 2 meV. (Reprinted figure with permission from Kumagai *et al.*, Phys. Rev. Lett., 111:246101, 2013 [24]. Copyright 2013 by the American Physical Society. Adapted with permission of the author.)

tion a dependence on the isotope can be expected. Therefore, the hydrogen atoms in the molecular cavity were substituted by deuterium atoms and the voltage dependency of the d-porphycene was determined. For high bias voltages around  $250\text{ meV}$  to  $300\text{ meV}$  the d-porphycene tautomerization yield differs explicitly from the h-porphycene one (see figure 2.9a).

As shown in figure 2.10,  $dI/dV$  spectroscopy and calculated vibrational density of states reveal that the N-H and N-D stretching modes at an energy of around  $280\text{ meV}$  and isotope shifted at around  $380\text{ meV}$ , respectively, are the driving forces of the tautomerization in this bias voltage region. At bias voltages slightly above the tautomerization threshold of  $150\text{ meV}$ , no isotope shift can be identified (see figure 2.9a) and the tautomerization originates from a vibrational band around  $175\text{ meV}$  (see figure 2.10b), involving in-plane modes which are strongly coupled to out-of-plane motions of the molecular frame and do not exhibit a clear isotope dependence.

### 2.3.2 Thermally induced tautomerization

STM images at low bias voltage but higher temperatures as  $78\text{ K}$  and  $86\text{ K}$  (see figures 2.11a,b) show comparable features as STM images at bias voltages of  $190\text{ mV}$  and  $290\text{ mV}$  (see figures 2.8c,d), suggesting a thermal excitation of the *cis* to *cis* tautomerization. The purely thermal excitation of this tautomerization could be confirmed by the current independence of the tautomerization rate, as a non constant current dependency can be expected for a partially STM induced process. By fitting the temperature dependent tautomerization rate  $R$  to the Arrhenius equation ( $R \propto \exp(-E_a/k_B T)$ , with  $E_a$  the energy barrier,  $k_B$  the Boltzman constant, and  $T$  the temperature), as shown in figure 2.11c, the tautomerization barrier of  $168 \pm 12\text{ meV}$  can be determined for the double degenerate *cis* to *cis* tautomerization potential (see figure 2.11d). This energy stands in good agreement with the onset of the vibrationally induced tautomerization of around  $150\text{ meV}$ , suggesting an influence of the responsible in-plane vibrational band for the thermal and vibrationally induced process.

### 2.3.3 Control of tautomerization by STM manipulation

In absence of the tip, the *cis* to *cis* tautomeric states are degenerate and the barrier has a symmetric potential landscape. Occupation statistics of the two tautomeric states during tautomerization measurements with the tip positioned above the hydrogen atoms reveal that the presence of the tip lifts this degeneracy.

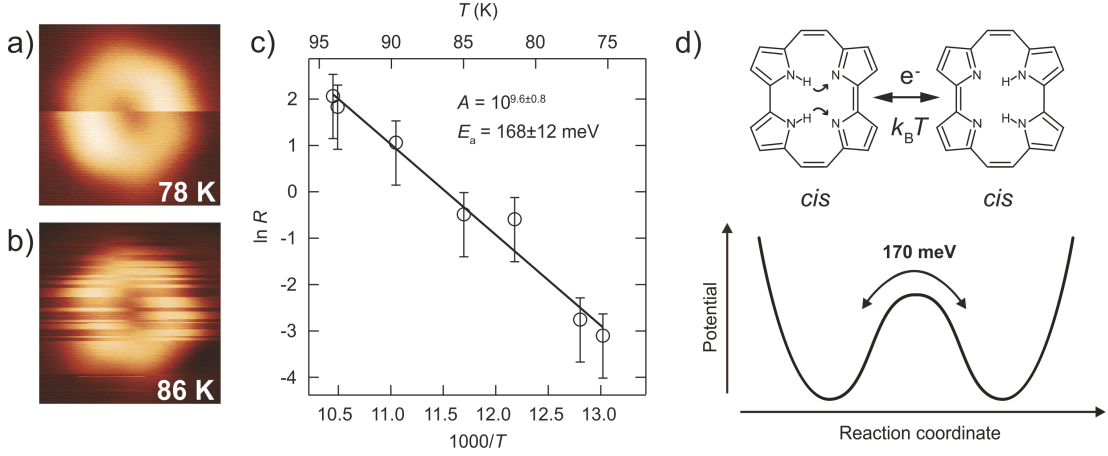


Figure 2.11: Thermal induced tautomerization. a,b) STM images at 78 K and 86 K, respectively. The sudden contrast changes correspond to reversible *cis* to *cis* tautomerization. c) Temperature dependence of the tautomerization rate with Arrhenius fit. d) Sketch of the degenerate *cis* to *cis* tautomerization potential landscape with an energy barrier  $E_a$  of  $168 \pm 12$  meV as determined by the Arrhenius fit of b). (Reprinted figure with permission from Kumagai *et al.*, Phys. Rev. Lett., 111:246101, 2013 [24]. Copyright 2013 by the American Physical Society. Adapted with permission of the author.)

For a voltage pulse of 300 mV at a fixed STM tip height (at a set point of 100 mV and 10 pA), the hydrogen atoms are with 40% probability positioned under the tip (high current) and 60% probability at the other side of the cavity (see (i) in figures 2.12a,b). That this is a pure effect of the antisymmetric tip positioning can be confirmed by inducing the voltage pulse at the center of the porphycene molecule (this leads to the disadvantage that the tautomeric state must be read out at a different position where the molecule has tautomerization dependent conductance). The occupation respectively the potential landscape of the tautomeric state can be tuned in a controlled way by manipulating an adatom next to the porphycene molecule. For an adatom positioned around 0.9 nm away from the molecule along the [001] surface axis, the *cis* state with the hydrogen atoms located at the cavity side closer to the adatom gets an increasing occupation (see (ii) in figures 2.12a,b) and for a very close adatom with around 0.5 nm distance to the molecule, the hydrogen atoms are energetically favorable at the opposite cavity side; then the adatom and the tautomerization gets quenched (see (iii) in figures 2.12a,b).

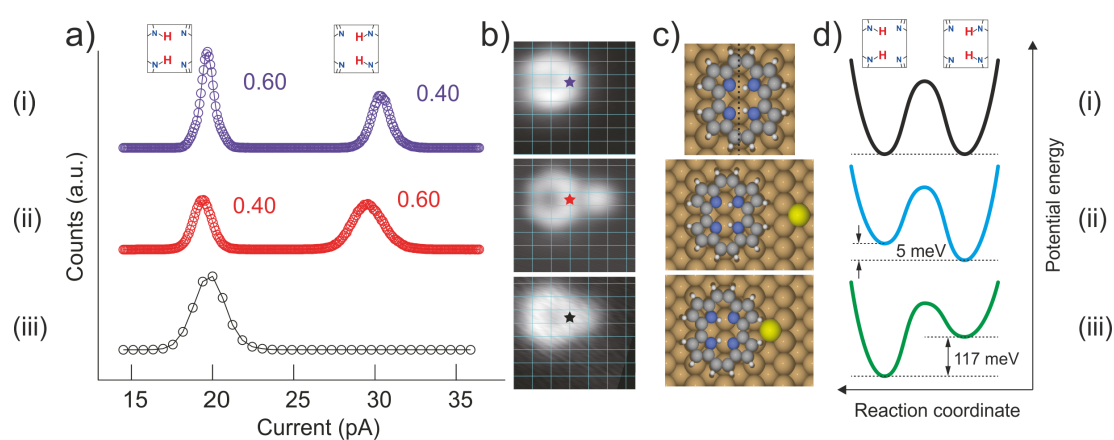


Figure 2.12: Controlled tautomerization tuning by adatom manipulation. a) Tautomerization state occupation measurement of the adatom set up (i) to (iii) in b). The high current state corresponds to a hydrogen atom cavity position under the STM tip. The presence and position of the adatom in (ii) and (iii) tune the occupation of the two *cis* tautomeric states. b, c) STM images and DFT optimized structures of the porphycene molecule and adatom setup. d) DFT calculated tautomerization barriers of the corresponding adatom positions in c) in absence of the tip. (Adapted by permission from Macmillan Publishers Ltd: Nature Chemistry [25], copyright 2014.)

## Chapter 3

# Scanning Probe Microscopy (SPM) Techniques

### 3.1 Scanning Probe Microscopy (SPM)

SPM started with the invention of the STM by Binnig and Rohrer in 1982 [51] and revolutionized the experimental possibilities of real space imaging on the atomic scale [52]. The basic concept of an SPM is the detection of the surface properties under an atomically sharp tip in a raster scanning manner across the surface giving a real space of the probe with atomic precision [53, 54]. Even though the scanning determined the name of the SPM family the results are not limited to the imaging capabilities of the SPM and a wide range of spectroscopic measurements are also possible at individual single positions on the surface [55, 56]. Another prominent application is the manipulation of atoms, molecules or the surface by the tip on the atomic scale [57–61]. Technical key aspects to realize such a system are a sophisticated vibrational damping and isolation of the scanning unit and the sample, an atomically precise motion of the tip, and in nearly all cases, the realization of an appropriate feedback mechanism to control the tip motion. The application range of SPMs is huge and determine the further requirements on a setup. SPMs are successfully operated in a vast range of environments as from ultrahigh vacuum to air and liquids as well as in a broad temperature range starting in the  $mK$  regime. The setup used in this thesis is a combined STM/AFM system operating in ultrahigh vacuum and at low temperatures around  $5\text{ K}$  allowing detailed investigations of tunneling electron- and force-induced processes on the atomic scale. This chapter gives

an introduction to the basic working principles, the operation modes, and the theoretical models describing the measurement principles of STM and AFM.

## 3.2 Scanning Tunneling Microscopy (STM)

### 3.2.1 Working principle of an STM

The STM uses quantum tunneling to investigate and image the surface of conductive samples with atomic resolution. The wave and particle nature of matter in quantum mechanics allows the tunneling of electrons through a barrier with a finite probability. In the STM this tunneling probability is used to quantify the local surface properties without direct contact between tip and sample. A bias voltage is applied between the tip and the sample, causing a tunneling current through the vacuum (or air) barrier, whereby the tunneling current depends very sensitively on the barrier thickness respectively the tip-sample distance and the density of states of tip and sample, as will be discussed in detail in the following sections.

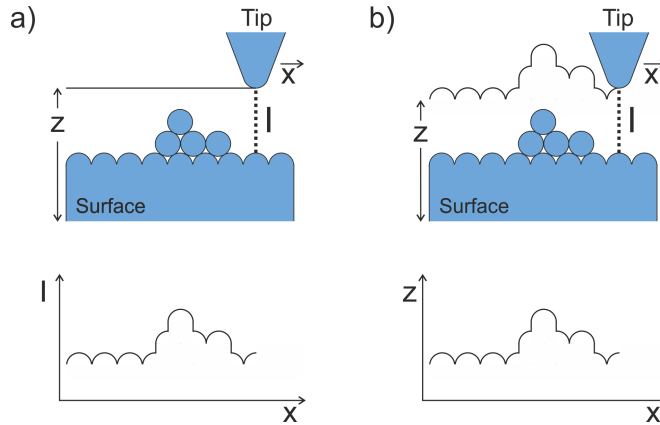


Figure 3.1: STM operation modes. a) In constant height mode, the STM tip scans the surface (scan direction  $x$ ) at a constant tip height  $z$  and the change in the tunneling current  $I$  is measured. b) In constant current mode, the tip height is regulated via a feedback loop to keep the tunneling current constant and the change in the tip height is detected.

The STM can be operated in constant height or constant current mode, see figure 3.1. In constant height mode, the STM tip is scanned at a given tip height over the surface and detects the tunneling current, as sketched in figure 3.1a. This operation mode does not require a feedback mechanism which allows a fast scanning speed but increases the risk of a collision between tip and sample at



atomic steps or adsorbates. In constant current mode, a feedback mechanism is used to keep the tunneling current between tip and sample constant and the tip height is detected while scanning, see figure 3.1b. Therefore, a sufficiently fast feedback mechanism eliminates the risk of collision into the surface or adsorbates. The drawback of the constant current mode is a slower scan speed, which is required to ensure a sufficiently fast reaction of the feedback.

### 3.2.2 Tunneling model of Tersoff and Hamann

Shortly after the invention of the STM by Binnig and Rohrer in 1982 [51] Tersoff and Hamann developed a theoretical model to describe the tunneling current between tip and sample in 1983 [62, 63] by adopting the Bardeen tunneling model for solids [64]. Within the limits of small voltages and low temperatures, they derived the well known exponential dependence of the tunneling current on the tip-sample distance for a s-wave like tip. This exponential distance dependence constitutes one of the key factors for the STM capability to resolve atomic resolution with an atomically sharp tip.

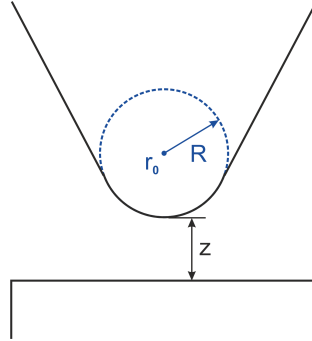


Figure 3.2: Schematic of the Tersoff and Hamann STM tunneling junction (adopted from [62]). The tip apex is assumed to have a spherical geometry with radius  $R$  and center  $\vec{r}_0$  and the surface is assumed as planar with a minimum distance  $z$  between tip and sample.

The Tersoff and Hamann tunneling model assumes a spherical tip and a planar surface, as shown in figure 3.2. Hence, the tunneling current  $I$  can be given in Bardeen's formalism [64] in first order by [62]

$$I = \frac{2\pi e}{\hbar} \sum_{\mu\nu} f(E_\mu)[1 - f(E_\nu + eV)] |M_{\mu\nu}|^2 \delta(E_\mu - E_\nu) \quad (3.1)$$

with  $f(E)$  the Fermi function,  $V$  the applied bias voltage between tip and sample,  $M_{\mu\nu}$  the tunneling matrix element between the states of the tip  $\psi_\mu$  and the states

of the surface  $\psi_\nu$ , and  $E_\mu$  ( $E_\nu$ ) the energy of  $\psi_\mu$  ( $\psi_\nu$ ) in absence of tunneling. In the limit of low temperatures (room temperature or below) and small voltages (around  $10\text{ meV}$ ), the tunneling current can be expressed as [62]

$$I = \frac{2\pi}{\hbar} e^2 V \sum_{\mu\nu} |M_{\mu\nu}|^2 \delta(E_\nu - E_F) \delta(E_\mu - E_F). \quad (3.2)$$

The tunneling matrix element  $M_{\mu\nu}$  can be given according to Bardeen [64] as [62]

$$M_{\mu\nu} = -\frac{\hbar^2}{2m} \int d\vec{S} \cdot (\psi_\mu^* \nabla \psi_\nu - \psi_\nu \nabla \psi_\mu^*) \quad (3.3)$$

with  $\vec{S}$  a surface lying anywhere in the vacuum barrier between the tip and the surface and  $(\psi_\mu^* \nabla \psi_\nu - \psi_\nu \nabla \psi_\mu^*)$  the current operator. To calculate the tunneling matrix element, Tersoff and Hamann assume an asymptotically spherical tip wave function (s-wave tip), which leads to [62, 63]

$$M_{\mu\nu} = \frac{\hbar^2}{2m} 4\pi k^{-1} \Omega_t^{-\frac{1}{2}} k R e^{kR} \psi_\nu(\vec{r}_0) \quad (3.4)$$

with  $k = \hbar^{-1}(2m\Phi)^{1/2}$  the the inverse decay length for the wave functions in vacuum,  $\Phi$  the work function of the tip and sample (which are assumed to be equal),  $\Omega_t$  the probe volume,  $R$  the radius of curvature of the tip, and  $\vec{r}_0$  the position of the center of curvature of the spherical tip, as shown in figure 3.2. This leads to a tunneling current of [62]

$$I = 32 \frac{\pi^3}{\hbar} e^2 V \Phi^2 \rho_t(E_F) R^2 \frac{e^{2kR}}{k^4} \sum_\nu |\Psi_\nu(\vec{r}_0)|^2 \delta(E_\nu - E) \quad (3.5)$$

with  $\rho_t$  the density of states per unit volume of the tip. Since  $|\Psi_\nu(\vec{r}_0)|^2 \propto e^{-2k(R+z)}$  [62], the exponential distance dependence of the tunneling current follows

$$I \propto e^{-2kz}. \quad (3.6)$$

Defining the local density of states (LDOS) of the sample  $\rho(\vec{r}_0; E)$  as

$$\rho(\vec{r}_0; E) \equiv \sum_\nu |\Psi_\nu(\vec{r}_0)|^2 \delta(E_\nu - E) \quad (3.7)$$

the tunneling current can be summarized as proportional to the LDOS of the sample

$$I \propto V \rho_t \rho(\vec{r}_0; E). \quad (3.8)$$

It should be noted that the tunneling current also depends on the density of states of the tip  $\rho_t$  which is assumed to be constant. But the experimental assurance of a constant tip and the estimation of the tip properties constitutes one of the key challenges in STM measurements.

### 3.2.3 Scanning Tunneling Spectroscopy (STS)

Electronic spectroscopy of the surface can be measured locally by the so-called scanning tunneling spectroscopy (STS). Hereby the LDOS of the surface is investigated in dependence of the applied bias voltage. The limit of small bias voltage in the order of around  $10\text{ mV}$  leading to equation 3.8 is not appropriate in STS. Therefore, Selloni and coworkers [65] followed the basic assumptions of the Tersoff and Hamann model and suggested an expression for the tunneling current which is more general in dependence of the applied voltage. In the limit of a s-wave tip and zero temperatures, they expressed the tunneling current  $I$  as an integral over the applied bias voltage between tip and sample [65]

$$I(V) \propto \int_{E_F}^{E_F+eV} \rho(\vec{r}_0, E - E_F) \rho_t(E) T(V, z, E) dE \quad (3.9)$$

with  $E_F$  the Fermi energy,  $eV$  the energy corresponding to the applied bias voltage  $V$  between the tip and the sample,  $\rho(\vec{r}_0, E - E_F)$  the LDOS of the sample at the tip position  $\vec{r}_0$ ,  $\rho_t(E)$  the DOS of the tip and  $T(V, z, E)$  the transmission function for the tunneling through the vacuum barrier ( $T(V, z, E) = |M_{\mu\nu}|^2$ ).

The tunneling through a vacuum barrier between tip and sample at an applied bias voltage is sketched in figure 3.3. At negative bias voltage  $-eV_s$ , as shown in figure 3.3a, the Fermi level of the sample is shifted with respect to the Fermi level of the tip and electrons tunnel from the occupied electronic states of the sample to the tip, indicated by arrows. At a positive applied sample bias voltage  $+eV_s$ , the electrons tunnel from the tip into the unoccupied sample states, as shown in figure 3.3b. The transmission function of the tunneling electrons is energy dependent and can be assumed to increase exponentially [52] as indicated by the length of the arrows. The tunneling current is the sum of all tunneling electrons in the energy window between the Fermi levels of the tip and sample.

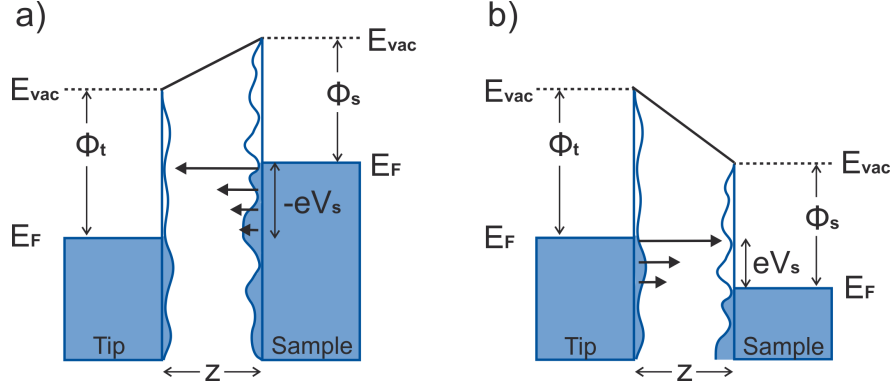


Figure 3.3: Scanning tunneling spectroscopy (STS). Schematic sketch of the tunneling barrier junction between tip and sample separated by a vacuum barrier of thickness  $z$ . a) At negative sample bias voltage  $-V_s$ , the Fermi level  $E_F$  of the sample is shifted by  $-eV_s$  with respect to the Fermi level of the tip and tunneling electrons flow from the occupied sample states to the unoccupied tip states as depicted by arrows. b) At positive sample bias voltage  $+V_s$ , tunneling electrons flow from the occupied tip states to the unoccupied sample states. The length of the arrows indicate the exponential energy dependence of the transmission function. The work function of the sample  $\Phi_s$  (tip  $\Phi_t$ ) is given by the energy difference between the Fermi level and the vacuum level  $E_{vac}$ .

To quantify the LDOS at a specific energy, the  $dI/dV$  signal can be measured. Assuming the tip DOS  $\rho_t$  and the transmission function  $T(V, z)$  as constant in energy, the LDOS can be expressed as directly proportional to the  $dI/dV$  signal [65]

$$\frac{dI}{dV} \propto \rho(\vec{r}_0, E_F + eV) \rho_t T(V, z). \quad (3.10)$$

But in experiment the consequences of these approximations should be taken into consideration. In STS measurements, the tip density of states depends strongly on the properties of the tip and has to be assessed. To quantify the tip properties, a reference  $dI/dV$  spectrum can be measured for example over the bare metal substrate and a comparison to literature can determine the nature of the tip as metallic or identify whether the LDOS indicate the adsorption of nonmetallic components as a picked up molecule on the tip. In the latter case, a convolution of the LDOS of the tip with the LDOS of the sample has to be taken into account. To avoid this, the tip is usually treated by small intentional dipping into the metal surface and voltage pulses until the tip has a metallic nature. The assumption of the transmission function as energy independent can for example be seen as an approximation to its upper limit at an energy corresponding to the applied bias

voltage  $E \leq eV$ . This results in a monotonous underestimation of the  $dI/dV$  signal at lower energies but will not result in a convolution of the  $dI/dV$  signal with additional features. In case of relevance, the underestimation of the low bias voltage  $dI/dV$  signal should be taken into consideration in a normalization of the  $dI/dV$  spectrum [52].

In principle a differential conductance  $dI/dV$  spectrum can be measured by detection of the current signal during a bias voltage ramp and calculation of the current signal derivative. However, in order to enhance the signal to noise ratio, the  $dI/dV$  signal is commonly directly detected by using a lock-in-amplifier. In a lock-in detection technique, a part of the incoming signal is modulated with a specific frequency in such a way that the measurement observable gets modulated with this frequency. This allows to extract only the modulated measurement observable out of the measured signal and improves the signal to noise ratio. Thereby, the detection of small signals within a large background is enabled. In STS measurements a lock-in-amplifier modulates the bias voltage with a oscillation signal  $V_{mod}\sin(\omega t)$ . The resulting modulated tunneling current signal can be approximated by a Taylor expansion

$$I(V_{bias} + V_{mod}\sin(\omega t)) \approx I(V_{bias}) + \frac{dI(V_{bias})}{dV} V_{mod}\sin(\omega t) + \dots \quad (3.11)$$

giving the  $dI/dV$  signal as directly proportional to the amplitude of the modulated signal which can be extracted. Next to the increased signal to noise ratio, the direct detection of the  $dI/dV$  signal exhibits the advantage that the bias voltage does not need to be ramped to measure the  $dI/dV$  signal. This is used for example in so-called  $dI/dV$  mapping where the surface  $dI/dV$  signal is imaged at a specific energy.

### 3.2.4 Inelastic Electron Tunneling Spectroscopy (IETS)

In STS the tunneling electrons preserve their energy and tunnel elastically from the tip through the vacuum barrier into the surface or vice versa. If the electrons excite during the tunneling a (molecular) vibration and lose energy, the electrons tunnel inelastically which can be quantified in so-called Inelastic Electron Tunneling Spectroscopy (IETS). To excite a molecular vibration, the tunneling electrons need at least the energy corresponding to the molecular vibration  $eV \leq \hbar\omega$ . Below the vibrational energy  $\hbar\omega$  only elastic tunneling occurs but a part of the tunneling electrons tunnel inelastically above the vibrational energy, leading to an additional tunneling channel. If the change in the elastic and inelastic tun-

neling probability is not equal, it can be observed in the IETS. Commonly, the opening of the inelastic tunneling channel results in an increase of the tunneling probability and can be observed as a kink in the current signal (see figure 3.4b), a step in the  $dI/dV$  signal (see figure 3.4c), and a dip and peak in the  $dI^2/dV^2$  signal at an energy of  $\pm\hbar\omega$  (see figure 3.4d). In an experiment the latter two are detected by a lock-in amplifier which results in a higher detection sensitivity due to the increased signal to noise ratio. With the detection of molecular vibrations with IETS [66–68], the STM also has a chemical sensitive tool next to its atomic resolution imaging possibilities.

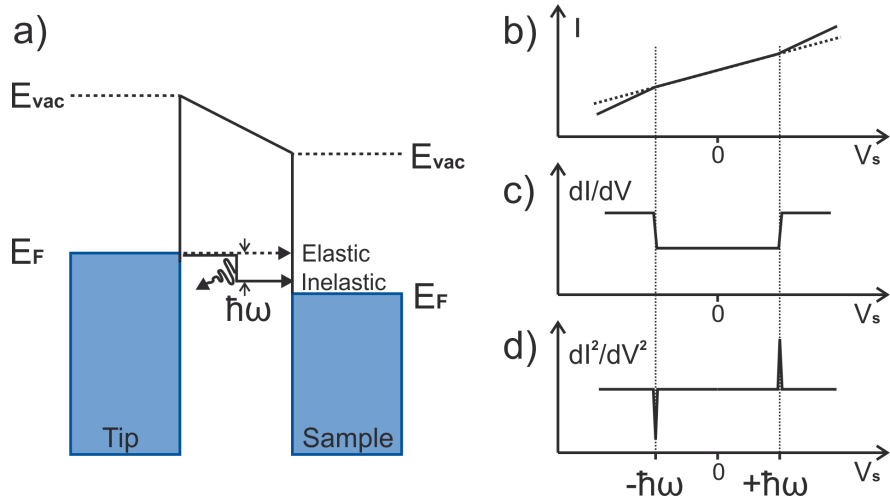


Figure 3.4: Inelastic electron tunneling spectroscopy (IETS). a) Schematic sketch of the tunneling barrier configuration. If the applied bias voltage provides sufficient energy to excite a (molecular) vibration with  $\hbar\omega$ , the electrons can tunnel inelastically through this additional channel (next to the elastic channel symbolized by the dotted arrow). b) The molecular vibration can be observed as a kink in the current channel, c) a step in the  $dI/dV$  signal, and d) a dip and peak in the  $dI^2/dV^2$  signal at an energy of  $\pm\hbar\omega$ .

## 3.3 Atomic Force Microscopy (AFM)

### 3.3.1 Working principle of an AFM

In 1986 Binnig, Quate, and Gerber realized the first setup of an AFM, opening the possibility to measure forces on the atomic level and to achieve spatial atomic resolution imaging on non conductive samples [69]. Similar to the STM, the AFM scans and images the surface but in contrast to the tunneling current detecting STM setup, the AFM detects the interaction forces between the tip and sample. Therefore, also the investigation of non conductive samples and tip materials is possible, as this detection principle requires no current flow between tip and sample. This is a huge advantage and led to an even broader application field of the AFM. But also in combination with STM, the AFM opens the possibility to additionally investigate the tip-sample forces, which results in a deeper understanding of surfaces at the atomic level.

AFMs can be operated in contact, non-contact, static, and dynamic mode. Depending on the operation mode, they directly quantify the interaction forces between tip and sample or a related parameter as the force gradient. For the detection an STM setup or a cantilever with a laser detection system can be used. In this thesis a combined STM/AFM system is used and an introduction to measured forces, the operation modes and the force detection with NC-AFM will be given in the following. As the AFM operation and set up are very diverse, the introduction focuses on the motivation and description of the used NC-AFM. In addition, comprehensive explanations of the different detection modes, AFM sensors and setups can be found in literature [52, 70–73].

### 3.3.2 Forces in AFM

In AFM different forces contribute to the interaction between tip and sample. In UHV experiments short range chemical forces, van der Waals forces, electrostatic forces, and magnetic forces contribute to the total interaction force. As the latter requires magnetic tips and samples, it is not a force which will be discussed in this thesis. The following sections will focus on the short range chemical forces and the long-range van der Waals forces. At this point only the long-range nature of the electrostatic forces should be mentioned and their relevance for AFM measurements will be discussed later in a separate section.

### 3.3.3 Chemical forces - Morse potential model

The short range chemical forces are of attractive and repulsive nature. They are present in the AFM measurement if the distance between the tip and sample is in the order of Ångströms so that the wave functions overlap. For simultaneous STM and AFM measurements, the chemical forces have comparable range to the tunneling current. In an idealized case these short range forces can be modeled by the interaction potential between two single atoms. In 1929 Philip M. Morse proposed a model potential for the interaction in a diatomic molecule [74]

$$U_{Morse}(z) = -E_d[e^{-2\kappa(z-z_e)} - 2e^{-\kappa(z-z_e)}] \quad (3.12)$$

$$F_{Morse}(z) = -E_d 2\kappa [e^{-\kappa(z-z_e)} - e^{-2\kappa(z-z_e)}] \quad (3.13)$$

with  $z$  the distance between the two nuclei, respectively the tip-sample distance in AFM,  $E_d$  the bond energy at the minimum potential  $z = z_e$ , the so-called the equilibrium distance  $z_e$ , and  $\kappa$  the decay length. The Lennard-Jones potential [75] is an alternative model with very similar properties [76].

### 3.3.4 Van der Waals forces - London dispersion force

Van der Waals forces describe the dipole interactions between atoms and molecules. The exceptional nature of van der Waals forces is their interaction in long range between all kind of atoms and molecules. Explicitly, also totally neutral atoms and molecules contribute to the van der Waals forces due to induced dipole interactions, the so-called London dispersion forces. In case of presence, the interaction forces between two permanent dipoles, as well as the interaction forces between a permanent and an induced dipole can add to the London dispersion forces.

The origin of the London dispersion force is of quantum mechanical nature. Considering a neutral atom, an instantaneous dipole moment can be present due to the instantaneous position of the electrons around the nuclei. The electric field of this instantaneous dipole moment polarize another atom close by and induce a dipole moment in it [77]. In the simplified case one can assume the dispersion forces as rigid, cohesion forces which are additive [78]. The dispersion energy between two identical neutral atoms or molecules can be expressed according to London by [78] [77]

$$U_{vdW}(z) = -\frac{C_{disp}}{z^6} \quad (3.14)$$



with  $C_{disp}$  a coefficient describing the interaction strength and  $z$  the distance between the atoms or molecules. The total present dispersion forces can then be expressed as a sum over all participating particles. For the case of a spherical tip over an infinite plate, the dispersion energy is given according to Hamaker by [79] [77]

$$U_{vdW}(z) = \frac{HR}{6z} \quad (3.15)$$

$$F_{vdW}(z) = -\frac{HR}{6z^2} \quad (3.16)$$

with  $H = \pi^2 C_{disp} \rho_t \rho_s$  the Hamaker constant,  $R$  the tip radius,  $z$  the tip-surface distance,  $\rho_t$  the density of states of the tip and  $\rho_s$  the sample. In principle van der Waals forces are present from short to long-range distances but their additive nature results in a particular importance for the long-range interaction regime. For tip-sample distances larger than around  $1\text{ nm}$  [52], the van der Waals forces are the largest forces which are detected in an AFM.

### 3.3.5 Operation modes - static and dynamic AFM

The force detection with an AFM can be realized with different operation modes which have advantages and disadvantages especially with respect to the construction of the experimental setup, a direct or indirect quantification of the measured interaction forces, and the spatial detection limit of the investigated surface systems. In the straight forward approach, a cantilever can be used to measure the deflection due to the interaction forces. In this case, the AFM operates in a static AFM mode and the interaction force can be extracted directly out of the deflection signal. But in order to observe a high resolution AFM signal, the tip-sample distance must be small to sense the short range chemical forces, as the long-range van der Waals forces dominate the signal at larger tip-sample distances. In static AFM mode the large attractive forces at very close tip-sample distances can result in the problematic situation that a insufficiently stiff cantilever gets pulled into the surface, a so-called jump to contact. Such a jump to contact can cause damage on the surface and the tip. Here, literature shows that atomic periodicity can be imaged [80–82]. However, the detection of so-called true atomic resolution with local atomistic effects (e.g. defects) is hardly possible [70, 83]. For stable measurements the stiffness of the cantilever  $k$  must always exceed the maximal measured tip-sample force gradient  $k_{ts}^{max}$  [70]

$$k > k_{ts}^{max}. \quad (3.17)$$

Dynamic operation of the AFM opens the possibility to prevent a jump to contact by oscillating the tip and enables to image true atomic resolution [54,84]. With the choice of a sufficient oscillation amplitude  $a$ , it can be ensured that the tip has enough energy to retract again at its smallest tip-sample distance without being pulled into the surface. For a stable dynamic AFM operation, the force  $ka$  of the with amplitude  $a$  oscillating cantilever needs to exceed the maximal measured tip-sample force  $F_{ts}^{max}$  [70]

$$ka > F_{ts}^{max}. \quad (3.18)$$

Therefore, next to the oscillation amplitude, the cantilever stiffness provides an additional parameter to prevent a jump to contact in dynamic AFM. A detailed description of further advantages of dynamic AFM, like the reduction of low-frequency noise, can be found in literature [70].

Dynamic AFM can be operated in amplitude modulation and in frequency modulation. Both detection modes have their technical advantages and limitations and probe different force related properties of the sample. Thus, their use is determined by the sample under investigation and the applied system. Amplitude modulated operation as the intermittent contact mode (tapping mode) are commonly used under ambient conditions. For UHV experiments the frequency modulation has become the standard operation mode due to its faster scan time. Frequency modulated dynamic AFM, the so-called NC-AFM, is used for the research in this thesis and its methodology will be introduced in the following sections.

### 3.3.6 Non-contact AFM (NC-AFM)

In NC-AFM (frequency modulated dynamic AFM) the tuning fork is oscillated with an oscillation amplitude  $a$  at its resonance frequency  $f_0$ . The oscillation amplitude is kept constant while the resonance frequency is shifted when forces act on the tip due to interactions with a probe. This frequency shift  $\Delta f$  is the measurement observable and gives a drawback on the acting forces. Generally, it is not trivial to derive the tip height dependent forces acting on the tip from the measured frequency shift, as the tip is oscillating. However, the dependence can be deduced analytically in the so-called small amplitude limit, which is valid for small oscillation amplitudes compared to the length scales of the tip-sample interaction forces and assumes a constant force gradient over an oscillation cycle of the tuning fork [70].

The oscillating tuning fork can be modeled by a damped harmonic oscillator

$$f_0 = \frac{1}{2\pi} \sqrt{\frac{k}{m}} \quad (3.19)$$

with  $k$  the spring constant and  $m$  the mass of the tuning fork. The tip-sample forces  $F$  are changing the resonance frequency of the oscillator to a new frequency  $f = f_0 + \Delta f$  and in the limit of a constant force gradient  $k_{ts} = \frac{dF}{dz}$  over one oscillation cycle, this can be expressed by

$$f = f_0 + \Delta f = \frac{1}{2\pi} \sqrt{\frac{k + k_{ts}}{m}}. \quad (3.20)$$

This leads to an observed frequency shift of

$$\Delta f = f - f_0 = \frac{1}{2\pi} \sqrt{\frac{k}{m}} \left( \sqrt{1 + \frac{k_{ts}}{k}} - 1 \right). \quad (3.21)$$

For  $k_{ts} \ll k$  the square root can be simplified with  $x = \frac{k_{ts}}{k}$  by the approximation of  $\sqrt{1+x} \approx 1 + \frac{1}{2}x$  which is valid for small  $x$  [52]

$$\Delta f = \frac{1}{2\pi} \sqrt{\frac{k}{m}} \cdot \frac{1}{2} \frac{k_{ts}}{k} = \frac{f_0}{2k} \frac{dF}{dz}. \quad (3.22)$$

The frequency shift  $\Delta f$  is therefore proportional to the force gradient  $\frac{dF}{dz}$  of the tip in the limit of a constant force gradient over an oscillation amplitude cycle and  $k_{ts}(z) \ll k$ .

### 3.3.7 Sader Jarvis Method

In general the force gradient can not be considered as constant especially for large oscillation amplitudes or very close tip-sample distances where the forces depend very strongly on the distance to the surface. For an arbitrary force  $F$  one can derive a general expression for the frequency shift  $\Delta f$  by the Hamilton-Jacobi formalism in first order approximation for  $\Delta f \ll f_0$  as reported by Giessibl [85,86]

$$\Delta f = -\frac{f_0}{\pi a k} \int_{-1}^1 F(z + a(1+u)) \frac{u}{\sqrt{1-u^2}} du \quad (3.23)$$

with  $f_0$  the resonance frequency,  $a$  the oscillation amplitude, and  $k$  the spring constant of the cantilever, and  $z$  the distance of closest approach between tip and sample. This general form of the frequency shift must be inverted in order to

reveal the measured forces in dynamic force spectroscopy. In the limits of small or big oscillation amplitudes in comparison to the length scale of the interaction forces, this can be solved analytically [85]. Nevertheless, a general expression for arbitrary oscillation amplitudes and forces is not known. Sader and Jarvis [86] proposed a force deconvolution method using a Laplace transformation and an appropriate Bessel function which can be applied for arbitrary forces and oscillation amplitudes.

It gives for the interaction force  $F(z)$

$$F(z) = 2k \int_z^\infty \left(1 + \frac{a^{1/2}}{8\sqrt{\pi(t-z)}}\right) \frac{\Delta f(z)}{f_0} - \frac{a^{3/2}}{\sqrt{2(t-z)}} \frac{d(\frac{\Delta f(z)}{f_0})}{dt} dt. \quad (3.24)$$

For the interaction energy  $U(z)$  the Sader Jarvis method gives

$$U(z) = 2k \int_z^\infty \frac{\Delta f(z)}{f_0} \left( (t-z) + \frac{a^{1/2}}{4} \sqrt{\frac{t-z}{\pi}} + \frac{a^{3/2}}{\sqrt{2(t-z)}} \right) dt. \quad (3.25)$$

For small and large oscillation amplitudes the Sader Jarvis formulas converge to the analytically determinable exact solutions and gives an error of less than 5% in all other cases. But it should be noted again that the formulas are only valid for a constant oscillation amplitude which is independent of the tip-sample distance, whereby its realization with appropriate feedback parameters can be an experimental challenge.

### 3.3.8 Electrostatic forces and Contact Potential Difference (CPD)

Electrostatic forces arise due to different work functions between the metallic tip and sample. If two metals with different work functions  $\Phi$  are not in contact to each other, the work functions align to the vacuum level  $E_{vac}$  and their Fermi energies  $E_F$  are not aligned, this situation is sketched in figure 3.5a. If the two metals are in electrical contact to each other, electrons flow from the metal with the lower work function to the metal with the higher work function until surface charges compensate the work function difference and the Fermi levels are aligned, see figure 3.5b. The vacuum levels of an electrically connected tip and sample are not aligned and separated by the work functions difference  $\Delta\Phi = \Phi_t - \Phi_s = eV_{CPD}$  which is commonly referred to as contact potential difference (CPD)  $V_{CPD}$  in the

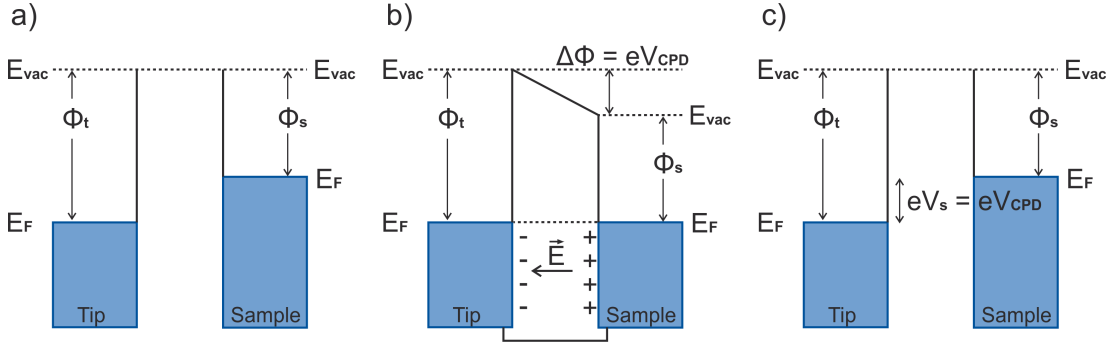


Figure 3.5: Electrostatic forces and contact potential difference (CPD) in AFM. a) Two metals with different work functions,  $\Phi_t$  for the tip and  $\Phi_s$  for the sample, align their vacuum levels  $E_{vac}$  when they are not in contact to each other. b) If they are in contact, electrons flow from the metal with lower work function to the other and build up surface charges until the electric field of the surface charges aligned the Fermi levels  $E_F$  of the tip and sample. The electrostatic field between the tip and sample leads to the electrostatic forces. The vacuum levels differ by the work function difference  $\Delta\Phi$ , the corresponding voltage  $V_{CPD}$  is defined as CPD. c) The electrostatic field and forces vanish if an applied bias voltage  $V_s$  is equal to the CPD  $V_s = V_{CPD}$ .

field of AFM. The electrostatic force results from these surface charges which compensate for the work function difference of the electrical connected tip and sample of an AFM. In a simple model the surface charges of tip and sample can be seen as a capacitor. For a spherical tip over an infinite plate sample, the electrostatic forces can be expressed by [87]

$$F_{el}(z) = \pi\epsilon_0 \left[ \frac{R^2}{z(z+R)} \right] V_{cap}^2 \quad (3.26)$$

with  $z$  the tip-sample distance,  $\epsilon_0$  the permittivity of free space,  $R$  the tip radius, and  $V_{cap}$  the voltage of the capacitor. The voltage of the capacitor is determined by the CPD  $V_{CPD}$  between tip and sample and the applied bias voltage  $V_s$

$$V_{cap} = V_s - V_{CPD}. \quad (3.27)$$

If a bias voltage equal to the CPD of the tip-sample junction is applied  $V_s = V_{CPD}$ , the work function difference can be compensated without surface charges and the electrostatic force component vanishes, as sketched in figure 3.5c.

The electrostatic force follows, according to equation 3.26, a parabolic voltage dependence with a minimum at the CPD for  $V_s = V_{CPD}$ . Here a bias voltage sweep can be used to measure the CPD between tip and sample. This capacitive

detection method was proposed by Kelvin as early as 1898 [88] and has become common to detect the CPD in AFM measurements.

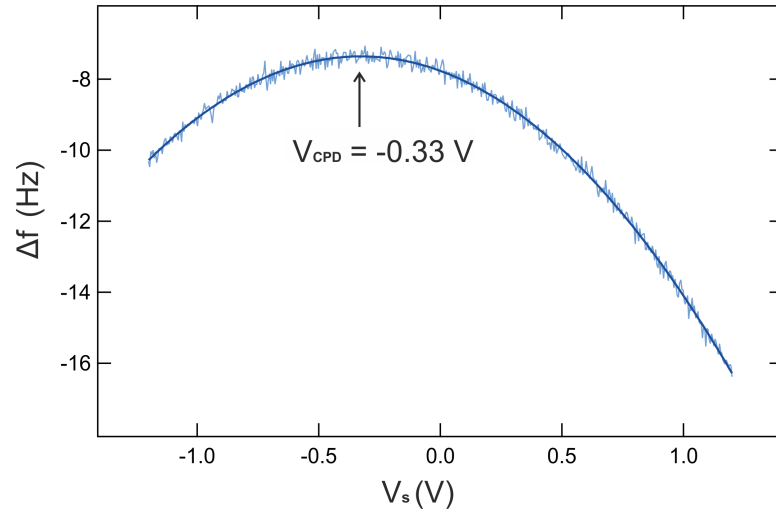


Figure 3.6: CPD measurement.

## 3.4 Experimental setup

The measurements shown in this thesis were performed in a customer modified commercially available low-temperature Omicron SPM system [89] equipped with Nanonis electronics from Specs GmbH [90] and operating at low temperatures of 5 K unless stated otherwise. All measurements and sample preparations were performed under UHV conditions with a base pressure of around  $10^{-10} - 10^{-11}$  mbar to avoid surface contaminations. The theoretical principles and technical details of vacuum technology are described in detail in various books [91–95]. Therefore, the following will focus on a brief description of the used setup and the sample preparation.

### 3.4.1 Setup of the UHV chambers

The SPM used in this thesis is situated in a UHV setup. Single crystalline metal surfaces are in general very reactive and easily contaminated by e.g.  $\text{H}_2\text{O}$ ,  $\text{O}_2$ , etc. in air. Therefore all the measurements and sample preparations in this thesis are performed under UHV conditions with a base pressure of around  $10^{-10}$  mbar to ensure an atomically clean and stable surface structure without the influence of contaminations. The UHV conditions in the setup are realized by a turbo-molecular pump, two ion-pumps, two titan-sublimation-pumps and the cryostat functioning as cooling pump. In figure 3.7 a photo of the UHV system is shown consisting of the SPM chamber equipped with the cryostat and the preparation chamber. Both chambers are separated by a gate valve to allow sample preparation without disturbing the base pressure in the STM chamber. The system is situated on air legs to separate it from vibrations transferred via the laboratory floor. The system is constructed to allow the sample cleaning and preparation with molecules in the separated preparation chamber and transfer the fresh prepared sample within UHV conditions to the SPM chamber for the measurements. For sample preparations at low temperatures on the surface within the SPM, molecules or gas atoms can also be deposited in the SPM chamber. The UHV setup is equipped with a load lock to provide an easy transfer channel for new samples, STM tips or  $\text{q}^+$ -sensors into the system without breaking the UHV conditions. Thereby, STM tips and  $\text{q}^+$ -sensors can be handled within the system and exchanged in the SPM head via the same mechanism as the samples.

For the sample cleaning, preparation and handling, the preparation chamber is equipped with the following tools:

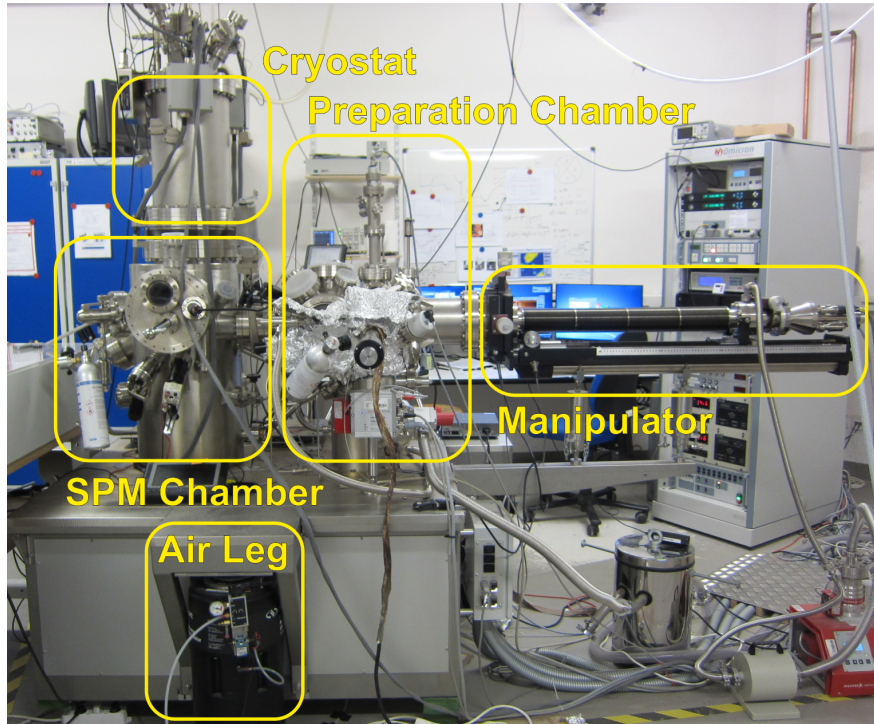


Figure 3.7: SPM setup. Photo of the SPM setup which consists of the SPM chamber and a gate valve separated preparation chamber. The SPM head in the SPM chamber is cooled by liquid nitrogen and helium in the cryostat. The manipulator is used to transfer samples and tips within and between the chambers. The whole setup is situated on air legs to damp mechanical vibrations from the laboratory floor.

- Load lock: a gate valve separated, very small chamber which can be pumped within a few hours to allow transferring of samples and tips without breaking the UHV of the preparation chamber.
- Manipulator: to handle the samples and tips in the preparation chamber. The manipulator can be moved along all three axes and can be rotated by 360°.
- Heating stage (on the manipulator): for annealing the sample for example after the sputtering.
- Screwdriver: to fix the sample on the manipulator stage to allow the use of all manipulator angles without risk of dropping the sample.
- Argon gas valve: to provide Argon gas for the sample cleaning.



- Sputter gun: to accelerate Ar-ions on the surface to remove contaminations from the surface.
- Molecule evaporator: for the deposition of molecules on the surface.
- Quartz balance: to quantify the evaporation rate from the molecule evaporator.
- Quadrupole mass spectrometer: to detect the composition and evolution of the present particles in the UHV system for example during a leak check.

For the sample transfer, storage and the low-temperature sample preparations within the SPM, the SPM chamber is equipped with the following tools:

- Wobble stick: for the tip and sample transfer into the SPM head and opening and closing of the cooling shields.
- Gas valve: for deposition of e.g. Xe atoms on the cold sample located in the SPM head.
- Sample garage: for the storage of samples, STM tips, and AFM sensors under UHV conditions and the possibility to exchange them fast.

### 3.4.2 SPM head

The SPM head is located in the SPM chamber below the cryostat. It is cooled by the liquid helium and nitrogen in the cryostat and surrounded by two cooling shields for the realization of a temperature of  $5\text{ K}$ . Figure 3.8 shows a photo of the SPM head with dismantled cooling shields. The SPM tip is placed on piezo crystal which allows the atomically precise scanning of the tip. The sample can be slid into the sample holder which is equipped with a heating stage and a temperature controller. With the temperature controlled heating, the sample can be measured at constant intermediated temperatures in the range between  $5\text{ K}$  and room temperature. The SPM head is mounted on three springs to the SPM chamber system. Together with an eddy current brake, the springs provide a good vibrational isolation to the rest of the system to prevent disturbances during the measurement. Additionally, the system is equipped with a clamping mechanism to allow efficient cooling, for example after a sample transfer. In clamped position, the SPM head is thermally coupled to the cryostat via a Cu block. During the measurements, the SPM head is released in order to ensure the vibrational damping by the springs.

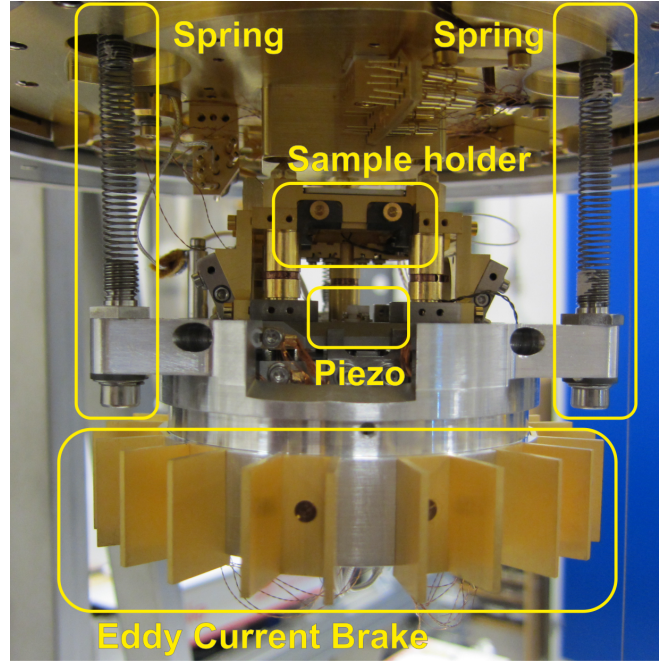


Figure 3.8: SPM head. Photo of the SPM head with dismantled liquid nitrogen and helium cooling shield. An SPM tip is placed on the piezo crystal and the sample is slid into the sample holder (photo without tip and sample). The SPM head is mounted on three springs to the SPM chamber and equipped with an eddy current brake to achieve a good vibrational isolation from the rest of the SPM setup.

### 3.4.3 SPM tips

For the SPM measurements, STM tips or AFM tuning forks in design of the  $q^+$ -sensor [84] can be used. SPM tips are commonly fabricated by electrochemical etching of tungsten wires but atomic resolution STM measurements can already be obtained by a mechanical cut tungsten wire. The shape of an AFM tip apex is more critical due to the presence of the long range forces. For the STM research in this thesis commercially available electrochemical etched tungsten STM tips from Omicron were used. Additionally, mechanical cut platinumiridium wire and commercially available mechanically polished, and electrochemically etched platinumiridium tips from Unisoku were mounted to Omicron STM tip holders and used for STM experiments in dependence of the tip shape. For the AFM measurements in this thesis, the commercially available  $q^+$ -sensor with electrochemical etched tungsten tips from Omicron were used. A photo of the  $q^+$ -sensor on an Omicron SPM sample holder is shown in figure 3.9a. The bias voltage was applied to the sample for the AFM measurements. For the STM measurements the bias voltage

was applied either to the tip or the sample but all bias voltages are given with respect to the sample  $V_s$  in this thesis.

Before an air exposed SPM tip was used for the measurements, the tip apex was cleaned by voltage pulses up to  $\pm 10\text{ V}$  and intentional dipping into the clean metal surface by several  $\text{nm}$ . During and after this procedure the surface area was changed to ensure a clean surface without contaminations coming from the tip. Therefore, it can be expected that the tip apex is covered by atoms of the used metal surface. Voltage pulses of up to around  $\pm 4\text{ V}$  and dipping into the surface by a few  $100\text{ pm}$ , so-called tip-forming, was used during the measurements to intentionally change and clean the tip apex.

### 3.4.4 AFM setup with the $q^+$ -sensor

For the AFM measurements in this thesis, a  $q^+$ -sensor setup of the so-called second generation was used [96]. In the first generation of the  $q^+$ -sensor setup, an influence of the current to the frequency shift signal, the so-called cross-talk, was observed [97, 98]. The second generation setup of the  $q^+$ -sensor is shown in figure 3.9b. To reduce the cross-talk between the frequency shift and the current channel the used second generation setup collects the tunneling current from the sample side and has an optimized internal wiring [97, 98]. But in contrast to the third generation of the  $q^+$ -sensor setup [96, 99], it does not have a separate tip wire. The AFM data in this thesis are measured at  $0\text{ V}$  bias voltage which exclude a cross-talk in principle due to the absence of a tunneling current. Additionally, a possible influence of a small tunneling current which could result from the finite resolution of the instrument which cannot provide a bias voltage of exactly  $0\text{ V}$  is investigated and discussed in section 5.2.2.

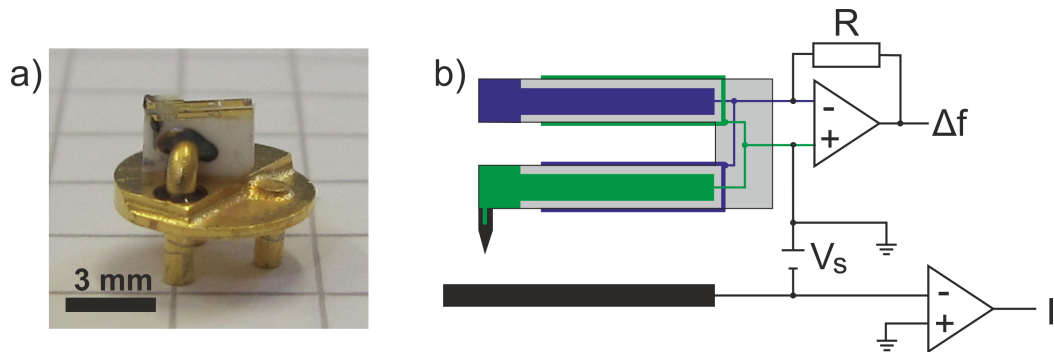


Figure 3.9: AFM set up with the  $q^+$ -sensor. a) Photo of the  $q^+$ -sensor on an Omicron SPM tip holder. b) Schematic of the  $q^+$ -sensor electrodes and amplifier.

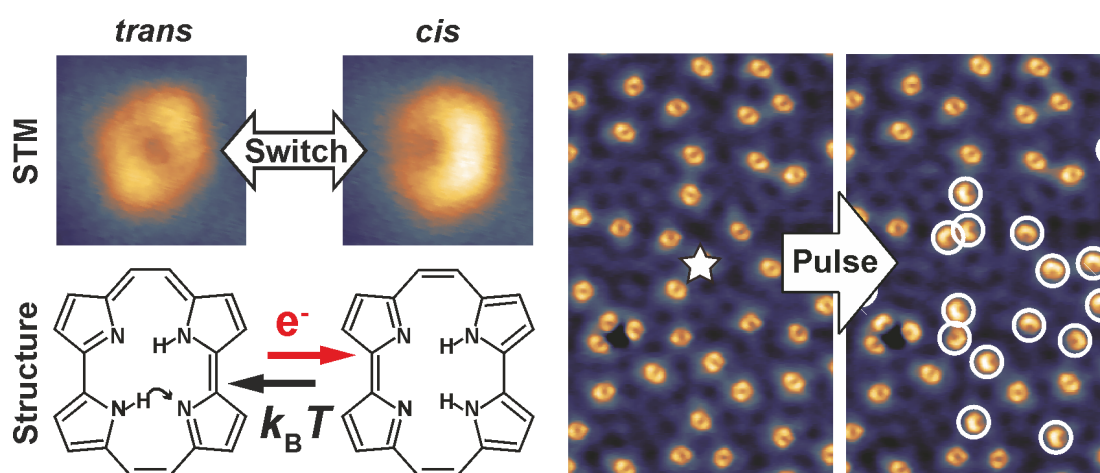
### 3.4.5 Sample preparation

For the research in this thesis, commercially available single crystalline Cu surfaces in (111) and (110) orientation with an accuracy of  $0.1^\circ$  and a surface roughness of  $0.01\ \mu\text{m}$  from MaTeck [100] were used as samples. Before the Cu surface was used for SPM measurements, it was cleaned in the preparation chamber. A pressure of around  $5 \times 10^{-6}\ \text{mbar}$  Argon gas was let into the preparation chamber. The Argon atoms are ionized by the sputter gun and accelerated onto the surface by application of a high voltage of  $1.5\ \text{kV}$  between the sputter gun and the sample. Here, a current of around  $6\ \mu\text{A}$  can be observed between the sputter gun and the sample. The accelerated Argon ions hit the surface of the sample and remove the first surface layers and contaminations. After the sputtering, the rough surface structure is healed out by annealing the surface to around  $400 - 500^\circ\text{C}$  for around  $10\ \text{min}$ . The sputtering and annealing cycle is repeated several times depending on the amount and nature of the contaminations, as remaining contaminations can diffuse from the surface into the first layers during the annealing. In the used setup, the clean nature of the surface was checked by STM imaging.

The molecules were evaporated onto the clean metal surface from a small heated glass crucible, a so-called Kundsén cell evaporator. Porphycene molecules start to evaporate at temperatures around  $180^\circ\text{C}$ . The deposition rate was estimated by a quartz micro-balance which consists of an at around  $6\ \text{MHz}$  oscillating quartz that shifts its resonance when mass is attached. By taking into consideration the quartz frequency shift and the sample evaporation time with respect to previous sample preparations the molecular coverage of the surface can be estimated. The porphycene molecules were evaporated at room temperature and directly transferred into the SPM head for measurements.

## Chapter 4

# Hot carrier-induced tautomerization



### Abstract

In this study we investigate the hot carrier-induced tautomerization of single porphycene molecules on a Cu(111) surface with low-temperature STM. On the Cu(111) terraces, the porphycene molecules adsorb in the *trans* tautomeric state and can be tautomerized to the metastable *cis* state by vibrational excitation via an inelastic electron tunneling process during a voltage pulse and thermally switched back to the *trans* state. The *cis* molecules could be excited thermally and vibrationally to a reversible *cis* to *cis* tautomerization. Furthermore, voltage pulse induced nonlocal tautomerization of porphycene molecules in distances of up to 100 nm was found and identified as hot carrier-induced by variation of the tip height and tunneling current in

a decoupled fashion by the use of step edges and clusters. The nonlocal tautomerization shows to be especially efficient for the excitation of hot electrons traveling via the surface state. Distinct interactions between the surface state and the adsorbed molecules lead to a molecular coverage dependence of the tautomerization efficiency with surface state mediated porphycene adsorption at low coverages and locally quenched surface state at high porphycene coverage.

## 4.1 Introduction

### 4.1.1 Nonlocal reactions induced by STM

In addition to the excitation of individual molecules, also nonlocal reactions can be induced by STM and were investigated on metal [30–33, 101, 102] and semiconductor [103, 104] surfaces. This nonlocal excitation could be of advantage in possible future applications in nanoscale science, as this method allows to address several molecules within a controllable area of up to  $100\text{ nm}$  [21, 30–33, 101–104] at the same time. The nonlocal reaction can be triggered either by the electric field [101, 105–108] or the propagation of hot carriers [30–33]. Hereby, the propagation of hot carriers is a particularly interesting nonlocal excitation mechanism as it can be associated with photo induced reactions on surfaces [29]. Hence, the detailed understanding of the mechanisms in hot carrier-induced processes and their coupling to the local environment will also provide a further understanding of photo induced chemistry on surfaces and key aspects, as the hot carrier traveling distance, efficient hot carrier transport states or the influence of adsorbed molecules, can be investigated by using the nonlocal excitation of molecules as monitor for the hot carrier transport across the surface.

### 4.1.2 Hot carrier-induced reactions on metal surfaces

Hot carrier-induced nonlocal reactions have for example been investigated by Maksymovych and co-workers who characterized the dissociation of adsorbed molecules on various metal surfaces [31]. They dissociated for instance  $\text{CH}_3\text{SSCH}_3$  on a Au(111) surface by an STM voltage pulse above  $1.4\text{ eV}$ . This relatively high excitation voltage suggests a reaction via an electronic rather than a vibrational excitation. The dissociation efficiency was found to depend on the pulse parameters with an increasing efficiency for higher pulse voltages, a linear dependence on the current, and an exponentially decaying efficiency as a function of radial

distance from the pulse. The presence of a hot carrier mechanism and absence of an electric field induced process was identified by the application of the excitation pulse above nanosize conductive clusters on the surface. Even though the tip is retracted above the cluster and thereby a smaller electric field acts on the molecules, the process showed the same efficiency as for a pulse directly above the surface. For future application in nanoelectronics or photo induced processes, a detailed knowledge about the electronic states that contribute to the hot carrier transport is of interest but these could not be rigorously assigned. In principle the hot carriers can travel through a surface state along the surface and excite a nonlocal reaction, but the molecular dissociation was also observed in absence of a surface state, e.g. it was observed on the  $(5\times 20)$  reconstructed Au(100) surface at a voltage of around 1.3 V significantly below the first surface state resonance at 4 V. Maksymovych and co-workers expected a contribution of pure bulk states to be unlikely as the hot carriers would leave the surface regime quickly and suggested a possible contribution from bulk states at the edge of the projection band gap, as these were found to show similar properties to surface state resonances [109]. This rises the question of the role of the surface state in efficient hot carrier transport.

### 4.1.3 Influence of the surface state on adsorbed molecules and vice versa

Another interesting contribution to the hot carrier traveling efficiency is the molecular coverage. A limiting influence on the hot carrier traveling efficiency was reported for the number of adsorbed oxygen molecules on a Ag(110) surface [33]. Especially in combination with the transport of the hot carriers through the surface state, the influence of the coverage gets important, as literature shows that the surface state influences the adsorption of molecules and vice versa [110, 111].

How the surface state influences the adsorption of atoms or molecules was shown by J. Repp and co-workers for the case of Cu adatoms on a Cu(111) surface [110]. A statistical analysis of the Cu adatom separation distances revealed that the single adatoms adsorb with a preferred separation on the Cu(111) surface. The separation distances of the atoms are of oscillatory nature and could be identified to origin from the interaction potential of the surface state scattering with a periodicity of half the Fermi wavelength of the surface state.

The influence of the adsorption of molecules on the surface state was reported by Lindgren and co-workers for the case of CO molecules on a Cu(111)

surface [111]. Their angle resolved photoelectron energy spectroscopy showed a clear energy shift and a reduced peak intensity of the Cu(111) surface state with increasing adsorption of CO molecules on the surface. They could rationalize the reduction of the surface state intensity by a local extinction of the unperturbed metal surface state in the surrounding of an adsorbed CO molecule. The observed surface state intensity suggested a wiping out of the surface state on the Cu atoms directly under and nearest neighboring to the CO molecule adsorbed on top position.

Therefore, the hot carrier transport through the surface state and the adsorption of molecules could be sensitively influenced by each other and may open the possibility to tune the hot carrier transport in dependence of the molecular coverage. Here, the capability of the STM to investigate the surface properties locally provides an ideal investigation tool.

#### 4.1.4 Motivation for Cu(111) as metal substrate

The previous study of porphycene showed that on Cu(110) exclusively the *cis* tautomeric state is present, as described in section 2.3, even though the *trans* state is energetically favorable in gas phase [47,48]. This demonstrates the importance of the surface in stabilizing the adsorption geometry and raises the questions of the importance of the surface crystallographic orientation and a possible stabilization of the *trans* state on another surface orientation like e.g. Cu(111). For the investigation of a nonlocal tautomerization, the presence of two nondegenerate tautomeric states as e.g. the *trans* and *cis* state would be ideal, as they could provide distinguishable initial and final states for observing the nonlocal tautomerization. The comparable energetics of the *trans* and *cis* state in gas phase and the presence of the slightly disfavorable gas phase state on the Cu(110) surface provide the possibility of stable *trans* and *cis* state existence on another surface orientation. In this study we choose Cu(111) as metal substrate which has a surface state at  $-0.4\text{ V}$  [34], and therefore provides ideal conditions to evaluate the role of the surface state for the hot carrier transport efficiency and a possible coupling to adsorbed molecules and vice versa.



## 4.2 Porphycene on a Cu(111) surface

Porphycene molecules adsorb on Cu(111) as isolated molecules at room temperature and no islands or clusters are observed, as shown in figure 4.1a, similar to the adsorption of porphine molecules on a Ag(111) surface [112]. A typical STM image of a single porphycene molecule adsorbed on the Cu(111) terrace is displayed in Figure 4.1b. Two point symmetric protrusions can be observed. In comparison to the structure of the porphycene this is consistent with the symmetry of a flat adsorbed *trans* tautomer of porphycene, as shown in figure 4.1c, suggesting a *trans* tautomeric state for porphycene on Cu(111). In total, six differently orientated porphycene molecules can be identified which matches the threefold Cu(111) surface geometry and the two possible hydrogen atom arrangements in the *trans* state of a porphycene molecule. It should be noted that the porphycene molecules at the step edge show a different appearance that corresponds to the *cis* tautomer, as shown in figure 4.1d, which was also observed on the Cu(110) surface [24, 25] (see section 2.3).

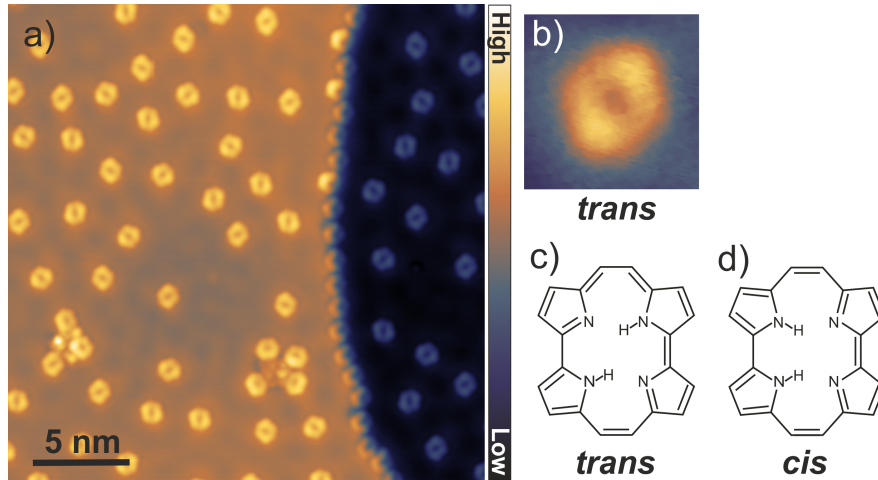


Figure 4.1: Porphycene on Cu(111). a) STM image of porphycene molecules on Cu(111) after sample preparation ( $V_s = -50\text{ mV}$ ;  $I_t = 50\text{ pA}$  color scale:  $0\text{ pm} - 400\text{ pm}$ ). b) STM image of single porphycene molecule on the Cu(111) terrace. c) and d) chemical structure of porphycene in the *trans* and *cis* state, respectively. All porphycene molecules on the Cu(111) terraces are in the *trans* tautomeric state (Note that molecules next to defects represent an exceptional case).

### 4.3 Vibrationally induced tautomerization of porphycene

The porphycene molecules show a stationary appearance and adsorption position during STM imaging at low bias voltages. However, at application of higher bias voltages the porphycene changes its configuration, as shown in figure 4.2. A bias voltage pulse of  $-280\text{ mV}$  was applied for  $100\text{ ms}$  at the upper left molecule in figure 4.2a (indicated by the black star) which changed the appearance of the molecule to an asymmetric single protrusion with one symmetry axis, see figure 4.2b. In comparison to the chemical structure of porphycene (see figure 4.1c, d) and the appearance of porphycene on Cu(110) [24, 25], see section 2.3, the molecule can be identified as *cis* tautomer of porphycene. Inducing another bias

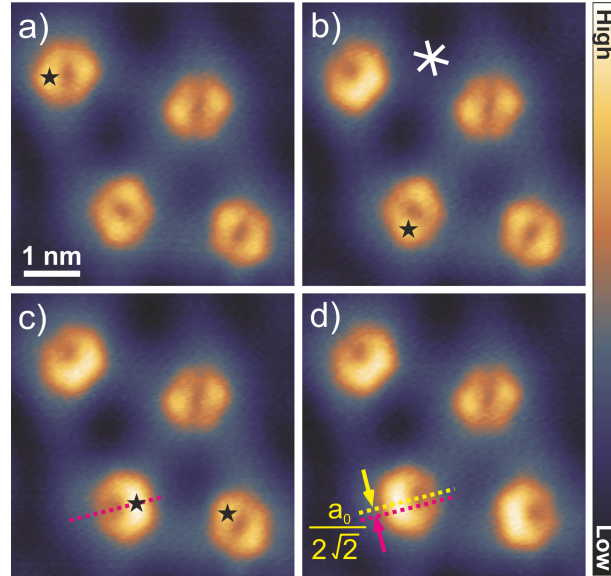


Figure 4.2: Voltage pulse induced tautomerization of a single porphycene molecule. a) STM image of porphycene molecules in the *trans* state. A bias voltage pulse of  $-280\text{ mV}$  was applied for  $100\text{ ms}$  above one of the protrusions of the upper left *trans* molecule, as indicated by the star. b) The pulse changed the molecule to an asymmetric appeared *cis* porphycene which follows the orientation of the high symmetry axis of the Cu(111) surface indicated by white lines. c) A further bias voltage pulse on the lower left molecule (see star in b) tautomerizes it to a differently orientated *cis* state. d) Application of a bias voltage pulse on a *cis* state molecule (lower left in molecule in c) induces a tautomerization to a mirror symmetric *cis* state. The *cis*  $\leftrightarrow$  *cis* tautomerization involves a slight movement of  $\sim 0.14\text{ nm}$  ( $\approx a_0/2\sqrt{2}$ ) along the surface high symmetry axis. Image parameters:  $V_s = -100\text{ mV}$ ;  $I_t = 100\text{ pA}$ ; the color scale ranges from  $-15$  to  $82\text{ pm}$ .

voltage pulse to the lower left molecule (see figure 4.2b) tautomerizes it to a differently orientated *cis* molecule. In total, six differently orientated *cis* porphycene molecules can be found on the Cu(111) surface. Analog to the six *trans* states, this matches the threefold Cu(111) surface geometry and the two possible hydrogen atom arrangements in the *cis* state of a porphycene molecule. Application of a bias voltage pulse on this *cis* state porphycene lead to a mirror symmetric *cis* tautomer, indicating a  $cis \leftrightarrow cis$  tautomerization. The  $cis \leftrightarrow cis$  tautomerization showed a slight movement of the porphycene molecule of  $\sim 0.14 \text{ nm}$  ( $\approx a_0/2\sqrt{2}$ ) along the Cu(111) high symmetry axis, with  $a_0$  the Cu lattice constant [113].

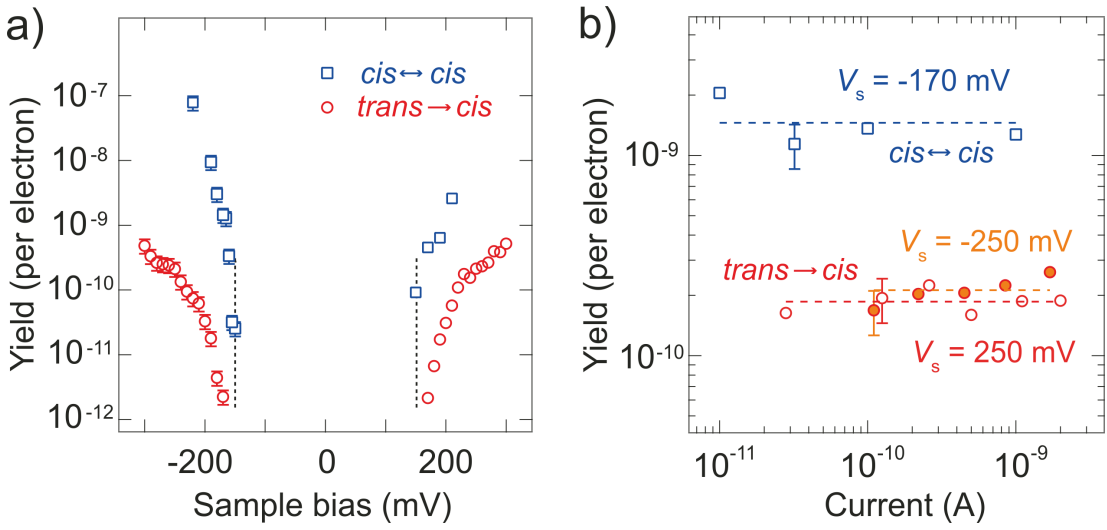


Figure 4.3: Voltage and current dependence of the voltage pulse induced single molecule tautomerization. a) Voltage dependence of the tautomerization yields of the  $trans \rightarrow cis$  (red circles) and  $cis \leftrightarrow cis$  (blue squares) tautomerization. The tautomerization yield is symmetric for positive and negative bias voltages and has a threshold voltage of around  $\pm 160 \text{ mV}$  for the  $trans \rightarrow cis$  and around  $\pm 150 \text{ mV}$  for the  $cis \leftrightarrow cis$  tautomerization. b) Current dependence of the  $trans \rightarrow cis$  (red unfilled and orange filled circles) and  $cis \leftrightarrow cis$  (blue squares) tautomerization yields at a bias voltage of  $250 \text{ mV}$ ,  $-250 \text{ mV}$ , and  $-170 \text{ mV}$ , respectively.

In figure 4.3a the voltage dependence of the voltage pulse induced  $trans \rightarrow cis$  and  $cis \leftrightarrow cis$  tautomerization is shown. A symmetric behavior for positive and negative voltages and a clear threshold voltage of around  $\pm 160 \text{ mV}$  and  $\pm 150 \text{ mV}$  can be identified for the  $trans \rightarrow cis$  and  $cis \leftrightarrow cis$  tautomerization yields, respectively. The current dependence of the tautomerization yields (shown in figure 4.2b) is constant, indicating a one electron process. The voltage and current dependences suggest the excitation of molecular vibrations via an inelastic electron tunneling process, as observed for porphycene on Cu(110) [24, 25]. An excitation

from the HOMO to the LUMO seems unlikely due to the high energy gap of around  $2.2\text{ eV}$  for porphycene in the gas phase [114].

## 4.4 Thermally induced tautomerization of porphycene

By thermal excitation all *cis* molecules can be switched back to the *trans* state and also the *cis*  $\leftrightarrow$  *cis* tautomerization can be induced reversibly. In figure 4.4a the temperature dependence of the tautomerization rate is plotted and can be analyzed by the Arrhenius equation  $R \propto \exp(-\Delta E/k_B T)$ , with  $R$  the thermally induced tautomerization rate,  $\Delta E$  the energy barrier of the process,  $k_B$  the Boltzmann constant, and  $T$  the temperature. Fitting the data by the Arrhenius equation determines  $\Delta E = 42(\pm 3)\text{ meV}$  and  $\Delta E = 35(\pm 9)\text{ meV}$  for the *cis*  $\rightarrow$  *trans* and *cis*  $\leftrightarrow$  *cis* energy barrier, respectively (see figure 4.4c). Due to the limited measurable temperature range of the *cis*  $\leftrightarrow$  *cis* tautomerization, this experimental error is larger. Note that we confirmed the tunneling current independence of the thermal induced tautomerization rate and can therefore exclude influences from the presence of the STM tip.

Figure 4.4b summarizes the vibrationally and thermally induced tautomerization processes. The *trans* tautomeric state is thermodynamically stable while the *cis* state is metastable. The *trans*  $\rightarrow$  *cis* and the backward *cis*  $\rightarrow$  *trans* tautomerization can be selectively induced by vibrational and thermal excitation and the *cis*  $\leftrightarrow$  *cis* tautomerization shows a reversible tautomerization for both excitation processes. The *trans*  $\rightarrow$  *cis* tautomerization was not observed during the thermal excitation which can be rationalized by the limited time resolution of the STM of around a few hundred microseconds. At elevated temperatures the metastable *cis* state switches back to the *trans* state before the STM can capture the intermediate existence in the *cis* tautomeric state. Interestingly, the *cis*  $\rightarrow$  *trans* tautomerization can not be induced by a voltage pulse and the reason for this remains unclear. Even if the thermal tautomerization barrier of the *cis*  $\leftrightarrow$  *cis* tautomerization is smaller than the barrier for the *trans*  $\rightarrow$  *cis* tautomerization, the absence of the voltage pulse induced *cis*  $\rightarrow$  *trans* tautomerization process is not straightforward, as the threshold voltages for the inelastic tunneling processes are with around  $150\text{ mV}$  and  $160\text{ mV}$  much higher than the thermal barrier of around  $42\text{ meV}$ . However, vibrational excitation via an inelastic electron tunneling process differs from a thermal excitation process and it is not trivial to compare them directly. The high tautomerization barrier for the vibrationally

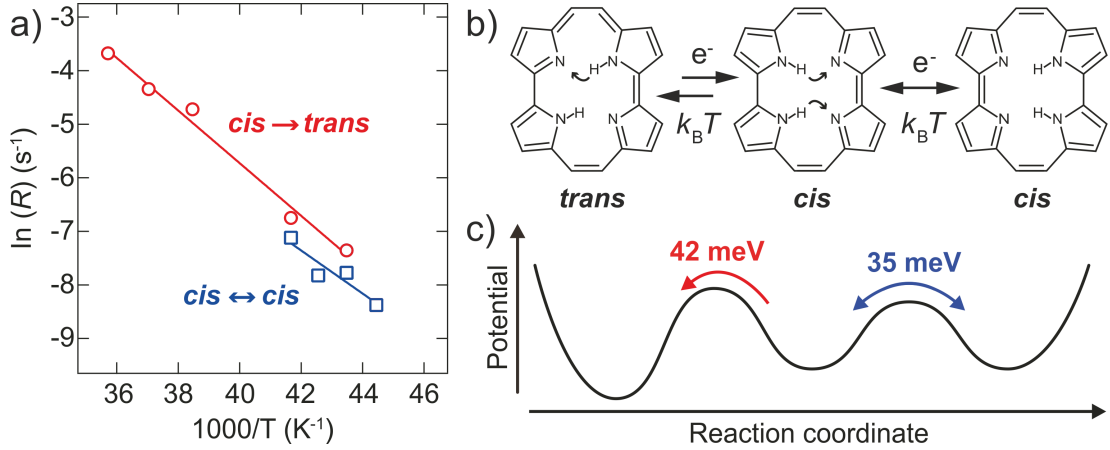


Figure 4.4: Thermally induced tautomerization of porphycene molecules. a) Arrhenius plot of the  $cis \rightarrow trans$  (red circles) and  $cis \leftrightarrow cis$  (blue squares) tautomerization rates (Measurement condition for the rates:  $V_s < 50 \text{ mV}$ ;  $I_t < 50 \text{ pA}$ ). b) The chemical structure of the porphycene can be selectively tautomerized from  $trans \rightarrow cis$  by voltage pulse induced STM ( $e^-$ ) excitation and backward from  $cis \rightarrow trans$  by thermal excitation ( $k_B T$ ). The  $cis \leftrightarrow cis$  tautomerization can be induced reversibly by STM and thermal excitation. c) The Arrhenius fit (in a) determines a tautomerization barrier of  $42 (\pm 3) \text{ meV}$  and  $35 (\pm 9) \text{ meV}$  for the  $cis \rightarrow trans$  and the  $cis \leftrightarrow cis$  tautomerization process, respectively.

induced tautomerization indicates that this tautomerization involves the excitation of a higher frequency mode via anharmonic coupling, which can substantially influence an induced reaction processes [115]. The different barrier heights for the vibrationally and thermally induced tautomerization suggest that the reactions take place via different excitation pathways within the multidimensional potential landscape of the tautomerization. To clarify this behavior, a detailed determination of the induced vibrational modes and a calculation of the multidimensional potential landscape including anharmonicity would be required.

## 4.5 Hot carrier-induced nonlocal tautomerization

In addition to the voltage pulse induced switching of single molecules located directly under the tip, we also observed tautomerization of molecules not located under the tip apex. In figure 4.5a an STM image directly after sample preparation is shown, all porphycene molecules are in the *trans* state. The same area is scanned after the application of a bias voltage pulse of  $-1.5 \text{ V}$  for  $50 \text{ ms}$  at the center of the image (with gap conditions of  $V_s = -50 \text{ mV}$  and  $I_t = 100 \text{ pA}$ ),

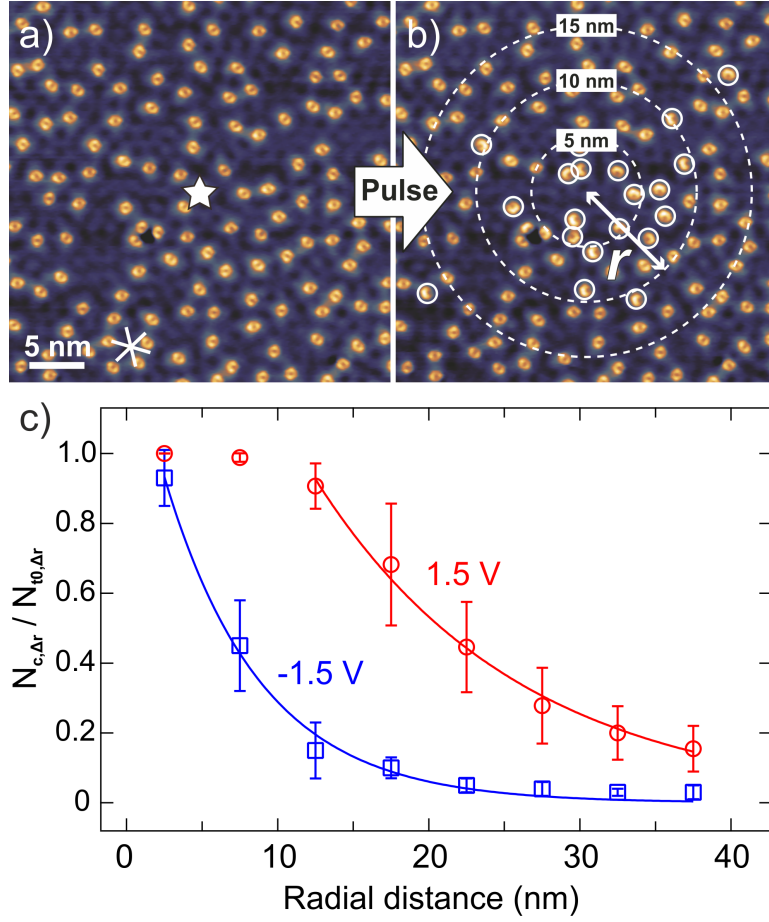


Figure 4.5: Nonlocal STM induced tautomerization. a) STM image of porphycene molecules after the sample preparation. All molecules are in the *trans* state. The white lines indicate the Cu(111) high symmetry axis. b) The same area after application of a  $-1.5\text{ V}$  voltage pulse for  $50\text{ ms}$  (gap conditions:  $V_s = -50\text{ mV}$ ;  $I_t = 100\text{ pA}$ ) at the center of the image (indicated by the star in a). Some of the porphycene molecules are converted to the *cis* tautomeric state (marked by white circles). The dashed circles show the radial distance  $r$  to the pulse at the center of the image. c) Tautomerization efficiency in radial distance dependence  $N_{c,\Delta r}/N_{t0,\Delta r}$  of a pulse of  $1.5\text{ V}$  (red circles) and  $-1.5\text{ V}$  (blue squares) for  $50\text{ ms}$  at the center of the image (gap conditions:  $V_s = -50\text{ mV}$ ;  $I_t = 100\text{ pA}$  and porphycene coverage of  $0.15 (\pm 0.005)\text{ nm}^{-2}$ ). The tautomerization efficiency  $N_c/N_{t0}$  represents the number of successfully tautomerized *cis* molecules  $N_c$  with respect to the initially available *trans* porphycene molecules before the pulse  $N_{t0}$  and is plotted with respect to their distance to the pulse in circular rings with a radial width  $\Delta r$  of  $5\text{ nm}$ . The data is fitted with an exponential decay.

shown in figure 4.5b. Some of the molecules are not in the *trans* state anymore and tautomerized to the *cis* state (indicated by the circles in figure 4.5b). This

nonlocal tautomerization was observed for molecules up to  $100\text{nm}$  away from the tip position depending on the voltage pulse parameters. It should be noted that also the  $cis \leftrightarrow cis$  tautomerization can be induced nonlocally, but the following will concentrate on the nonlocal  $trans \rightarrow cis$  tautomerization. Figure 4.5c shows the tautomerization efficiency in radial distance dependence  $N_{c,\Delta r}/N_{t0,\Delta r}$  of a voltage pulse of  $-1.5\text{ V}$  ( $1.5\text{ V}$ ). The tautomerization efficiency  $N_c/N_{t0}$  of successfully tautomerized  $cis$  molecules  $N_c$  with respect to the initially available  $trans$  molecules  $N_{t0}$  before the pulse is determined in circular ring areas with a radial width  $\Delta r$  of  $5\text{ nm}$  and plotted in radial distance dependence  $r$  to the pulse. In total 14 (4) experiments with around 10000 (3000) molecules were analyzed for a voltage pulse of  $-1.5\text{ V}$  ( $1.5\text{ V}$ ), respectively. The tautomerization efficiency shows a clear bias voltage dependence; a positive voltage pulse induces the tautomerization process more efficiently than a negative voltage pulse. The radial distance  $r$  behavior has an exponential decay  $e^{-r/\lambda}$ , with a decay constant  $\lambda$  of around  $13.5\text{ nm}$  ( $6.5\text{ nm}$ ) for a pulse of  $-1.5\text{ V}$  ( $1.5\text{ V}$ ), respectively (note that the exponential of the  $1.5\text{ V}$  pulse data is fitted with an offset due to the saturation behavior for  $r < 12.5\text{ nm}$ ).

#### 4.5.1 Tautomerization next to step edges

The nonlocal tautomerization raises the question of the mechanism that induces the tautomerization. Literature suggests the electric field of the STM tip [101, 105–108] or tunneling current induced hot carriers [30–33] as possible excitation mechanisms for the nonlocal reaction process. To distinguish between an electric field and a hot carrier-induced process the nonlocal tautomerization was excited next to step edges. As shown in figure 4.6, the tip was placed on the lower terrace next to a step edge. In this configuration the distance dependent electric field of the STM tip should be higher on the upper terrace than on the lower one. In contrast to this, the exponential distant dependent tunneling current is injected into the lower terrace and induces hot carriers there. The propagation of the hot carriers might be disturbed by the step edge suggesting a higher amount of hot carriers on the lower terrace. To eliminate geometric effects of the tip, we repeated the experiment next to differently orientated steps and changed the tip apex by dipping it slightly into the Cu surface. Figure 4.6 shows the tautomerization efficiency  $N_c/N_{t0}$  on the upper and lower terrace after the voltage pulse for the repeated experiments. The lower terrace shows an around 25 % higher tautomerization efficiency than the upper terrace, suggesting a hot carrier-induced process. Furthermore, the nonlocal tautomerization showed the



same behavior even though very different STM tips prepared by mechanical cut, mechanically polished and electrochemical etched platinumiridium wire were used (see section 3.4.3). These contradicts an electric field induced mechanism as the electric field should depend on the tip shape [116].

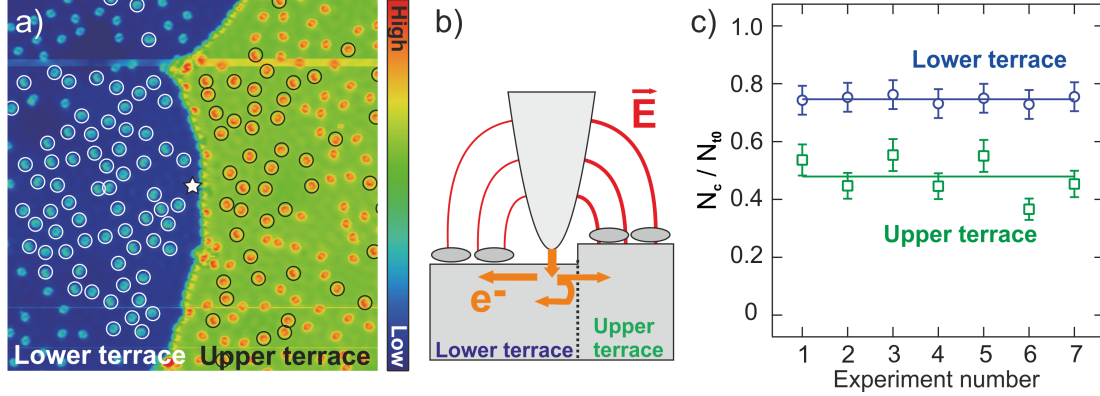


Figure 4.6: Hot carrier-induced nonlocal tautomerization next to a step edge. a) STM image after a bias voltage pulse of  $1\text{ V}$  for  $1\text{ s}$  with  $I_t = 100\text{ pA}$  at the lower terrace  $\sim 1\text{ nm}$  next to a step edge (indicated by the star). Tautomerized molecules in the *cis* state are marked with white (lower terrace) and black (upper terrace) circles (image parameters:  $V_s = -50\text{ mV}$ ;  $I_t = 50\text{ pA}$ ; size:  $(45\text{ nm})^2$ ; color scale from  $-0.01\text{ nm}$  to  $0.37\text{ nm}$ ). b) Schematic sketch of the experiment: The voltage pulse is induced next to a mono atomic step edge on the lower terrace. The shorter tip-surface distance results in a higher electric field above the upper terrace. The tunneling current induced hot carriers are injected to the lower terrace and their propagation might be hindered by the step. c) Tautomerization efficiency  $N_c/N_{t0}$  at the lower (blue circles) and upper (green squares) terrace after the voltage pulse at the lower terrace for different measurements (pulse parameters as in a). The higher tautomerization efficiency at the lower terrace suggests a hot carrier-induced tautomerization process.

#### 4.5.2 Tautomerization induced through conductive clusters

Additional to nonlocal excitation next to step edges, pulse injection into conductive clusters can reveal a hot electron induced process as shown by Maksymovych and co-workers (see section 4.1.2) [31]. An STM image of an exemplary conductive cluster is shown in figure 4.7a and the experiment configurations are schematically sketched in figure 4.7b. Voltage pulses were injected into the surface with the STM tip placed at three different configurations: over the clean Cu surface, see figure 4.7b (i), over a conductive cluster of height  $d_{\text{cluster}}$ , see figure 4.7b (ii), and over the clean surface with the same tip-surface distance as over the cluster,



see figure 4.7b (iii). When the tip is placed over a conductive cluster it retracts from the clean surface by the height of the cluster (around  $0.25 - 0.7 \text{ nm}$ ) and the increased tip-surface distance reduces the electric field on the surface, see figure 4.7b (ii), compared to an STM tip over the clean surface with the same tunneling current (constant current mode), see figure 4.7b (i). The same electric field on the surface as with the STM tip over the cluster can be expected with the same tip-surface height which leads, in absence of the cluster, to a lower tunneling current, see figure 4.7b (iii). Figure 4.7c shows the tautomerization efficiency in radial dependence for the three experimental configurations. No difference can be identified for measurements with the same tunneling current. Furthermore, with the reduced tunneling current no tautomerization can be observed in absence of the cluster, even though the same electric field can be expected for the same tip-sample distance with and without cluster. These results indicate a negligible influence of the electric field on the tautomerization and suggesting a hot carrier-induced tautomerization process.

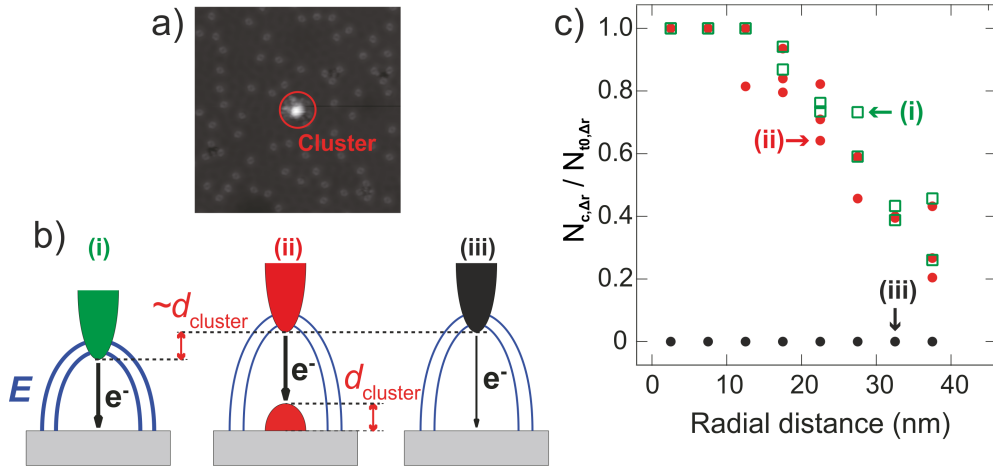


Figure 4.7: Tautomerization induced through conductive clusters. a) STM image of porphycene molecules on Cu(111) with a conductive cluster. b) Configurations of the experiment with the STM tip placed (i) over the clean Cu(111) surface, (ii) over the conductive cluster with an increased tip-sample distance of  $d_{cluster}$  which corresponds to the height of the cluster, and (iii) over the clean Cu(111) surface with the same tip-sample height as in (ii). c) Tautomerization efficiency ( $N_{c,\Delta r}/N_{t0,\Delta r}$ ) in radial dependence for the experiment configurations sketched in b). A bias voltage pulse of  $1.5 \text{ V}$  was injected for  $50 \text{ ms}$ . The tip height in (i) and (ii) was given by an STM set point of  $V_s = -50 \text{ mV}$  and  $I_t = 100 \text{ pA}$ , for (iii) the tip was retracted by  $d_{cluster}$  from this STM set point.

### 4.5.3 Tip-sample distance dependence of the tautomerization

For a hot carrier-induced nonlocal process the tautomerization efficiency should follow the exponential dependence of the tunneling current on the tip-sample distance. The tip-surface distance dependence of an averaged tautomerization efficiency over an area of  $50 \times 50 \text{ nm}^2$  in dependence of the tip-sample distance is shown in figure 4.8. It can be fitted by an exponentially decreasing tautomerization efficiency with a decay constant of  $5 \text{ nm}^{-1}$  which is comparable to the exponential decrease of the tunneling current with  $10 \text{ nm}^{-1}$  [117]. Here, the deviation of the decay constants may result from an underestimation of the tautomerization efficiency at short tip-sample distances due to a saturation around the pulse at the center of the image.

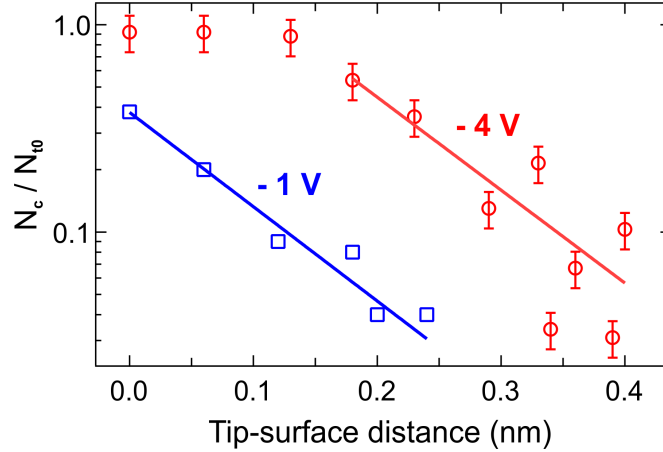


Figure 4.8: Tautomerization efficiency in tip-surface distance dependence. The tautomerization efficiency ( $N_c/N_{t0}$ ) is averaged over an area of  $(50 \text{ nm})^2$  after a voltage pulse of  $-1 \text{ V}$  (blue squares) and  $-4 \text{ V}$  (red circles) with  $50 \text{ ms}$  duration. The tip height is given with respect to a STM set point of  $V_s = 50 \text{ mV}$  and  $I_t = 3 \text{ nA}$  as zero-point. The data is fitted by an exponential decay.

### 4.5.4 Efficient hot carrier transport through the surface state

In previous studies the main transport channel for the hot carriers remained weakly understood [31, 33] and a contribution of bulk states was discussed [31], as they behave similar to surface states at the edge of the projection band [109]. To investigate efficient transport channels for the hot carriers, the tautomeriza-

tion efficiency can be compared to the local density of states of the surface. In figure 4.9 the bias voltage dependence of the tautomerization efficiency  $N_c/N_{t0}$  and a  $dI/dV$  spectrum of the Cu surface is shown. The tautomerization efficiency is averaged over an image area of  $(80\text{ nm})^2$  after a pulse at the center of the image with the plotted bias voltage for 1 s at a constant current of  $250\text{ pA}$ . For positive bias voltage (corresponding to electron injection) a much higher tautomerization efficiency is detected than for negative bias voltages (corresponding to hole injection). The  $dI/dV$  spectroscopy shows the Cu(111) surface state at  $-0.4\text{ V}$  (see also the inset of figure 4.9b) [34] and a drastic increase of the signal at negative bias voltages of  $> 2.5\text{ V}$  indicating the  $d$  bands of the Cu surface [118]. The tautomerization efficiency does not show an increasing intensity at the presence of the Cu  $d$  bands and shows up to  $-4\text{ V}$  lower efficiency than for  $1\text{ V}$ , suggesting that the Cu  $d$  bands do not contribute significantly to the hot carrier transport. Therefore the Cu(111) surface state supports a very efficient transport of hot electrons compared to the transport of hot holes.

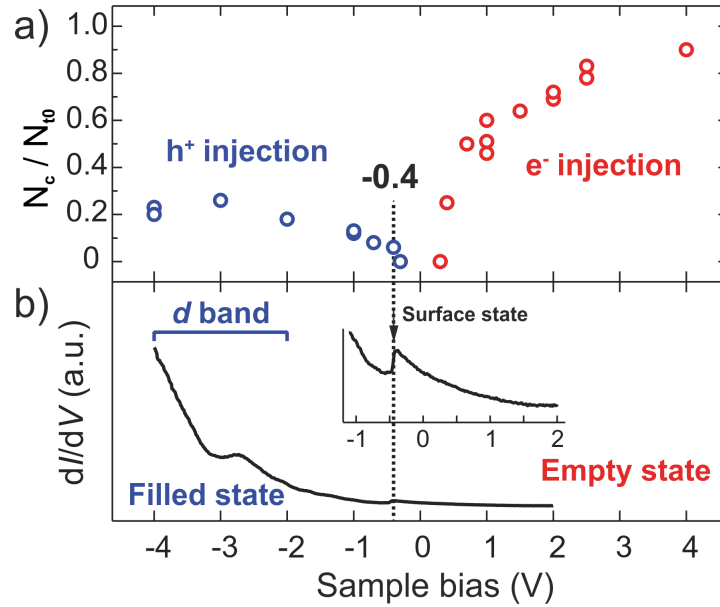


Figure 4.9: Voltage dependence of the hot carrier-induced tautomerization. a) Tautomerization efficiency  $N_c/N_{t0}$  in dependence of the pulse bias voltage. The tautomerization efficiency is averaged over an image area of  $(80\text{ nm})^2$  after a bias voltage pulse for 1 s with the indicated voltage at a constant current of  $250\text{ pA}$ . b)  $dI/dV$  spectroscopy of Cu(111). The Cu(111) surface state is resolved as a step like feature at  $-0.4\text{ V}$  (this voltage area is magnified in the inset) and the Cu(111)  $d$  bands show an increasing contrast at negative sample bias voltages.

## 4.6 Coverage dependence of the nonlocal tautomerization

The surface state can be affected by adsorbed molecules and vice versa. STM has been used to investigate such phenomena locally [119,120]. Figure 4.10 shows the coverage dependence of the nearest neighbor distance between the molecules. At very low coverages of  $0.03 \text{ nm}^{-2}$  (red histogram in figure 4.10a and STM image figure 4.10b) the nearest neighbor distance shows a multiple peak structure with a first peak at  $2.5 \text{ nm}$ , a second peak at  $3.8 \text{ nm}$ , a third peak at  $5.0 \text{ nm}$ , and a fourth peak at  $6.3 \text{ nm}$ , indicating an oscillatory behavior with a period of  $1.3(\pm 0.1) \text{ nm}$ . This corresponds well to half of the Fermi wavelength of the Cu(111) surface state, suggesting a surface state mediated long-range ordering [110,121–123] as reported

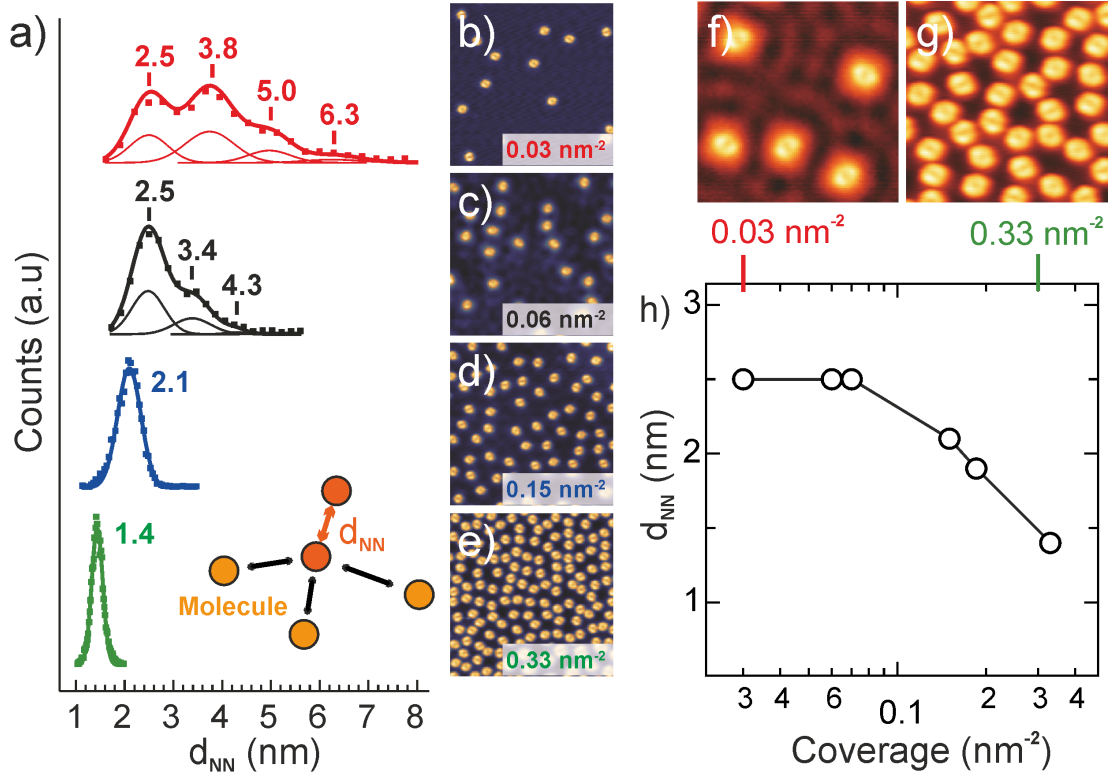


Figure 4.10: Coverage dependence of the nearest neighbor distance. a) Histogram of the nearest neighbor distances  $d_{NN}$  at a molecular coverage of  $0.03(\pm 0.005) \text{ nm}^{-2}$  (red),  $0.06(\pm 0.005) \text{ nm}^{-2}$  (black),  $0.15(\pm 0.005) \text{ nm}^{-2}$  (blue), and  $0.33(\pm 0.005) \text{ nm}^{-2}$  (green). b)-e) STM images at the different coverages (image size:  $(20 \text{ nm})^2$ ). f) and g) STM images at a coverage of  $0.03 \text{ nm}^{-2}$  and  $0.33 \text{ nm}^{-2}$ , respectively (image size:  $(10 \text{ nm})^2$ ). h) Coverage dependence of the first peak of the nearest neighbor distribution.

for Cu atoms on a Cu(111) surface [110]. At low molecular coverage of  $0.06 \text{ nm}^{-2}$  (black in figure 4.10a and figure 4.10c) the nearest neighbor distance also shows a multiple peak structure with a first peak at  $2.5 \text{ nm}$ , indicating the presence of long-range ordering. Note that the smaller oscillation period results from the fact that the nearest neighbor distance histogram is a first order approximation of the general molecular distance histogram, which only allows reasonable interpretation of the second and further peak positions in a very low coverage limit. At higher coverages of  $0.15 \text{ nm}^{-2}$  (blue in figure 4.10a and figure 4.10d) and very high coverages of  $0.33 \text{ nm}^{-2}$  (green in figure 4.10a and figure 4.10e) a single peak at  $2.1 \text{ nm}$  and  $1.4 \text{ nm}$  can be observed. At these high coverages the substrate mediated optimal distance can not be fulfilled anymore due to too many adsorbed molecules on the surface. The molecules order with equal distance separation and lead to a single peak in the nearest neighbor histogram with decreasing distance for higher coverages. In summary, different molecular ordering can be identified at low and high molecular coverages with a threshold coverage of around  $0.1 \text{ nm}^{-2}$ , whereby at low coverages the Cu surface state mediates the adsorption positions of the porphycene molecules. Indications of the surface state mediated ordering can also be seen on the STM images at low coverages: The surface state scatters at the molecules and the resulting interference pattern can be imaged. At high coverages this behavior cannot be observed anymore due to the high molecular density. This raises the question whether the surface state is affected by a high molecular coverage. Here, the STM setup provides the possibility to locally investigate the Cu surface state with  $dI/dV$  spectroscopy. The blue spectrum in figure 4.11c shows the  $dI/dV$  of the Cu surface in surrounding of a high coverage of molecules, as indicated in the STM image in figure 4.11a. No Cu surface state can be detected. The same Cu spectrum is taken again after manipulating the directly neighboring porphycene molecules away (see figure 4.11b) and the Cu surface state can be observed (see red  $dI/dV$  spectrum in figure 4.11c). This indicates that the high molecular coverage quenches the surface state locally.

The previously discussed results show an especially efficient propagation of the hot carriers through the surface state raising the issue of a possible influence of the molecular coverage on the nonlocal hot carrier-induced tautomerization. To separate the observations of the single molecule tautomerization and the hot carrier-induced nonlocal tautomerization, first the single molecule tautomerization is investigated in coverage dependence, this is shown in the inset of figure 4.12. The tautomerization yield is constant for low and high molecular coverages, indicating a coverage independent tautomerization efficiency at the single

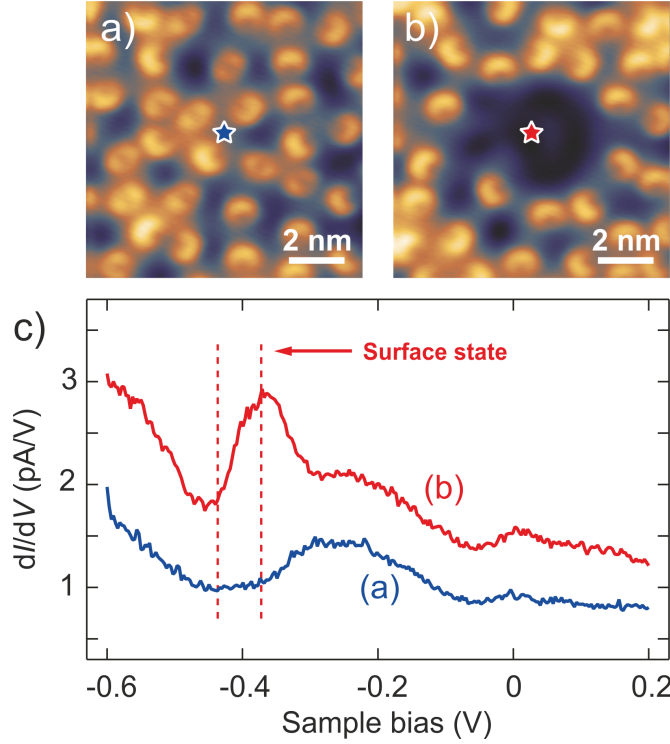


Figure 4.11: Local surface state quenching at high molecular coverage. a) STM image of porphycene molecules with a molecular coverage of around  $0.30 \text{ nm}^{-2}$ . ( $V_s = 50 \text{ mV}$ ;  $I_t = 50 \text{ pA}$ ; image size:  $(10 \text{ nm})^2$ ). b) STM image of the same area after manipulating the molecules away from the center of the image. c)  $dI/dV$  spectroscopy measured over the bare Cu surface next to high molecular coverage (blue) and at the same position after manipulating the neighboring molecules away (red), the measurement position is indicated by stars in a) and b), respectively. The Cu surface state is quenched at high molecular coverage and recovers after creation of a locally low molecular coverage.

molecular level. Figure 4.12 shows the nonlocal hot carrier-induced tautomerization efficiency  $N_c/N_{t0}$  at a pulse voltage of  $300 \text{ mV}$  in time-evolution at four different molecular coverages of  $0.03 \text{ nm}^{-2}$ ,  $0.06 \text{ nm}^{-2}$ ,  $0.15 \text{ nm}^{-2}$ , and  $0.33 \text{ nm}^{-2}$ . The coverages of  $0.03 \text{ nm}^{-2}$  and  $0.15 \text{ nm}^{-2}$  are measured with different tip conditions (the tip was changed by dipping it slightly into the surface) as indicated by the open and filled markers in figure 4.12. For the different tip conditions no differences in the time evolution tautomerization efficiency can be determined, suggesting a negligible influence of the tip conditions.

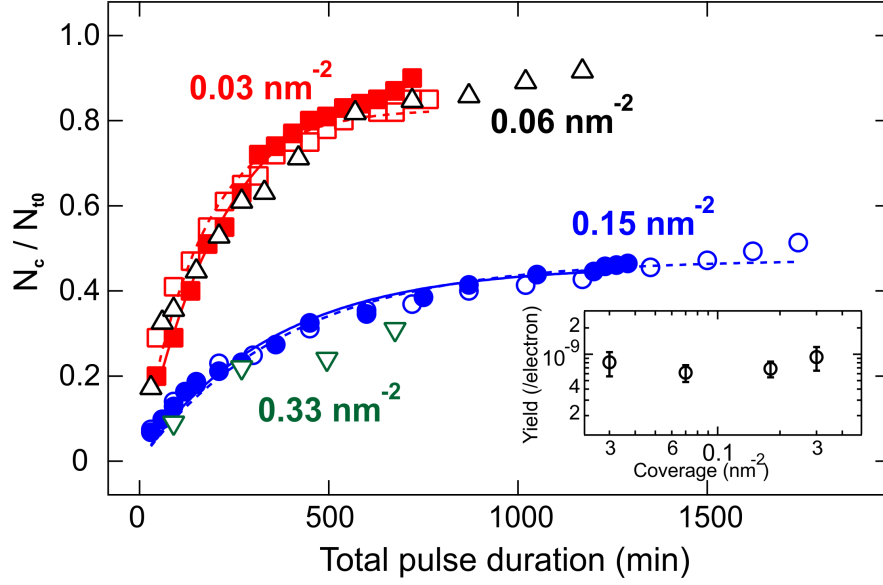


Figure 4.12: Coverage dependence of the hot carrier-induced tautomerization. Voltage pulse time-evolution of the hot carrier-induced tautomerization efficiency at a coverage of  $0.03(\pm 0.005) \text{ nm}^{-2}$  (red squares),  $0.06(\pm 0.005) \text{ nm}^{-2}$  (black up pointing triangles),  $0.15(\pm 0.005) \text{ nm}^{-2}$  (blue circles), and  $0.33(\pm 0.005) \text{ nm}^{-2}$  (green down pointing triangles). The tautomerization efficiency  $N_c/N_{t0}$  is averaged over an image area of  $(70 \text{ nm})^2$  and a voltage pulse of  $300 \text{ mV}$  was applied at the center of the image with gap conditions of  $V_s = -50 \text{ mV}$  and  $I_t = 10 \text{ pA}$  (tunneling current during the pulse  $70(\pm 25) \text{ pA}$ ). The open and filled red squares (blue circles) represent the measurement with two different tips, the solid (broken) line show the data fit by equation 4.2. The inset shows the coverage independent *trans*  $\rightarrow$  *cis* tautomerization yield of a single molecule.

Coverage independent, the tautomerization efficiency shows a saturation behavior for long pulse durations, reflecting the limited local influence of the excitation pulses. The data can be described by using the rate equation [31]

$$\frac{dN_{c,r}}{dt} = k(N_{t0,r} - N_{c,r})I_r^n \quad (4.1)$$

where  $N_{c,r}$  ( $N_{t0,r}$ ) is the (initial) number of *cis* (*trans*) molecules at a radial distance  $r$ ,  $I_r$  the current at a distance  $r$ , and  $n$  the reaction order of the process. In terms of the tautomerization efficiency  $N_c/N_{t0}$  it can be expressed as

$$\frac{N_c}{N_{t0}} = N(\infty)(1 - e^{-kI_{eff}^n t}) \quad (4.2)$$

where  $N_c$  ( $N_{t0}$ ) is the (initial) number of *cis* (*trans*) molecules in the measured area,  $N(\infty)$  the tautomerization efficiency at a pulse time  $t = \infty$ , and  $I_{eff} = I_t \sum_r e^{-\frac{r}{\lambda}}$  the total number of effective hot carriers that induce the nonlocal tautomerization. For the fit of the tautomerization efficiency in figure 4.12 a reaction order of  $n = 1$  is assumed, as an one-electron process can be expected at an excitation voltage of 300 mV (see fig. 4.3). The fit of the tautomerization efficiency in time-evolution is shown by the solid (and dashed, representing a second tip condition) lines in red and blue in figure 4.12 and determined a total number of effective hot carriers  $kI_{eff} \sim 8.8(\pm 2) \times 10^{-5} s^{-1}$  and  $kI_{eff} \sim 4.5(\pm 1) \times 10^{-5} s^{-1}$  for the coverage of  $0.03 nm^{-2}$  and  $0.15 nm^{-2}$ , respectively.

The two low coverages of  $0.03 nm^{-2}$  and  $0.06 nm^{-2}$  show a more efficient tautomerization than the two high coverages of  $0.15 nm^{-2}$  and  $0.33 nm^{-2}$ . Interestingly, there is no clear difference in the tautomerization efficiency between the two low or the two high coverages, respectively, indicating a negligible influence of hot carrier scattering at the molecules where a monotonic coverage dependence would be expected. There seems to be a critical change of the tautomerization efficiency between the coverages of  $0.06 nm^{-2}$  and  $0.15 nm^{-2}$ , which reflects the characteristics of the coverage dependent interactions between the molecules and the Cu surface state. At low coverage the nonlocal tautomerization efficiency is higher, the molecules order to substrate mediated ideal positions, and the STM images show surface state scattering. In this case, the hot carriers can travel efficiently through the Cu surface state. At high coverage the tautomerization efficiency is reduced, the surface state mediated ordering is not present, and the STM images do not show surface state scattering patterns. Here, the local quenching of the surface state due to the high molecular coverage results in a less efficient hot carrier transport.



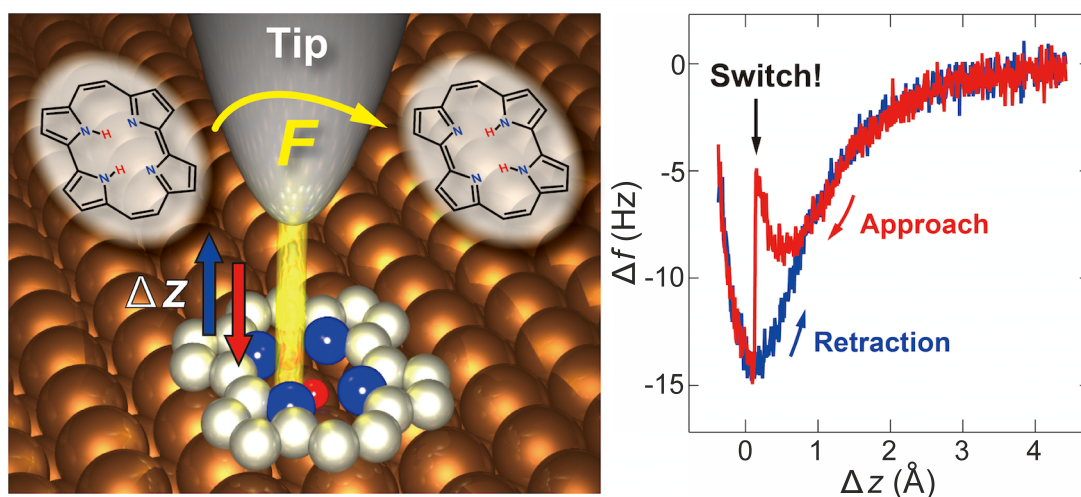
## 4.7 Summary

We investigated the vibrationally, thermally and hot carrier-induced tautomerization of porphycene molecules on a Cu(111) surface by LT-STM. After preparation, the porphycene molecules on the Cu(111) terraces are exclusively found in the *trans* tautomeric state. By the excitation of molecular vibrations via an inelastic electron tunneling process during a voltage pulse of the STM, single porphycene molecules could be switched from the *trans* to the *cis* tautomeric state and reversible between the two *cis* tautomeric states, involving a slight movement along the surface high symmetry axis. Temperature dependent measurements identified the *cis* tautomeric state as metastable, as all molecules could be thermally switched back to the *trans* state and determined the tautomerization barrier for the *cis*  $\rightarrow$  *trans* tautomerization to be around  $42\text{ meV}$  and the *cis*  $\leftrightarrow$  *cis* barrier around  $35\text{ meV}$ . Additionally, the tautomerization could be induced nonlocally in an area of up to  $100\text{ nm}$  by excitation of hot carriers. In this process, the Cu surface state was found to be a very efficient hot carrier traveling channel with a higher tautomerization efficiency for hot electrons than hot holes. The surface state was identified to influence the adsorption of the porphycene molecules and vice versa, resulting in a distinct change of the nonlocal tautomerization efficiency in dependence of the molecular coverage. At low coverages the porphycene molecules show a surface state mediated ordering and an efficient nonlocal tautomerization. In contrast to this, high porphycene coverages were identified to locally quench the surface state, leading to a less efficient hot carrier propagation and nonlocal tautomerization, which demonstrates the interplay between the molecule-surface interaction and the reaction efficiency. These results show the controlled operation of a single molecular switch on a metal surface in a local and nonlocal fashion and give microscopic insight into the mechanisms.



## Chapter 5

# Force-induced tautomerization in a single molecule



### Abstract

Chemical reactions are commonly activated by thermal, electric, and light energy. A force-induced mechanical activation would provide an additional way which is not understood on the atomic level. In this study we present a combination of low-temperature non-contact atomic force microscopy (AFM) and density functional theory (DFT) calculations which reveal the force-induced tautomerization of porphycene on Cu(110). The reversible bond rearrangement can be induced just by the interaction force between a Cu terminated AFM tip and the

molecule and can be controlled and quantified with a precision on the atomic scale. The DFT calculations showed the evolution of the reaction barrier in presence of the approaching tip and revealed the reaction mechanism on the atomic (submolecular) scale. The tautomerization was found to be absent in the case of a chemical inert Xe terminated tip, which showed much weaker interaction forces and strong relaxation of the tip apex, demonstrating the importance of the chemical and mechanical properties of the tip to induce a bond rearrangement catalytically with an AFM tip.

## 5.1 Introduction

### 5.1.1 Mechanochemistry

Chemical reactions are commonly activated by heat, light or electric energy. Mechanical force is another way to stimulate reactions, which defines the area of mechanochemistry [124] but is generally far less investigated compared to thermo-, electro-, and photochemistry. The presence and importance of mechanochemical reactions in nature can be captured very intuitively by the sense of touch, hearing or balance [125] and also their relevance in application and technology is obvious, as a key aspect for the lifetime of many products of daily life is determined by their mechanical stability. Recent research revealed that mechanochemical reactions can bias chemical reaction pathways, which cannot be achieved by other energy sources like heat or light [126], have a large potential application field in technology as for damage sensing or full regenerative self-healing [127, 128], and also play a key role for biochemical reactions, as they can activate biochemical reactions like protein binding [129]. In a mechanochemical process the selective bond breaking and formation is activated by a directional mechanical force. In mechanochemistry a mechanical force is defined as macroscopic (classical) force acting directional on the system, but the bond breaking and formation at the molecular level should be described in a quantum mechanical manner. Therefore, force-induced processes on the molecular scale can not be rationalized by a classical picture and should be understood as a process of chemical interactions.

Mechanochemical processes could exhibit a different selectivity from heat- and/or light-induced ones. For instance, Hickenboth and co-workers [126] found that the mechanochemical activation can bias reaction pathways, leading to spe-

cific products. The *trans* and *cis* isomers of a benzocyclobutene molecule placed within long polymer strands can be excited to a ring opening reaction. The excitation with light and thermal energy activates processes which preserve the molecular symmetry and lead to two final states. Mechanical activation via ultrasound biases the reaction pathways and leads to only one final isomer by inducing two different processes depending on the isomer state.

A technological application of mechanochemical reactions has been demonstrated for mechanosensitive polymers. Davis and co-workers showed polymers functionalized with mechanically sensitive groups, so-called mechanophores, can change the color by application of a directional force, which for example allows visualizing a location of mechanical stress in the polymer and could be used as damage sensor. Furthermore, Mechanophores in polymers could induce a variety of other responses to mechanical activation, as for example reorganizing the polymer and thereby strengthening it or the recently achieved highly effective self-healing after structural damage [128].

The importance of mechanical activation in biochemistry can be seen in the results by Rio and co-workers [129]. They showed that the mechanical stretching of a single protein molecule activates the binding of another protein. Using a magnetic tweezer and AFM, they investigated that the stretching of the talin protein, which links transmembrane receptors to the cytoskeleton, activates the binding of (additional) vinculin proteins. In this way a mechanical stimulus can activate a chemical response of a biological cell by reorganizing its cytoskeleton. The secondary structure of proteins, as for example the  $\alpha$ -helices in this case, is determined by a pattern of hydrogen bonds and the mechanical stretching of proteins proceeds via bond breaking and formation within this pattern. Therefore, this work also demonstrates the important role of hydrogen bonds in the mechanical activation in biochemistry.

Chemical reactions depend critically on the local environment up to the atomic scale. However, the majority of previous studies addressing mechanochemical reactions are employed spatially using averaging techniques, which cannot determine the influence of the local surrounding. The rare investigations at the single molecule level give first insights into the reactions of a single molecule under mechanical activation. But the studied biomolecules have complex structures out of many building blocks, which limits the information gain regarding the effects of the surroundings on the atomic scale. Here, NC-AFM has proven to be a powerful investigation tool and will be used in this study to investigate a mechanically induced reaction at the atomic scale.

### 5.1.2 Atomic scale force detection with AFM

Ever since its invention, AFM has been used to investigate forces locally, as for instance in the interaction force detection between single strands of DNA in 1994 [130]. In the beginning, dynamic AFM at RT showed the capability to detect forces on the atomic scale [56, 131, 132]. Recently, low-temperature NC-AFM was used for detecting forces at the atomic scale, for example the force needed to move a single atom [133–135] or molecule [133, 136] on metal [133, 136] or semiconductor surfaces [134, 135] or to peel of a molecular chain from a metal surface [137, 138] have been measured.

The force needed to manipulate a single atom on a metal surface was investigated by Ternes and co-workers by NC-AFM with a tuning fork sensor in q+ design [133]. With repeated constant height line scans and decreasing tip-sample distance, the tip measured the frequency shift due to the tip-sample interactions above the atom along the substrate direction of easiest manipulation. The (vertical) force and the interaction potential was determined by the Sader Jarvis method (by integrating along the tip height). Additionally, the lateral forces were calculated by differentiation of the interaction potential along the line scan direction. They quantified the force to move a single Co atom on a Pt(111) surface and the threshold force is estimated to be  $210 \pm 30 \text{ pN}$  in the lateral direction and is independent of the vertical force component. The experiment showed a high reproducibility and no atom moving for a  $5 \text{ pm}$  larger tip-sample distance and around  $\pm 5\%$  deviation in the threshold lateral force for different tips. The influence of the surface was demonstrated by moving Co atoms on a Cu(111) surface, which revealed a threshold lateral force of  $17 \pm 3 \text{ pN}$  and proved a high surface sensitivity.

Moreover, Ternes and co-workers measured the force to move a CO molecule [133] and found a lateral force of  $160 \pm 30 \text{ pN}$  needs to be applied to move a CO molecule on a Cu(111) surface, which is an order of magnitude larger than for moving a Co atom on the same surface. The force required to move a larger molecule was investigated by Langewisch and co-workers for a PTCDA molecule (3,4,9,10-perylene-tetracarboxylicacid-dianhydride) on Ag(111) [136]. They determined a lateral threshold force of around  $200 \text{ pN}$  to induce the manipulation to the next Ag lattice site in direction of the easiest manipulation. Even though a continuous force detection could be observed with a specific tip, all other tips which moved the molecule successfully showed discontinuities, which prevented the force analysis and indicates the importance of a stable relaxation free tip (and molecule) for detailed force detection measurements. Next to a sufficiently sta-

ble tip, a clearly defined molecular adsorption position and easiest manipulation direction must be present. Otherwise, the various molecular degrees of freedom of translation and rotation prevent the reproducibility of the force manipulation. This situation was reported by Mao and co-workers for the force manipulation of single phthalocyanine molecules on Pt(111), which do not adsorb in a specific adsorption position [139]. This leads to various manipulation pathways of translation and rotation with threshold forces between  $5\text{ pN}$  and  $17\text{ pN}$  and prevents reproducible manipulation force detection.

### 5.1.3 Model system for force-induced tautomerization

The research described above demonstrates the capability of NC-AFM to measure forces acting on the atomic scale, which are in the order of several  $\text{pN}$ . Even though the forces for moving, rotating or detaching molecules have been quantified for selected systems, there is a lack of studies of force-induced reversible bond rearrangement within a single molecule. The *cis* to *cis* tautomerization of porphycene on Cu(110) provides an intriguing model for experimental and theoretical force determination. The STM studies of porphycene on Cu(110) [24, 25], see section 2.3, revealed a stable adsorption in the *cis* tautomeric state. The vibrational and thermal induced tautomerization to the mirror symmetric *cis* state should be energetically degenerate [24], whereby the potential landscape could be significantly influenced by the local environment like the tip proximity and neighboring adatoms/molecules [25]. These results imply the possibility to distort the potential landscape drastically and to control the tautomerization by an AFM tip. Here, the reversibility of the tautomerization and the very small translation during the tautomerization builds a good basis for very defined and reproducible force measurements and simplify theoretical modeling, whereby the known DFT optimized structure of porphycene on the Cu(110) surface [25] provides a good basis for further calculations.

## 5.2 Force-induced *cis* to *cis* tautomerization

Porphycene adsorbs on a Cu(110) surface exclusively in the *cis* tautomeric state, as shown in the STM image in figure 5.1a (see section 2.3 for a summary of the previous STM and DFT study of the system). It was found that a reversible *cis* to *cis* tautomerization of a single porphycene molecule (see figures 5.1a-c) can be induced by approaching the tip towards the molecule even at 5 K and in absence of applied bias voltage, where no sufficient thermal or vibrational energy is present to induce the tautomerization.

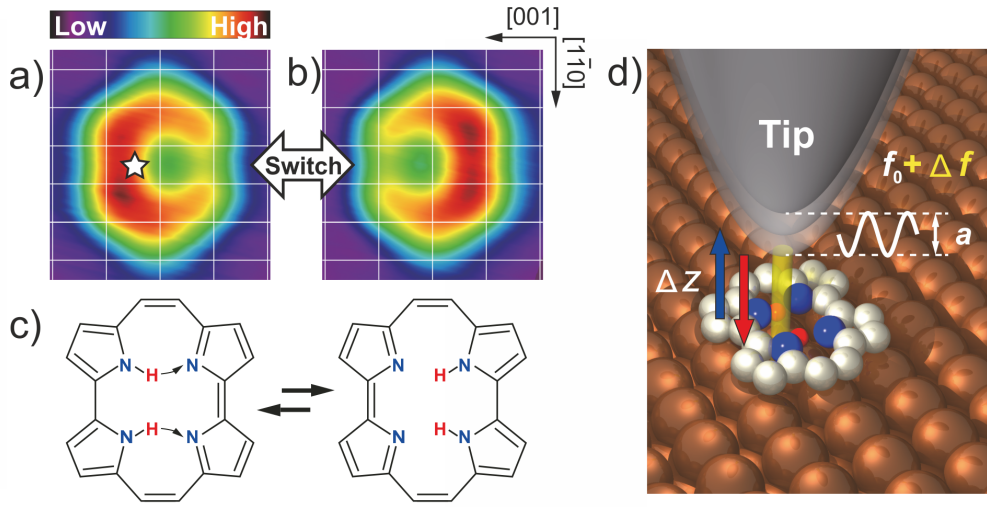


Figure 5.1: Porphycene molecule on Cu(110) and schematic of the force-induced tautomerization. a) STM image of a porphycene molecule on the Cu(110) surface in the *cis* tautomeric state. The with star indicates the tip position of the  $\Delta f(\Delta z)$  spectra in figure 5.2. b) STM image of the molecule after the *cis* to *cis* tautomerization. Image parameters:  $V_s = -100 \text{ mV}$ ,  $I_t = 10 \text{ nA}$ ; image size:  $1.49 \times 1.42 \text{ nm}^2$ . c) Molecular structure of the porphycene in the two mirror symmetric *cis* states in a) and b), respectively. The curved arrows show the intra molecular H atom transfer of the tautomerization. d) Schematic of the force measurement ( $\Delta f(\Delta z)$  spectra). The AFM tip oscillates at the resonance frequency  $f_0$  with an amplitude  $a$ . The tip is approached to (red arrow) and retracted from (blue arrow) the molecule and the interaction forces (yellow column) between tip and molecule are detected by the frequency shift  $\Delta f$  in dependence of the tip height  $\Delta z$ .

To investigate the nature of this intra molecular H atom transfer, we measured frequency shift spectra in dependence of the tip height ( $\Delta f(\Delta z)$ ) above the porphycene molecule with applying zero voltage during the measurement. A schematic sketch of the experiment is shown in figure 5.1d. The oscillating AFM



tip is approached and retracted over the porphycene molecule and the frequency shift probes the interaction forces between the tip and the molecule on the surface. It can be expected that the tip apex is covered by copper, because the tip was dipped into the Cu surface several times before the measurements (see section 3.4.3).

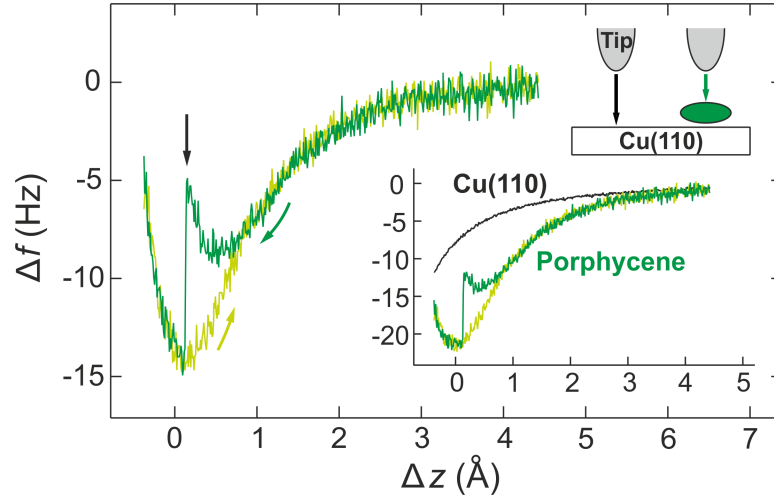


Figure 5.2:  $\Delta f(\Delta z)$  tautomerization spectra of porphycene on Cu(110). a) Frequency shift  $\Delta f$  approach (dark green) and retraction (light green) spectra in dependence of the tip height  $\Delta z$ . To exclude the tip-surface background forces, the spectra are background subtracted by a Cu(110) spectrum at the same starting tip-sample distance ( $\Delta z \sim 4.5 \text{ \AA}$ ) of an STM set point of  $V_{bias} = 100 \text{ mV}$  and  $I_t = 10 \text{ pA}$  over the Cu surface (see sketch). The porphycene spectra (green) before subtraction and the Cu(110) spectrum (black) are shown in the inset (same axis units). The tip height  $\Delta z$  is given with respect to  $z_e$  of the Morse potential model fit of the approach curve in figure 5.3a. Measurement parameters:  $a = 100 \text{ pm}$ ,  $f_0 = 22653 \text{ Hz}$ ,  $Q = 18274$  (tip 1).

An approach and retraction frequency shift spectrum ( $\Delta f(\Delta z)$ ) of the tautomerization is shown in figure 5.2. To separate the molecule tip interaction from the background surface tip interactions, the porphycene spectra are background subtracted by a  $\Delta f(\Delta z)$  spectra over the bare Cu surface at the same tip-sample distance (see the inset and schematic sketch of figure 5.2) [140, 141]. For this, the starting tip-sample distance (at around  $\Delta z = 4.5 \text{ \AA}$ ) was set in reference to an STM set point of  $V_{bias} = 100 \text{ mV}$  and  $I_t = 10 \text{ pA}$  over the bare Cu(110) surface. The STM set point was adjusted by the STM feedback over the Cu surface and the tip was then moved in constant height with disabled feedback over the molecule to measure the porphycene spectra. Note that  $\Delta z = 0$  is defined with respect to a Morse potential model fit shown in figure 5.3a, which will be dis-

cussed later on in this section. The frequency shift spectra shown in figure 5.2 were measured at the central area of the porphycene molecule with the tip above the part of the inner cavity where the H atoms are located. The tip position is shown by a star on the STM image in figure 5.1a. The backward subtracted approach frequency shift spectrum is shown in dark green in figure 5.2. Starting at the tip height of the reference set point, it exhibits more attractive interactions for closer tip-sample distances until it passes a minimum, as expected for a force measurement in distance dependence. At close tip-sample distance, the frequency shift spectrum shows a sudden jump to more attractive interactions. After the sudden jump, the frequency shift spectrum proceeds continuously and the retraction spectrum (plotted in light green) follows a different trajectory with stronger interactions at close tip-sample distances. STM imaging before and after the  $\Delta f(\Delta z)$  spectra show that this jump corresponds to a *cis* to *cis* tautomerization of the porphycene molecule. Analog to the temperature and voltage pulse induced *cis* to *cis* tautomerization [24], it was found to be reversible.

In figure 5.3 the force  $F(\Delta z)$  and the energy  $U(\Delta z)$  spectra calculated by the Sader and Jarvis method [86] are shown, and additionally, the tautomerization spectra of two further tips are plotted. The different tips were obtained by modification of the tip apex by applying voltage pulses and (/or) dipping the tip apex intentionally into the bare Cu surface, so-called tip forming. The force  $F(\Delta z)$  spectra in figure 5.3a are fitted by the Morse potential model  $U(z) = -E_d [2 \exp^{-\kappa(z-z_e)} - \exp^{-2\kappa(z-z_e)}]$  with  $E_d$  the bond energy,  $\kappa$  the decay constant, and  $z_e$  the equilibrium distance. The fit reproduces the experimental data very well. The force spectroscopy with different tips reveals that the tautomerization shows common characteristics independently of the specific tip properties. The  $F(\Delta z)$  jumps towards more attractive forces at the tautomerization and passes during the approach over the force minimum before the tautomerization (for the majority of tips). A main difference between tips is the total interaction strength between the tip and the sample, which leads to different interaction energies depending on the tip. We have investigated 21 different tips and found that the tautomerization threshold  $U_{th}$  varies between 230 meV and 630 meV, as shown in the histogram in figure 5.3b.

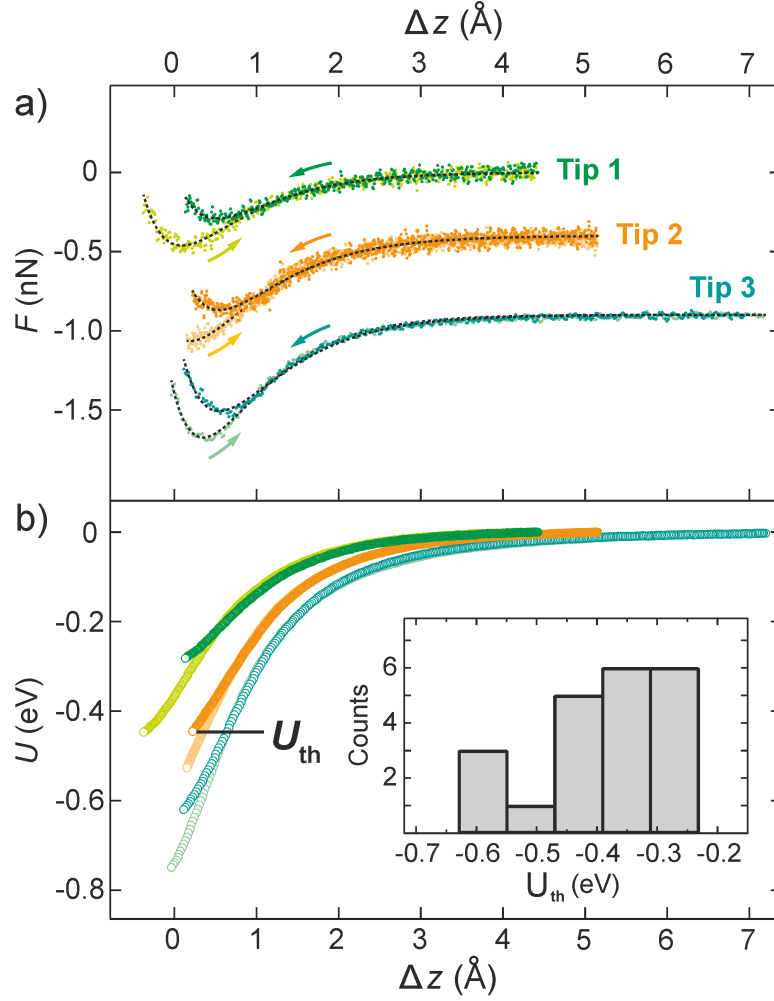


Figure 5.3:  $F(\Delta z)$  and  $U(\Delta z)$  tautomerization spectra of porphycene on Cu(110). a) Force  $F(\Delta z)$  spectra of the  $\Delta f(\Delta z)$  spectra shown in figure 5.2 and two further tips calculated by the Sader Jarvis method [86]. The data is fitted by the Morse potential model  $U(z) = -E_d [2 \exp^{-\kappa(z-z_e)} - \exp^{-2\kappa(z-z_e)}]$  with  $E_d$  the bond energy,  $\kappa$  the decay constant, and  $z_e$  the equilibrium distance. The tip height  $\Delta z$  is given with respect to  $z_e$  of the approach curves. b) Energy  $U(\Delta z)$  spectra of the tautomerization. The inset shows a histogram of the threshold energies  $U_{th}$ . Measurement parameters: tip 1:  $a = 100 \text{ pm}$ ,  $f_0 = 22653 \text{ Hz}$ ,  $Q = 18274$ ; tip 2:  $a = 100 \text{ pm}$ ,  $f_0 = 22645 \text{ Hz}$ ,  $Q = 33855$ ; tip 3:  $a = 100 \text{ pm}$ ,  $f_0 = 22646 \text{ Hz}$ ,  $Q = 39143$ .

### 5.2.1 Reproducibility of the tautomerization spectra

The tautomerization spectra are highly reproducible for the same tip conditions. Figure 5.4 shows six tautomerization spectra successively measured under the same tip condition over the same molecule. The tip position is indicated on

the STM image in the inset of figure 5.4 by a white star and corresponds to the position of the force spectra in figure 5.2. To ensure a stable spectroscopy position for multiple measurements, a grid over the STM was used (see blue grid in the inset of figure 5.4). In the six spectra, the tautomerization is induced in a frequency shift area of  $3.6\text{ Hz}$  within a tip-sample distance area of  $0.08\text{ \AA}$  with respect to the STM set point of  $V_{bias} = 100\text{ mV}$  and  $I_t = 10\text{ pA}$  above the bare Cu(110) surface. Note that due to the different tip condition for the spectra in figure 5.2, the observed frequency shift at the tautomerization differs.

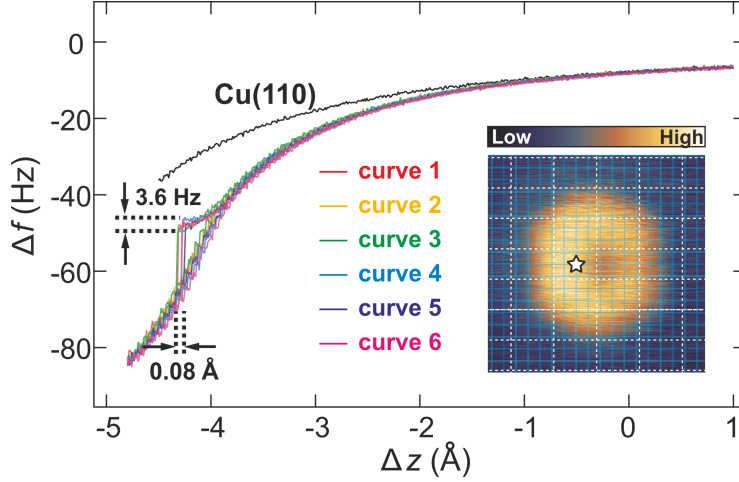


Figure 5.4: Reproducibility of the tautomerization with the same tip. Six successively measured frequency shift  $\Delta f$  spectra of the tautomerization. The tautomerization is induced in a tip height  $\Delta z$  area of  $0.08\text{ \AA}$  and  $\Delta f$  area of  $3.6\text{ Hz}$ . The inset shows an STM image with the position of the spectra. The blue grid was used to ensure a stable spectroscopy position and the white grid indicates the position of the Cu surface atoms. The tip height  $\Delta z$  is given with respect to the STM set point of  $V_{bias} = 100\text{ mV}$  and  $I_t = 10\text{ pA}$  over Cu(110). Measurement parameters:  $a = 100\text{ pm}$ ,  $f_0 = 23213\text{ Hz}$ ,  $Q = 51714$  (tip 4).

### 5.2.2 Influence of small bias voltage and tunneling current on the tautomerization

The force-induced tautomerization is investigated at zero bias voltage to prevent the possibility of an inelastic tunneling current induced tautomerization. But in an experimental set up, the bias voltage cannot be exactly zero due to the finite resolution of the instrument. In our system we use the digital-to-analog converter (DACs) of the Nanonis electronics, which has a 16-bit resolution. This leads to a minimal output resolution of around  $30\text{ }\mu\text{V}$  at an output range of  $\pm 1\text{ V}$ .

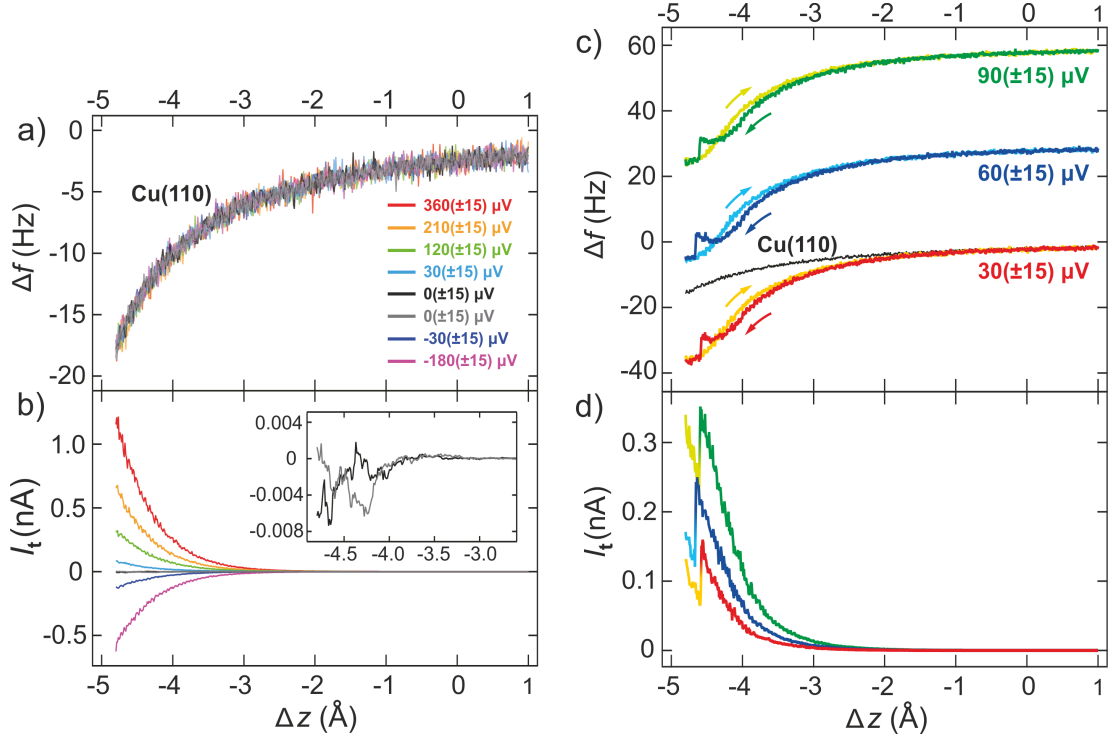


Figure 5.5: Influence of small bias voltage and current on  $\Delta f$  spectra and the tautomerization. a) Eight frequency shift  $\Delta f$  spectra with small applied bias voltages and their b) corresponding current  $I_t$  channels. The inset shows a zoom into the current channel at a bias voltage  $V_{bias} = 0 \mu V$  (same axis units). c) Three  $\Delta f$  spectra with small applied bias voltages and their d) corresponding current channel. The tip height  $\Delta z$  is given with respect to the STM set point of  $V_{bias} = 100 mV$  and  $I_t = 10 pA$  over Cu(110). Measurement parameters: a,b)  $a = 100 pm$ ,  $f_0 = 23234 Hz$ ,  $Q = 20315$ ; c,d)  $a = 100 pm$ ,  $f_0 = 23213 Hz$ ,  $Q = 51714$  (tip 4).

Therefore, even with a bias voltage experimentally set to zero a small flow of tunneling current cannot be excluded, as shown by the random fluctuations in the current signal in the inset of figure 5.5b. In figure 5.5a  $\Delta f$  spectra of Cu(110) with different applied bias voltages in the region of  $-180 \mu V$  to  $330 \mu V$  are shown. Even though the corresponding current channels (see figure 5.5b) exhibit tunneling currents of up to  $nA$  the  $\Delta f$  signal does not show any influence on this, we can therefore exclude a crosstalk in this bias voltage regime. Additionally, we investigated the force-induced tautomerization process with small bias voltages of  $30 \mu V$ ,  $60 \mu V$ , and  $90 \mu V$  (see figure 5.5c,d) and no influence could be detected. Therefore, a small flow of tunneling current is negligible for the  $\Delta f$  spectroscopy and the tautomerization.

### 5.2.3 Effect of long-range electrostatic force on the tautomerization

The contact potential difference (CPD) of a tip causes an electrostatic force gradient in the tip-sample junction; these long-range electrostatic forces could influence the tautomerization. Accordingly, we investigated the tautomerization with tips with substantially different CPD values, as shown in figure 5.6a and 5.6b. The tips were changed by application of bias voltage pulses with up to  $\pm 10$  V and by dipping the tip into the Cu(110) surface. The CPD value was determined by a

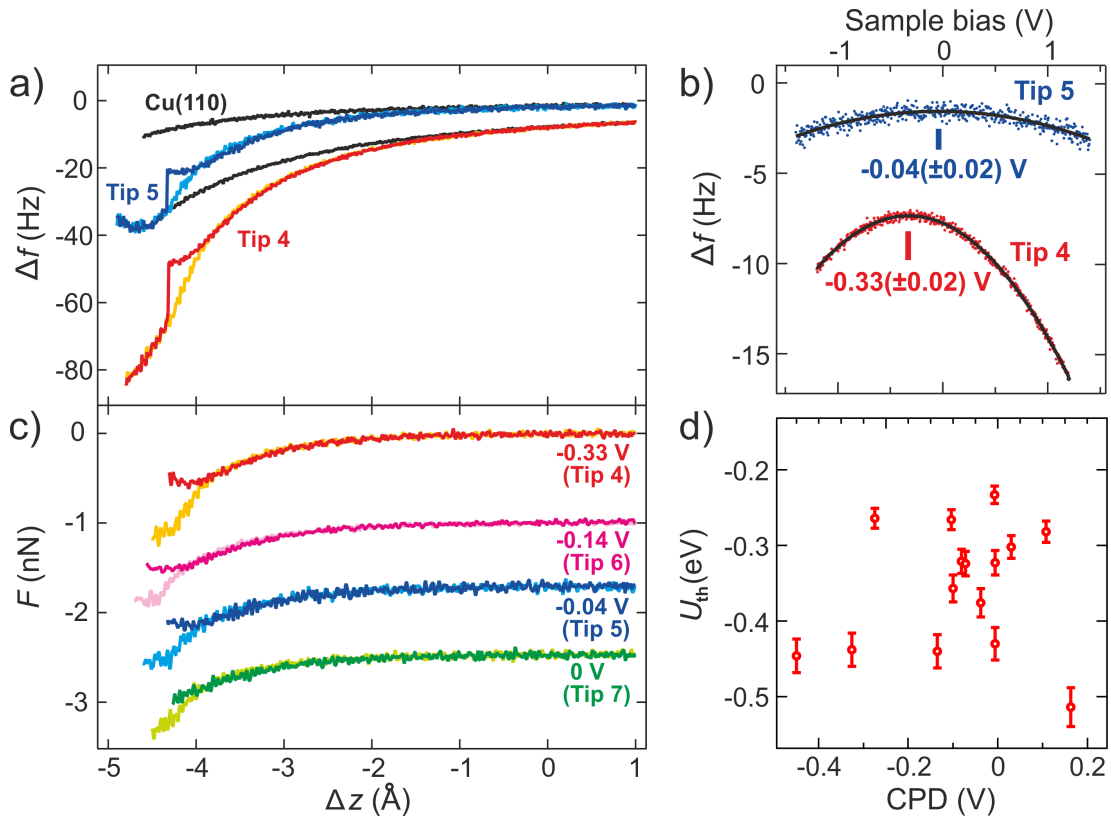


Figure 5.6: Effect of long-range electrostatic forces on the tautomerization. a) Frequency shift  $\Delta f$  spectra of porphycene measured with two different tips (no backward subtraction) and the corresponding Cu(110) spectra. b) Contact potential difference (CPD) spectra of the two tips in a). c) Force  $F$  spectra of the tautomerization (backward subtraction) of four different tips and their CPD values. d) Threshold energy  $U_{th}$  in dependence of the CPD value. The tip height  $\Delta z$  is given with respect to the STM set point of  $V_{bias} = 100$  mV and  $I_t = 10$  pA over Cu(110). Measurement parameters: tip 4:  $a = 100$  pm,  $f_0 = 23213$  Hz,  $Q = 51714$ ; tip 5:  $a = 100$  pm,  $f_0 = 23234$  Hz,  $Q = 20315$ ; tip 6:  $a = 100$  pm,  $f_0 = 23215$  Hz,  $Q = 49610$ ; tip 7:  $a = 100$  pm,  $f_0 = 23224$  Hz,  $Q = 34051$ .

bias voltage dependent measurement of  $\Delta f$  at a STM set point of  $V_{bias} = 100\text{ mV}$  and  $I_t = 10\text{ pA}$  over Cu(110), as shown in figure 5.6b. The tautomerization spectra of two tips with a CPD of  $-0.04\text{ V}$  (blue) and  $-0.33\text{ V}$  (red and orange) are shown in figure 5.6a. The tautomerization could be induced with both tips. Figure 5.6c shows the backward subtracted forces of these two and two additional tips with CPD values of  $-0.14\text{ V}$  and  $0\text{ V}$ ; no substantial differences can be observed in the main features of the force spectra. As discussed previously, the different tips show different interaction strength, but the threshold energies for inducing the tautomerization (and the threshold forces of  $\Delta f$  and  $F$ ) do not exhibit any dependence on the CPD value, as shown in figure 5.6d.

### 5.3 Force map of porphycene

Tip-molecule interactions depend strongly on the lateral position over a molecule [142] and  $\Delta f(\Delta z)$  spectra over different positions of the porphycene molecule showed that the tautomerization could not be induced everywhere over the molecule. To characterize the tip-molecule interactions and the tautomerization over the whole porphycene, we measured a three-dimensional force map out of individual  $\Delta f(\Delta z)$  spectra over the porphycene, shown in figure 5.7. Analog to the procedure for the  $\Delta f(\Delta z)$  spectra in figure 5.2, the tip height was adjusted by an STM set point of  $V_{bias} = 100\text{ mV}$  and  $I_t = 10\text{ pA}$  over the bare Cu(110) surface and the  $\Delta f(\Delta z)$  spectra were background subtracted before the  $F(\Delta z)$  spectra were calculated by the Sader Jarvis method [86]. STM images between the  $\Delta f(\Delta z)$  spectra were used to identify the tautomerization. Cu(110)- $\Delta f(\Delta z)$  spectra before, during, and after the porphycene- $\Delta f(\Delta z)$  spectra for the force map verified the stable tip conditions. To exclude influences of an unsymmetrical tip on the map data, the porphycene molecule was switched back to the original orientation after a successful tautomerization before the  $\Delta f(\Delta z)$  spectra were continued. The procedure of the measurement and analysis to adjust the position of the individual  $\Delta f(\Delta z)$  spectra and the whole force map to the porphycene molecule is described in the next subsection 5.3.1.

The three-dimensional force map (see figure 5.7) shows a very high spatial resolution, demonstrating the appropriateness of the AFM to study forces with an atomic spatial resolution. In particular, the force line spectrum in figure 5.7c along the symmetry axis of the porphycene molecule has a lateral spatial resolution of sub-Ångström, which exceeds the resolution obtained with STM imaging (see figure 5.1a) for this system. On the three-dimensional porphycene force map,

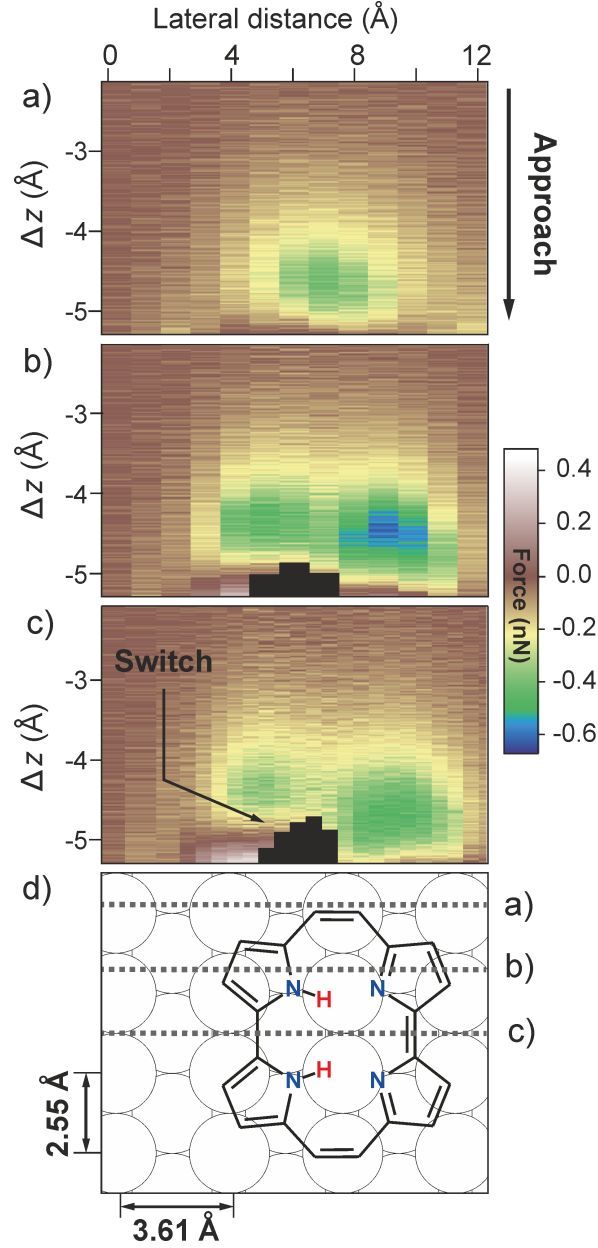


Figure 5.7: Force map of the porphycene. a-c) Force line spectra over the porphycene corresponding to the positions indicated in d). The line spectra were analyzed out of individual backward subtracted  $\Delta f(\Delta z)$  approach spectra by the Sader Jarvis method [86]. The black markers in b) and c) indicate the region after tautomerization of the porphycene molecule. The tip height  $\Delta z$  is given with respect to the STM set point of  $V_{bias} = 100 \text{ mV}$  and  $I_t = 10 \text{ pA}$  over Cu(110). d) DFT calculated structure model and positions of the force line spectra in a-c). Measurement parameters:  $a = 100 \text{ pm}$ ,  $f_0 = 22653 \text{ Hz}$ ,  $Q = 18274$  (tip 1).



two attractive force minimums can be identified: one over the NH and one over the N side of the inner cavity of the porphycene molecule. The strongest interaction forces can be observed above the bare N sides. The tautomerization is shown by the black markers in figure 5.7b and 5.7c. All tautomerization appeared as a single sudden jump at the tip height, indicated by the beginning of the black marked region, and no instable behavior or backward tautomerization on a  $F(\Delta z)$  spectrum of the three-dimensional force map was observed. The absence of any tip height ( $\Delta z$ ) area or position area over the porphycene molecule with an unstable reversible tautomerization indicates a clear energy difference between the initial and final tautomeric state in presence of the tip at these positions over the molecule. The tautomerization can be successfully induced in the area over the NH sides of the inner cavity of the porphycene molecule. The tautomerization transfers the H atoms intra molecular from the NH sides under the tip towards the other side and leaves behind the bare N sides with stronger tip-molecule interactions under the tip after the tautomerization. The shortest tip approach which could induce the tautomerization can be found on the molecular symmetry axis at around the center of the area, which could successfully induce the tautomerization. This represents the position (see figure 5.1a) of the  $\Delta f(\Delta z)$  spectra shown in figure 5.2 and indicates this as good reference position for further investigations of the mechanism of the force-induced tautomerization by a comparison to theoretical simulated data.

### 5.3.1 Position adjustment of the force map

To adjust the position of the force map with respect to the molecule and underlaying surface represents an experimental challenge. During the three-dimensional force map measurements, a grid over the STM image of the porphycene molecule was used to determine the position of the individual  $\Delta f(\Delta z)$  spectra with respect to the porphycene molecule. Additionally, a manual drift correction according to the STM images measured between the individual  $\Delta f(\Delta z)$  spectra ensured a high positional precision.

To adjust the STM image with the grid of individual  $\Delta f(\Delta z)$  spectra with respect to the chemical structure and underlaying Cu(110) surface, the known DFT calculation optimized molecular adsorption position and the corresponding simulated STM images give a good basis. As the frequency shift spectra show very high position dependence and the porphycene molecule switches between two mirror symmetric states, additionally, a comparison of corresponding spectra was used for the lateral position alignment of the force map. Assuming a

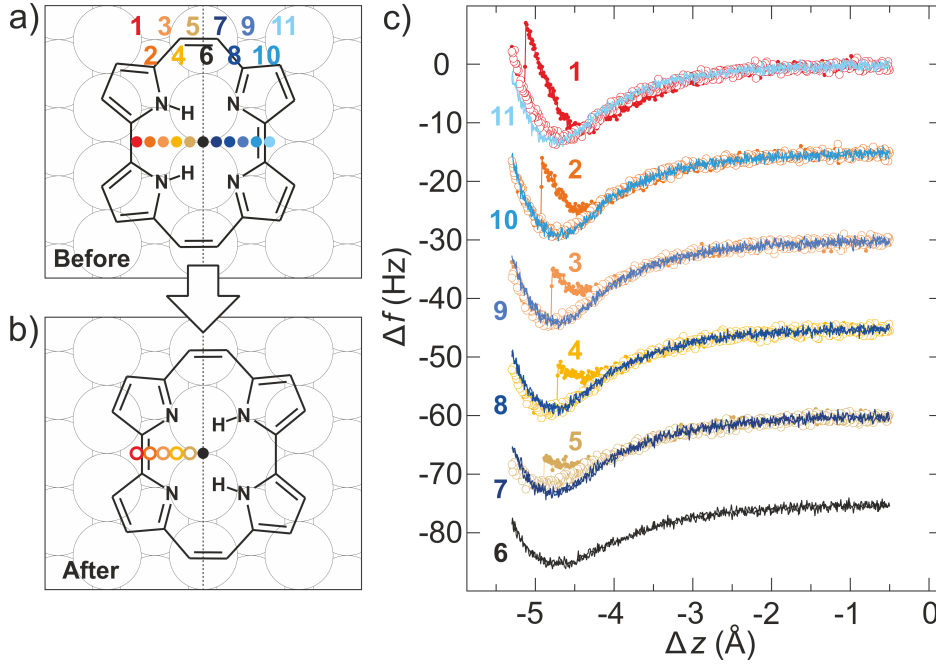


Figure 5.8: Position adjustment of the force map. a, b) Schematic sketch of DFT calculated optimized structure of the porphycene molecule on Cu(110) with the position of the spectra before (a) and after the force-induced tautomerization (b). Note that porphycene molecule changes its adsorption position during the *cis* to *cis* tautomerization by  $0.4 \text{ \AA}$  [25]. c) Backward subtracted approach and retraction frequency shift  $\Delta f(\Delta z)$  spectra. The tautomerization is (exclusively) induced over the NH side of the porphycene, red to yellow filled circles in a), leading to spectra over the N side for the retraction, red to yellow unfilled circles in b), which are comparable to the spectra measured directly over the N sides of the porphycene, blue filled circles in a). The best fitting pairs (1&11; 2&10; 3&9; 4&8; 5&7; 6) are shown in c) with the same  $\Delta f$  shift (0; -15; -30; -45; -60; -75 Hz). The tip height  $\Delta z$  represents the relative tip displacement with respect to an STM set point of  $V_s = 100 \text{ mV}$  and  $I_t = 1 \text{ nA}$ . Measurement parameters:  $A_{ocs} = 1 \text{ \AA}$ ,  $f_0 = 22646 \text{ Hz}$ ,  $Q = 39143$  (tip 1).

symmetrical tip, each spectrum measured over the NH side of the porphycene (see red to yellow filled circles figure 5.8a) is a spectrum over the N side of the porphycene after the tautomerization (see red to yellow unfilled circles figure 5.8b) and has a corresponding spectrum measured directly over the N side of the porphycene, (see blue filled circles figure 5.8a). Therefore, the  $\Delta f(\Delta z)$  spectra after the tautomerization can be compared to the spectra over the N sides of the porphycene to identify the best fitting pairs, which are shown in figure 5.8c. The small deviations are expected to result from small uncertainties in the chosen

tip position for the  $\Delta f(\Delta z)$  spectra and possible asymmetrical geometries at the tip apex. Nevertheless, this procedure should give an accuracy of  $\pm 0.4 \text{ \AA}$  in the lateral position adjustment of the force map.

## 5.4 Potential curves in position dependence

To identify the energies required and gained by the tautomerization in dependence of the position above the NH sides, three tautomerization spectra are shown in figure 5.9. The energy spectra are measured at the symmetry axis of the porphycene molecule and are exemplary chosen to show the energetic behavior for the tautomerization at the outer edge of the molecule (see (i) in figure 5.9a), the center of the area where the tautomerization can be induced successfully (see (ii) in figure 5.9a), and close to the center of the molecule (see (iii) in figure 5.9a), as indicated in the sketch of the porphycene molecule in the inset of figure 5.9a. As discussed already in connection with the three-dimensional force map data (see section 5.3), the tautomerization is induced after the shortest approach distance at the green centrally located tautomerization spectrum (see (ii) in figure 5.9a). But next to the tip height at the tautomerization, the relation of the approach and retraction spectra before and after the tautomerization shows to be very position dependent, which is of interest as it allows conclusions on the preferred tautomeric state. This relation is well accessible by analyzing the difference of the approach and retraction spectra  $\Delta U = U_{\text{initial}} - U_{\text{final}}$  which defines the energy that is gained due to the tautomerization. These  $\Delta U(\Delta z)$  energy spectra are shown in figure 5.9b and identify distinct differences in the evolution of the energy gain with the tip-sample distance dependent on the position above the NH side of the porphycene molecule. At the outer edge of the molecule (see (i) in figure 5.9b), the energy shows a crossover behavior with a favorable energy for the initial state at large tip-sample distances and a favorable final state at close tip-sample distances. This behavior vanishes towards the inner molecular side (see (iii) in figure 5.9a), where the energy gain shows monotonous increase. At the tip-sample distance of the tautomerization, the final state is favorable and the system gains energy independent of the tip position over the molecule. That the preference of a tautomeric state can be influenced and even the favorable state changed depending on the distance of an "atom of influence" in the atomic scale surrounding of the molecule has also been observed by the tuning of the tautomerization rate of the STM induced tautomerization with an adatom next to the molecule (see section 2.3.3) [25]. Depending on the adatom molecule

distance, the porphycene first preferred the state with the H atoms at the side of the adatom and changed this favorable tautomeric state at very close adatom distance. The position dependent energy spectra support these previous results and demonstrate that the favorable tautomeric state depends next to the "atom of influence" molecule distance also strongly on the position of approach to the molecule.

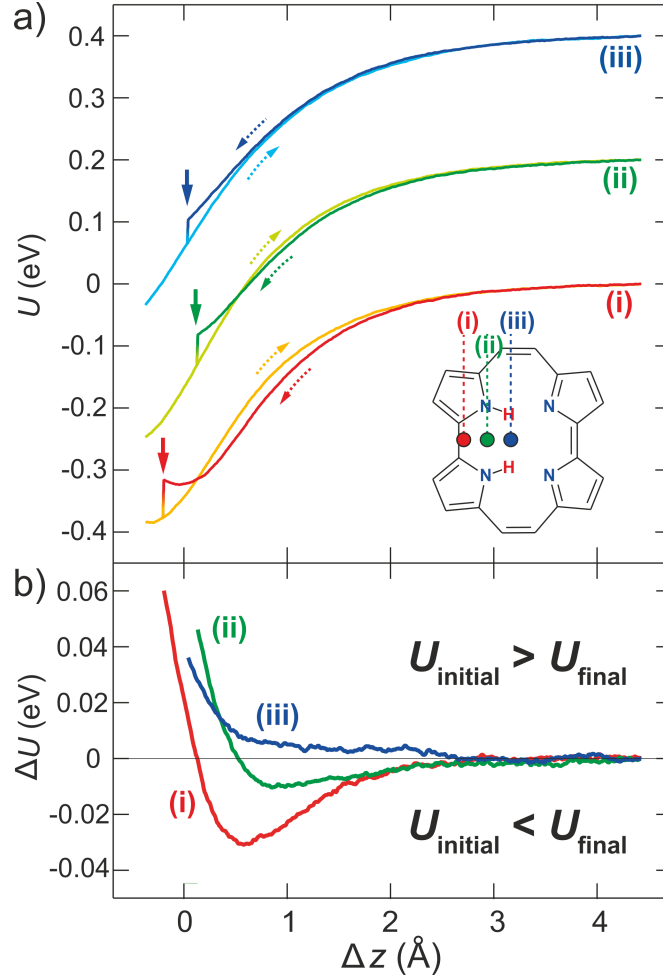


Figure 5.9: Potential curves of the tautomerization in position dependence. a) Tautomerization energy  $U$  spectra at three positions above the porphycene as indicated in the inset (backward subtracted). The tip height  $\Delta z$  is given with respect to  $z_e$  of the Morse potential model fit at the position (ii) (green) (due to a higher fitting accuracy the fit was proceed with the force data shown in figure 5.3). For clarity the spectra of position (ii) and (iii) are displaced by  $0.2\text{ eV}$  and  $0.4\text{ eV}$ , respectively. b) Energy gain  $\Delta U = U_{\text{initial}} - U_{\text{final}}$  corresponding to the tautomerization spectra in b). Measurement parameters:  $a = 100\text{ pm}$ ,  $f_0 = 22653\text{ Hz}$ ,  $Q = 18274$  (tip 1).

## 5.5 Xe terminated tip

A very interesting question is the importance of the chemical properties of the tip for the force-induced tautomerization. Distinct influence of the chemical tip properties was for example predicted by DFT calculations for Si atom hopping on Si(111) [143]. Hence, we functionalized the AFM tip by vertical manipulation with a single Xe atom (see sketch in figure 5.10a) [144]. The Xe tip termination did not significantly change the STM image contrast but enhanced it slightly in comparison to the Cu tip (see STM images in figure 5.10b and c).

To characterize the importance of the chemical properties of the tip apex on the tautomerization, we investigated the interaction forces between the Xe tip and the porphycene molecule. In contrast to the measurement with a Cu tip, a minimum in the frequency shift spectrum over the Cu(110) surface can be measured. As shown in figure 5.10b, the spectrum over the porphycene molecule was taken at the same position as the one where the Cu tip induced the tautomerization. With the Xe tip the frequency spectrum shows an attractive minimum and enters into the repulsive regime at closer tip-sample distances. For further approach of the tip, the interaction becomes attractive again, suggesting a sideways relaxation of the Xe atom at the tip apex. The backward spectrum follows the same trajectory as the forward one and the STM image taken after the spectra (see figure 5.10c) identifies that no tautomerization was induced by the Xe tip. Figure 5.10e and the inset of figure 5.10d and 5.10e show the background subtracted energy, frequency shift and force spectrum in the area before the Xe atom relaxes at the tip apex. The interaction energy between the Xe tip and the porphycene is much smaller than the one with the Cu tip, suggesting that the Xe tip can not overcome the threshold energy to induce the tautomerization. The fit of the force spectrum with the Morse potential model does not reveal the experimental data as well as the spectra taken with a Cu tip, which may attribute to a slight relaxation of the physisorbed Xe atom on the Cu tip due to the expected weak bonding strength [145] between Xe and tip already in this regime.

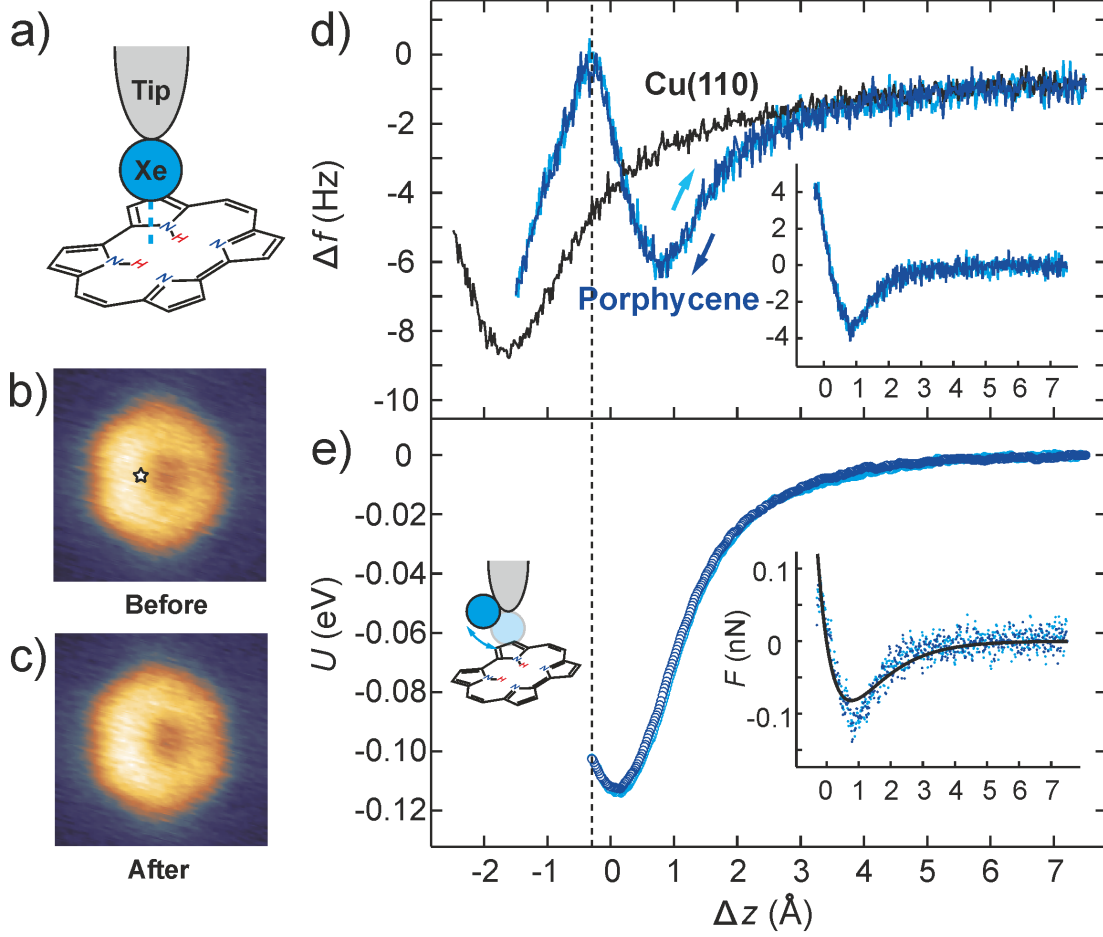


Figure 5.10: Force spectroscopy of porphycene with a Xe terminated tip. a) Schematic sketch of the Xe terminated tip over the porphycene molecule. b) STM image before and c) after the spectrum over the porphycene. The tautomerization was not induced by the Xe terminated tip. d) Frequency shift  $\Delta f$  spectrum of the porphycene and the Cu(110) surface with the Xe terminated tip. The position of the tip over the molecule is indicated by a white star in b). The inset shows the backward subtracted porphycene spectrum in the area before the Xe tip relaxes, as indicated by the dashed line (same axis units). e) The background subtracted energy  $U$  spectrum and in the inset the corresponding force  $F$  spectrum (same x-axis unit). The force spectrum is fitted by the Morse potential model and the tip height is given with respect to  $z_e$ . Measurement parameters:  $a = 100 \text{ pm}$ ,  $f_0 = 22646 \text{ Hz}$ ,  $Q = 39143$ .

## 5.6 DFT calculations of porphycene

To get a closer insight into the mechanism of the force-induced tautomerization we modeled the surface-molecule-tip system with DFT (see figure 5.11a) and calculated the optimized structure, force curves, and the reaction pathway in collaboration with Thomas Frederiksen and Mats Persson. The DFT calculations of the geometries, interaction energies, MEPs, vibrational modes, and vibrational frequencies were calculated using periodic, plane-wave DFT of the Vienna ab-initio simulation program (VASP) [146]. Additionally the electron-ion core interactions were computed by the Projected Augmented Wave (PAW) method [147] and the exchange-correlation by the van der Waals density functional optB86B [148–151]. The plane-wave cut off was set to 400 eV. The Cu(110) surface was implemented by a super cell containing four layers of  $4 \times 6$  Cu(110) unit cell and 20 Å vacuum region. The Cu tip was modeled by a pyramid of five Cu atoms and for the Xe tip a Xe atom was adsorbed on its tip apex. A  $2 \times 2 \times 1$  grid was used in the k-point sampling. The bottom two Cu layers were kept fixed at the lattice constant of 3.6 Å at the relaxation of the structures. The rest of the structure was relaxed until all forces were less than 0.01 eV/Å.

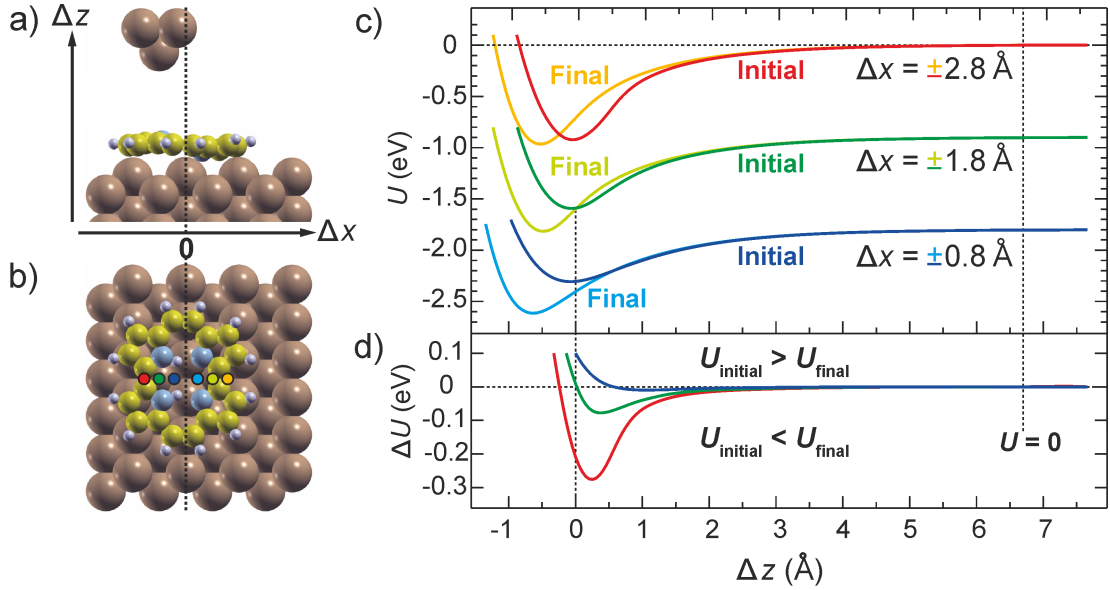


Figure 5.11: DFT calculation of the energy spectra. a, b) Structure model of the DFT optimized structure of porphycene on Cu(110). c) DFT calculated background subtracted interaction energies  $U$  at three positions over the NH (initial) and the N (final) sides of the porphycene molecule as indicated in b) and d) their corresponding energy gain  $\Delta U = U_{\text{initial}} - U_{\text{final}}$  spectra. The initial and final spectra represent the states before and after the tautomerization.

The DFT calculated optimized structure of porphycene on Cu(110) is shown in figure 5.11a and b. The bare N atoms interact with the underlying Cu atoms and distort the molecule from its planar gas phase form by  $0.75 \text{ \AA}$ . Additionally the interaction shifts the molecular axis with respect to the underlying closed packed  $[1\bar{1}0]$  Cu row by  $0.2 \text{ \AA}$  along the Cu  $[001]$  high symmetry direction.

As comparison to the experimentally determined position dependent interaction energies and energy gains of the tautomerization, we performed DFT calculations of the tip porphycene system with approaching the tip at six different positions over the porphycene molecule. To represent the experimental positions in figure 5.9a, the interaction energies were calculated with a tip displacement of  $\Delta x = \pm 2.8 \text{ \AA}$ ,  $\Delta x = \pm 1.8 \text{ \AA}$ , and  $\Delta x = \pm 0.8 \text{ \AA}$  of the molecular axis along the porphycene mirror axis, as indicated by the colored circles in figure 5.11b. In addition, the energy spectra were calculated for the tip approach over the bare Cu surface and subtracted from the Cu tip, porphycene, Cu surface calculated energies in order to obtain the background subtracted data shown in figure 5.11c. The associated energy gains at these three tautomerization positions are plotted in figure 5.11d. Furthermore, a force map along the porphycene mirror axis was calculated (see figure 5.12). The experimentally and theoretically determined interaction energies and forces agree quantitatively very well to each other, display the stronger forces over the N sides than over the NH sides and reveal the position dependent development of the energy gain before and after the tautomerization. Nevertheless, the calculated energies and forces exceed the experimentally de-

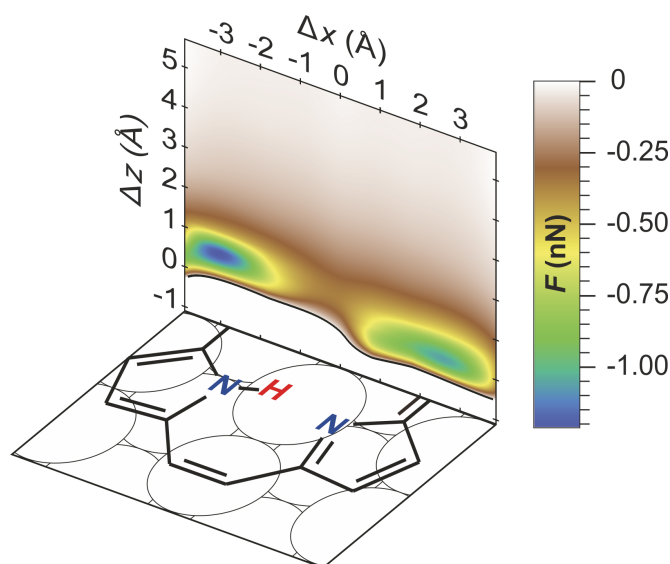


Figure 5.12: DFT calculation of the force map (only the  $F < 0$  regime is shown).



terminated ones. Next to the experimental error of around 10 – 20% due to the limited precision of the exact spring constant [152] also the tip model used in the DFT, a pyramid of five atoms, is an idealistic, low-coordinated and therefore rather reactive tip, which can lead to an overestimation of the tip interactions. Moreover, the force map shows strong minimums at the edges of the porphycene, suggesting an influence of the rather sharp and reactive tip model.

## 5.7 Mechanism of the force-induced tautomerization

### 5.7.1 Importance of the NH bond

In the gas phase the porphycene has a very low tautomerization barrier of around 70 *meV* [47], which is overcome via quantum tunneling and leads to rapid tautomerization [27]. It was identified that the tautomerization rate is essentially influenced by the hydrogen bonding strength and geometry in the porphycene cavity [50]. Considering the porphycene on Cu(110), the slight distortion from the planar form in gas phase distorts the geometry of the inner cavity and can lead to an increasing tautomerization barrier, which can be associated to weaker H bonds in the distorted cavity. The interaction with the approaching tip could lead to additional changes of the NH bonding geometry in the porphycene cavity.

It can be expected that the NH stretching mode is very sensitive to the hydrogen bonding strength and the geometry in the inner cavity. As reported, the NH stretching mode at around 380 *meV* can be detected by  $dI/dV$  spectroscopy [24] (see section 2.3.1), as shown in figure 5.13a. Therefore, we determined the NH stretching mode in dependence of the tip-sample distance as shown in figure 5.13b. The NH stretching mode shifts to lower energies at close tip-sample distances, which can be associated with a decreasing strength of the NH bond.

The DFT calculated NH stretching modes in tip distance dependence are shown in figure 5.14. With the tip positioned over the NH side (black dots), the stretching mode shifts to lower energies at close tip-sample distances. In contrast to this, the mode shifts to higher energies when the tip is placed over the bare N sides, indicating the importance of the tip positioning over the porphycene. The influence of the tip on the geometry of the inner cavity and the hydrogen bond strength can also be indicated by the NH bond length. A DFT calculated map of the NH bond length in dependence of the tip position is shown in figure 5.15. The map shows a maximum NH bond length for a tip located around the NH sides,

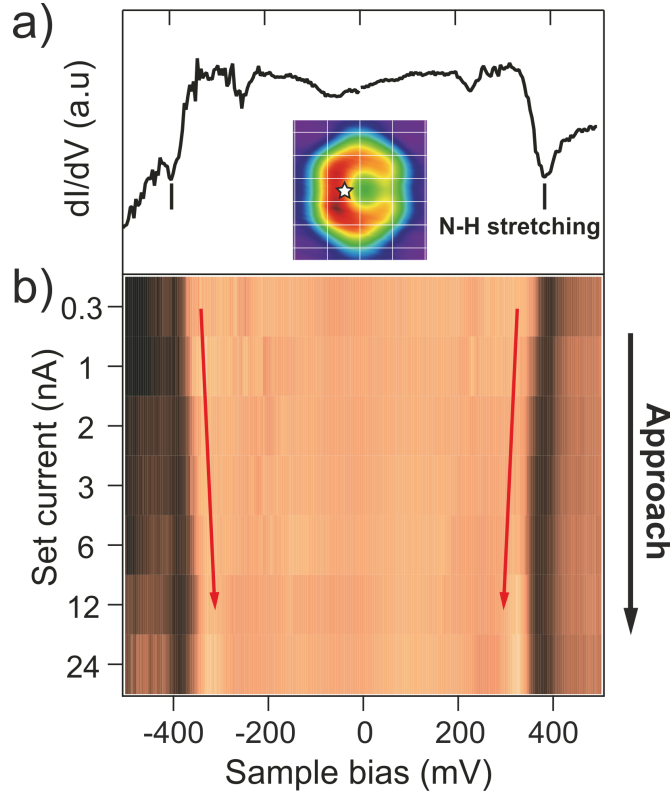


Figure 5.13:  $dI/dV$  of the NH stretching mode in tip-sample distance dependence. a)  $dI/dV$  spectrum of the NH stretching mode of porphycene ( $I = 300 \text{ pA}$ ;  $V = 100 \text{ meV}$ ). The inset shows an STM image with a star indicating the tip position. b) NH stretching mode  $dI/dV$  spectrum in tip-sample distance dependence. The tip height is given by the indicated STM current and a bias voltage of  $V = 100 \text{ meV}$  over the porphycene. Note that this data was measured with a pure STM setup of the system (no  $q^+$ -sensor) to increase the signal-to-noise ratio. Due to the absence of the oscillation amplitude, the tip height differs from the STM set point in the AFM setup. In the STM setup the tip is closer to the surface by approximately the oscillation amplitude.

which corresponds well to the tautomerization positions determined in experiment. Interestingly, the NH bond already extends in the attractive force regime (see the attractive-repulsive interaction force contour indicated by the black line in the map in figure 5.15), which reflects the experimental data very well. In summary, the tip-porphycene interactions influence the inner cavity geometry. At the tip positions of tautomerization, the red-shift of the NH stretching mode and increase of the NH bond length indicate stronger H bonds, which reduce the tautomerization barrier, that can then be overcome for example by quantum tunneling [153, 154].

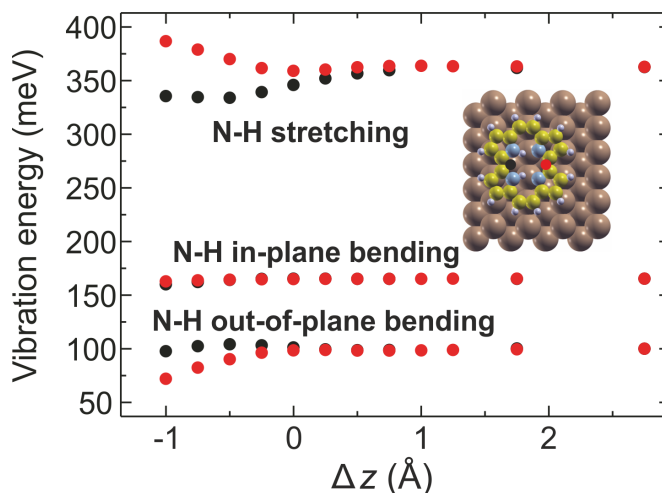


Figure 5.14: DFT calculation of NH modes in presence of the tip. DFT calculation of the NH stretching and NH in- and out-of-plane bending modes in dependence of the tip-sample distance at two positions over the porphycene molecule as indicated in the inset.

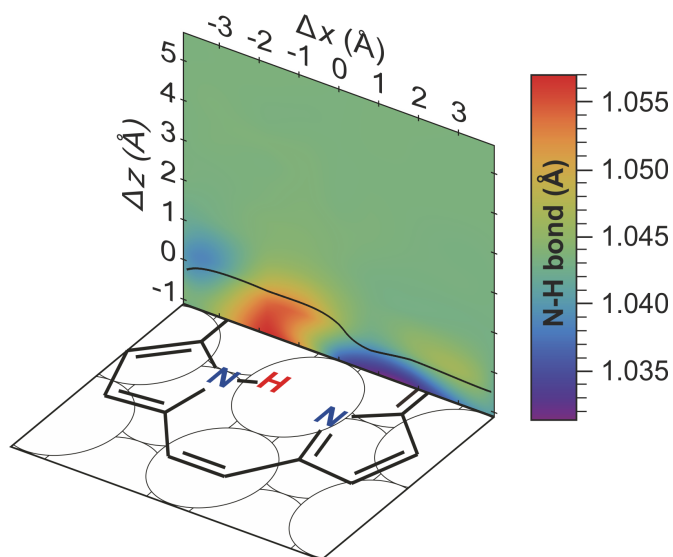


Figure 5.15: NH bond length map in dependence of the tip position. The contour between attractive and repulsive tip-sample forces  $F(z_{line}) = 0$  is indicated by a black line.

### 5.7.2 Minimum energy path (MEP)

Minimum energy paths (MEPs) of the tautomerization were calculated by the nudge elastic band (NEB) method [155, 156]. For the NEB method the initial and final state of the reaction must be known and an initial guess of an inter-

mediate state is interpolated to give a reaction path. The images along the path are minimized to give the MEP. The path length corresponds to the Euclidean

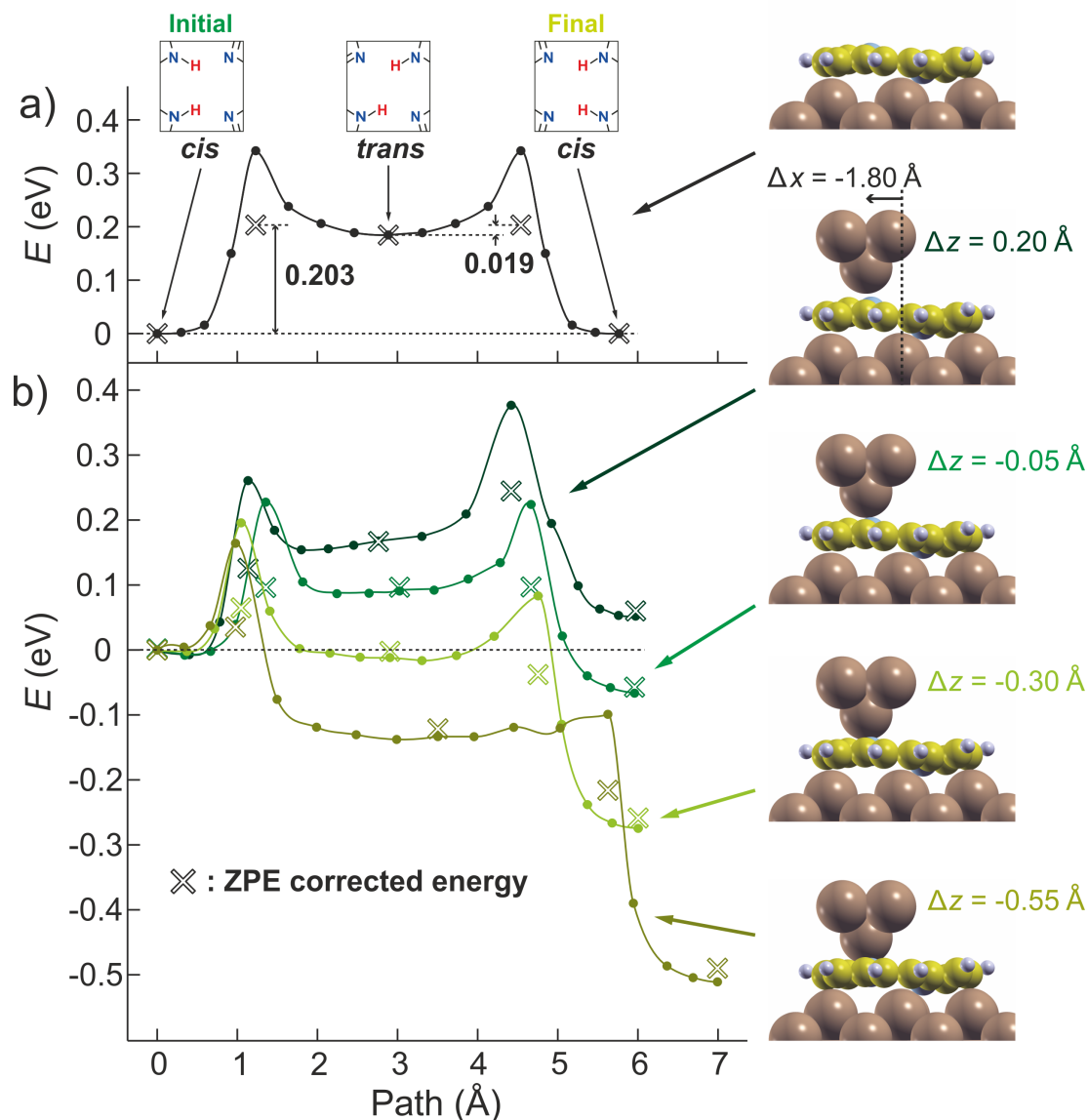


Figure 5.16: Minimum energy paths (MEPs) of the stepwise *cis* to *cis* tautomerization. a) MEP for the stepwise tautomerization via an intermediate *trans* state in absence of the tip and b) in presence of the tip over the NH side at different tip-sample distances as indicated by the geometry of the model. The crosses indicate the energy of the initial, final, barrier, and intermediate states including a zero-point energy (ZPE) correction calculated by considering the vibrational energy of the two inner H atoms.

distance between the images along the reaction path in the configuration space. In porphycene two tautomerization pathways are possible for the intermolecular transfer of the two H atoms: a stepwise tautomerization over one of the intermediate *trans* states or a concerted tautomerization where both H atom transfer at the same time and the molecule maintains its axis symmetry during the path. For these two reactions, the minimum energy pathways in absence of the tip are shown in figure 5.16a and 5.17. For the stepwise process, one obtains a symmetric MEP over one of the intermediate *trans* states with a *cis* to *trans* energy barrier of 342 meV and a *trans* to *cis* barrier of 168 meV. For comparison to the experimental data, the influence of the zero point energy (ZPE) of the two inner H atoms should be considered. The ZPE corrected energies  $U_c$  are defined as  $U_c = U(x) + U_{ZPE}(x) - U_{ZPE}(cis_i)$  with  $U(x)$  and  $U_{ZPE}(x)$  the potential and the zero-point energy at the state x and  $U_{ZPE}(cis_i)$  the zero-point energy at the initial *cis* state  $cis_i$ . The ZPEs were modeled by the vibration energies of the two inner H atoms, where only these were allowed to move. One of the vibration modes was observed to be unstable at the barrier configuration, indicating the transition state nature of this configuration. Including the ZPE, the

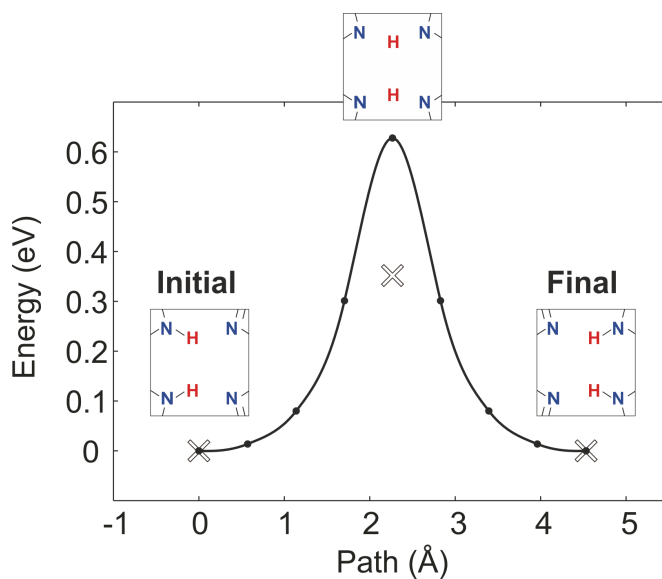


Figure 5.17: MEP for the concerted tautomerization in absence of the tip. The MEPs are calculated with the nudge elastic band (NEB) method and the path length is determined by the Euclidean distance between the images in the configuration space. The crosses indicate the energy of the initial, final, barrier, and intermediate states, including a zero-point energy (ZPE) correction calculated by considering the vibrational energy of the two inner H atoms.

barriers reduce to  $203\text{ meV}$  for the *cis* to *trans* state and  $19\text{ meV}$  for the *trans* to *cis* state. For the concerted pathway (see figure 5.17), the energy barrier is with  $628\text{ meV}$  and  $352\text{ meV}$  with ZPE correction much higher than the stepwise tautomerization, identifying this path as less favorable. Therefore, the energetically preferred stepwise pathway was used to calculate the potential landscape of the tautomerization under the influence of the interaction forces with the AFM tip. In figure 5.16b the MEP of the stepwise tautomerization is calculated in dependence of the approaching tip. The tip-sample interactions distort the MEP, depending on the tip height. At large tip-sample distances, the initial state is energetically favorable over the final state. This changes for smaller tip heights  $\Delta z < 0\text{ \AA}$  and the final state is favorite. At very close tip-sample distance of  $\Delta z = -0.55\text{ \AA}$ , the *cis* to *trans* barrier reduces to  $164\text{ meV}$  and the *trans* to *cis* barrier to  $34\text{ meV}$ . Including the ZPE correction, the *trans* to *cis* barrier vanishes completely and only the *cis* to *trans* barrier of  $35\text{ meV}$  remains, which can lead to the tautomerization via quantum tunneling [153,154].

## 5.8 DFT calculations with a Xe terminated tip

In figure 5.18 DFT calculations with a Xe terminated Cu tip are shown. For these calculations the tip model of a pyramid of five Cu atoms was extended by a Xe atom at its tip apex (see figure 5.18a) and the force and energy in tip height dependence are calculated, as shown in figure 5.18b. The interaction forces and energies are generally much weaker than the interactions calculated for the Cu tip, which reflects the experimental observations very well. Allowing the Xe atom to relax on the tip apex (see figure 5.18c), it does so at short tip-sample distances and the force spectroscopy shows a second minimum in the repulsive interaction regime close to  $z = 0$  (see figure 5.18d), standing in good agreement with the experiment. The DFT calculation results suggest that the molecule Xe tip interactions are too weak and the Xe atom is not stiff enough to induce the tautomerization of the porphycene molecule.

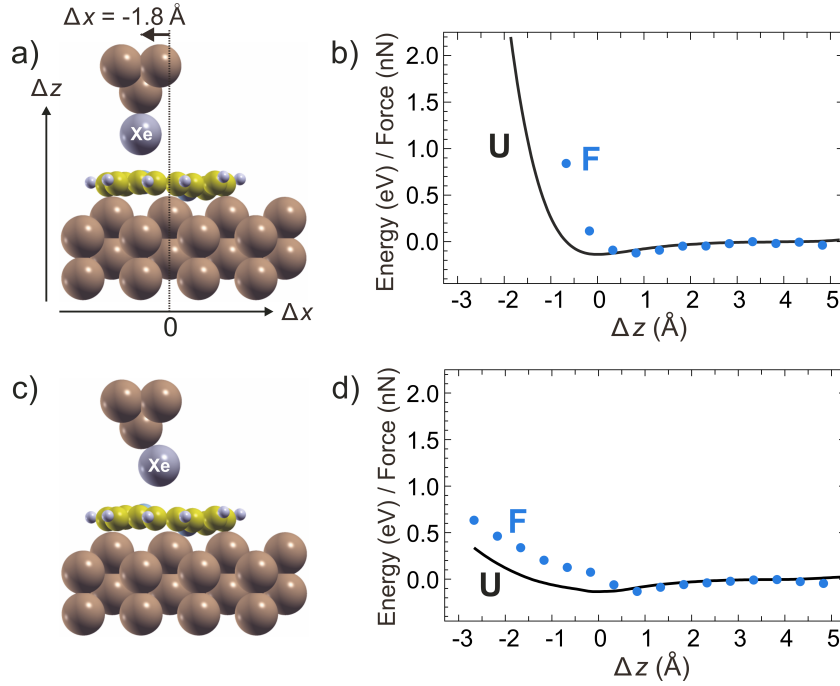


Figure 5.18: DFT calculations of spectroscopy with a Xe tip. a) Structural model of a frozen and c) relaxed Xe terminated Cu tip approaching to a porphycene molecule on Cu(110). b) Background subtracted interaction forces and energies between the frozen and d) relaxed Xe terminated Cu tip and the porphycene molecule for a lateral tip position of  $\Delta x = -1.8 \text{ \AA}$ . The background subtracted force  $F$  (blue markers) is derived from the background subtracted energy  $U$ . The tip height  $\Delta z$  is defined with respect to the energy minimum of  $U$  with a frozen Xe tip.

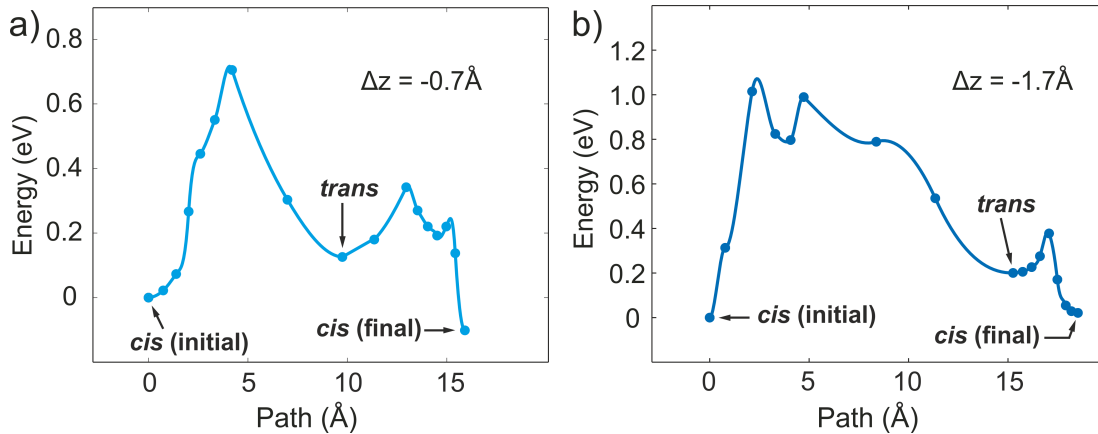


Figure 5.19: Minimum energy path for the tautomerization with a Xe tip. a) Calculated MEP for the stepwise *cis* to *cis* tautomerization via an intermediate *trans* state for a Xe terminated Cu tip at a tip height of  $\Delta z = -0.7\text{\AA}$  and b)  $\Delta z = -1.7\text{\AA}$ . The tip height is defined with respect to the potential minimum calculated with a frozen Xe tip and the lateral tip position of  $\Delta x = -1.8\text{\AA}$ . The MEPs are calculated with the nudge elastic band (NEB) method and the path length is determined by the Euclidean distance between the images in the configuration space.

Figure 5.19 shows the MEPs for the stepwise *cis* to *trans* to *cis* tautomerization with a Xe terminated tip. The tautomerization barrier is with  $0.72\text{ eV}$  and around  $1.07\text{ eV}$  for  $\Delta z = -0.7\text{\AA}$  (see figure 5.19a) and  $\Delta z = -1.7\text{\AA}$  (see figure 5.19b), respectively, much higher than for the Cu tip. The Xe atom is in the way of the reaction, which results in larger motions of the Xe atom and the atoms in the molecule in the reaction path. In contrast to the Cu tip, the reaction barrier is much higher in presence of a Xe tip than in absence of a tip, demonstrating the importance of the chemical properties of the tip to lower the tautomerization barrier via tip-molecule interactions and inducing the tautomerization.



## 5.9 Summary

We investigated the force-induced tautomerization of porphycene on Cu(110) by NC-AFM experiments and DFT calculations. On a Cu(110) surface the porphycene molecules are exclusively found in the *cis* tautomeric state and can be reversibly switched between the two *cis* states in absence of sufficient thermal or tunneling electron-induced energy at zero bias voltage and 5 K merely by interaction with an approaching Cu tip. Force spectroscopy with an approached and retracted AFM tip revealed the interaction forces between the Cu tip and the porphycene molecule and identified the tautomerization as instantaneous process, which is highly reproducible with the same tip conditions. The tautomerization occurred within a tip height area of 8 pm and a frequency shift area of 3.6 Hz (around 8% of the frequency shift at this tip height) for six spectra measured with the same tip conditions. For different tip conditions, the tautomerization threshold varies between 230 – 630 meV for 21 Cu tips. Three-dimensional force mapping of individual approach and retraction spectra over the porphycene molecule showed a high spatial sensitivity with a lateral resolution on the sub-atomic level, which exceeded the STM resolution of this system. The force map showed local interaction strength maxima over the NH sides of the inner cavity of the porphycene and the strongest interaction forces above the N sides. The tautomerization can be induced over the NH side of the inner cavity of the porphycene molecule, leading to stronger interaction forces and gained energy after the tautomerization with a tip over the bare N sides. DFT calculations of the approach and retraction force spectra and the force mapping show a very high quantitative agreement to the experimental results. Experimentally, a shifting of the NH stretching mode was found for an approaching tip at the position over the molecule where the tautomerization could be induced successfully, which was confirmed by DFT calculations. Furthermore, the calculated NH bond length showed to be higher for an approached tip at this position. The shifting of the NH stretching mode and the higher NH bond length indicate that the approaching tip lead to a changing of the inner cavity arrangement with stronger H bonding, which is known to lower the tautomerization barrier [50]. The NEB theory calculations revealed the evolution of the reaction barrier under the force of the approaching tip and identified a significant lowering of the tautomerization barrier and a stepwise *cis* to *trans* to *cis* tautomerization process. In the experiments, the tautomerization could not be induced by a Xe terminated tip, indicating the importance of the chemical properties of the tip apex. The DFT calculations with a Xe terminated tip showed a very high tautomerization barrier

in presence of the Xe tip, which even extended the barrier in absence of a tip and identified that the Xe atom bends at close tip-sample distances and is in the way of the reaction, confirming the importance of the chemical nature of the tip apex.

These results demonstrate that merely the approaching of a tip can lower the reaction barrier and induce the reaction process, which invokes a catalytic process. The absence of the reaction process for the Xe terminated tip displays the crucial importance of the tip reactivity and stability to reduce the reaction barrier. As the SPM tip termination with various atoms and molecules is a well-established method [59, 157–162] a systematic study of different tip terminations could give an insight into the mechanism of a catalytic reaction and provide a tool for controlling a reaction barrier at the atomic level. Additionally, the SPM technique provides the possibility to probe and manipulate the local environment of a molecule and the procedures of this study could be used to investigate the catalytic nature of e.g. step edges, defects or molecules on the a reaction process. Controlled force-induced reactions, as demonstrated in this study, could therefore give an insight into catalytic reaction mechanisms on surfaces.

# Chapter 6

## Summary and Outlook

This thesis described the study of tautomerization of single porphycene molecules on Cu surfaces using low-temperature SPM and demonstrated that the process could be induced by different external stimuli, i.e., heat, electrons, and force. The electron- and heat-induced tautomerization and the nonlocal hot carrier-induced tautomerization were studied on a Cu(111) surface with STM. The force-induced tautomerization was studied on Cu(110) with an AFM. The mechanism of the force-induced process was also investigated by DFT calculations and revealed that the tautomerization is triggered through the distortion of the potential landscape in the presence of the AFM tip.

Porphycene adsorbes on Cu(111) in the *trans* tautomeric state and can be observed stable at low bias voltages at 5 K. The porphycene molecule can be converted to the *cis* state by vibrational excitation via an inelastic electron tunneling process at bias voltages greater than 160 meV. Additionally a reversible *cis* to *cis* tautomerization can also be induced with a threshold voltage of around 150 meV. The *cis* to *trans* backward reaction can be thermally induced by heating the substrate up to 36 K, and all *cis* molecules were switched back to the *trans* form by an activation energy of around 40 meV, indicating that the *trans* is the thermodynamically stable tautomer and the *cis* state is the metastable one. A reversible *cis* to *cis* tautomerization could also be induced thermally with an activation energy of around 35 meV. Interestingly, the backward *cis* to *trans* reaction did not occur via a vibrationally-(electron-)induced process, albeit the threshold voltage ( $\sim 150$  meV) is substantially higher than the estimated thermal barrier ( $\sim 40$  meV). The higher barrier for the vibrationally induced tautomerization indicates that the reaction coordinate is associated to a high frequency mode via anharmonic coupling. Such an anharmonic coupling to a high frequency is known to be able to influence a reaction process decisively [115]. Further explanation of

these mechanism would require the identification of the STM-excited vibrational modes via inelastic electron tunneling (i.e. electron-phonon coupling) and molecular dynamics simulations that take into account the multi-dimensional nature of the potential landscape and anharmonic mode coupling.

Furthermore, electron-induced tautomerization can be induced not only in molecules underneath the STM tip, i.e. the injection point of tunneling electrons, but also in the distance of several tens of  $nm$ . Tip-surface distance dependent measurements next to step edges and above conductive defects revealed that the nonlocal process is induced by hot-carriers traveling along the surface. The reaction rate was found to be much smaller for hot holes than for hot electrons since the latter can travel efficiently via the surface state of Cu(111). The adsorbed porphycene molecules interact with the Cu surface state, leading to a coverage dependent tautomerization efficiency for the nonlocal process. At low molecular coverage the adsorption behavior is affected by the surface state and the intermolecular distance exhibits a preferable value determined by the surface state mediated interaction and a higher tautomerization rate was observed. At molecular coverages higher than around  $0.1\text{ nm}^{-2}$ , the molecules can not fulfill the optimized distances and adsorb with maximal possible molecular separation. At these coverages no scattering pattern of the surface state can be observed between the molecules in the STM image.  $dI/dV$  spectroscopy revealed the quenching of the surface state due to the high molecular coverage and the tautomerization efficiency became significantly lower for high molecular coverage than for low molecular coverage.

The coverage dependence of the tautomerization efficiency demonstrated the correlation of the Cu(111) surface state and the hot carrier transportation and we envision a possibility to engineer the Cu(111) surface state and the hot carrier transport locally by using the molecule-surface interactions. These results provide an insight into the mechanisms of hot carrier-induced chemical excitation processes on surfaces. These mechanisms can also be beneficial for a further understanding of other chemical reaction processes, which involve hot-carriers traveling via the surface and inducing a reaction, as e.g. in photochemistry on surfaces, where hot carriers are induced by photons.

The force-induced tautomerization of a single porphycene molecule on a Cu(110) surface was investigated using NC-AFM. A reversible *cis* to *cis* tautomerization can be induced merely by bringing a metallic tip close to a molecule even at  $5\text{ K}$  and zero bias voltage, thus in the absence of sufficient thermal energy and energetic tunneling electrons. Force spectroscopy was used to quantify

---

the tip-molecule interactions during the tip approach and retraction. The force spectra showed a sudden jump to more attractive interaction when the tautomerization occurs and the threshold energy varied in the range of 230 – 630 meV examined for 21 different tip apex conditions. This variation is most probably due to different tip apex geometry on the atomic scale. Three dimensional force mapping revealed that the tautomerization can be induced over the amine (NH) sides of the porphycene leaving imine (N) sides under the tip after the tautomerization. The force map resolved the tip-molecule interactions at sub-Ångström spatial resolution and showed the strongest interaction above the N sides of the inner cavity as well as local interaction maxima above the NH sides. The favorable tautomeric state during the tip approach was found in the energy gain of the system, which corresponds to the difference of the potential curves before and after a tautomerization event. The evolution of the energy gain shows a position dependence within the molecule. At the outer side of the porphycene, the favorable tautomeric state changes depending on the tip height. The initial state is favorable at large tip-sample distances, while it is inverted at short tip-sample distances and the system gains energy due to the tautomerization (note that at very long distances the initial and final state have the same potential energy). However, a different behavior was observed at the inner side of the molecule; the energy gain increases monotonously and the final state stays more stable than the initial state. Moreover, it was revealed that the tautomerization could not be induced with a Xe terminated tip. For the Xe terminated tip the interaction strength is weaker than that for a Cu tip and the Xe atom starts to bend reversible at very small tip-sample distances. This result demonstrates the importance of the chemical nature of the tip apex. Simulated force curves based on DFT calculations showed a good agreement to the experimental results; strongest interactions over the N sides as well as strong interactions over the NH sides of the inner cavity of the porphycene molecule and the position dependent energy gain. MEPs calculated by the NEB method predicted a step wise tautomerization via an intermediate *trans* state. The N-H stretching mode observed in the  $dI/dV$  spectra exhibited a significant red-shift upon tip approach, indicating the weakening of the NH bonds and a strengthening of the hydrogen bonds in the molecular cavity. These observations are supported by simulations and the increase of the NH bond length upon tip approach. The hydrogen bond strength in the inner cavity of the porphycene is associated with the tautomerization barrier and rate [50]. Therefore, the stronger hydrogen bonds should result in a lowering of the tautomerization barrier. This picture was confirmed by the DFT calcu-

lations and the MEP of the tautomerization showed that the approaching tip distorts the potential landscape and reduces the tautomerization barrier at close tip-sample distance. The DFT calculations for the Xe terminated tip revealed that the interaction strengths for the Xe tip are significantly smaller than for the Cu tip. Additionally, the Xe atom move around at the tip apex at close tip-sample distances. The MEP simulations showed that the Xe atom is in the way for the tautomerization, which leads to a complex and long MEP for a potential tautomerization with a high tautomerization barrier which even exceeds the one in the absence of a tip.

These results show the capability of inducing tautomerization merely by approaching an atomically sharp tip on a specific side over the molecule and demonstrate the role and importance of the chemical nature of the tip. Furthermore, these studies give an insight into the mechanisms that appear at the atomic scale during a force-induced chemical bond rearrangement and give an exemplary procedure to investigate force induced chemical reactions. The reduction of the reaction barrier by the approaching tip invokes a catalytic process. The absence of the the chemical process in presence of a Xe terminated tip demonstrates the capability to investigate the catalytic properties of a specific tip termination. The SPM tip termination with a variety of atoms/molecules is a well-established technique [59, 157–162] which could be used to investigate the interaction forces and capabilities to induce a chemical reaction in a systematic way. This could lead to a further understanding and control of the mechanisms of a catalytic process on the atomic scale.

# Bibliography

- [1] Asuka Ohshima, Atsuya Momotake, and Tatsuo Arai. Photochromism, thermochromism, and solvatochromism of naphthalene-based analogues of salicylideneaniline in solution. *Journal of Photochemistry and Photobiology A: Chemistry*, 162(2-3):473 – 479, 2004.
- [2] L. Claisen. Beiträge zur Kenntniss der 1,3 - Diketone und verwandter Verbindungen. *Justus Liebigs Annalen der Chemie*, 291(1-2):25–137, 1896.
- [3] Liudmil Antonov. *Tautomerism, Methods and Theories*. Wiley-VCH Verlag GmbH & Co. KGaA, 2014.
- [4] Liudmil Antonov. *Tautomerism, Concepts and Applications in Science and Technology*. Wiley-VCH Verlag GmbH & Co. KGaA, 2014.
- [5] J. D. Watson and F. H. C. Crick. Genetical implications of the structure of deoxyribonucleic acid. *Nature*, 171(4361):964–967, 1953.
- [6] Michael D. Topal and Jacques R. Fresco. Complementary base pairing and the origin of substitution mutations. *Nature*, 263(5575):285–289, 1976.
- [7] A.R. Morgan. Base mismatches and mutagenesis: how important is tautomerism? *Trends in Biochemical Sciences*, 18(5):160 – 163, 1993.
- [8] Victoria H. Harris, Clifford L. Smith, W. Jonathan Cummins, Alan L. Hamilton, Harry Adams, Mark Dickman, David P. Hornby, and David M. Williams. The Effect of Tautomeric Constant on the Specificity of Nucleotide Incorporation during {DNA} Replication: Support for the Rare Tautomer Hypothesis of Substitution Mutagenesis . *Journal of Molecular Biology*, 326(5):1389 – 1401, 2003.
- [9] Eric Westhof, Marat Yusupov, and Gulnara Yusupova. Recognition of Watson-Crick base pairs: constraints and limits due to geometric selection and tautomerism. *F1000Prime Reports*, 6:19, 2014.
- [10] Chenxu Zhu, Lining Lu, Jun Zhang, Zongwei Yue, Jinghui Song, Shuai Zong, Menghao Liu, Olivia Stovicek, Yi Qin Gao, and Chengqi Yi. Tautomerization-

- dependent recognition and excision of oxidation damage in base-excision DNA repair. *Proceedings of the National Academy of Sciences*, 113(28):7792–7797, 2016.
- [11] Pavel Pospisil, Patrick Ballmer, Leonardo Scapozza, and Gerd Folkers. Tautomerism in Computer-Aided Drug Design. *Journal of Receptors and Signal Transduction*, 23(4):361–371, 2003.
- [12] Alan R. Katritzky, C. Dennis Hall, Bahaa El-Dien M. El-Gendy, and Bogdan Draghici. Tautomerism in drug discovery. *Journal of Computer-Aided Molecular Design*, 24(6):475–484, 2010.
- [13] Z. Wojnarowska, P. Wlodarczyk, K. Kaminski, K. Grzybowska, L. Hawelek, and M. Paluch. On the kinetics of tautomerism in drugs: New application of broadband dielectric spectroscopy. *The Journal of Chemical Physics*, 133(9), 2010.
- [14] Deyu Li, Bogdan I. Fedeles, Vipender Singh, Chunte Sam Peng, Katherine J. Silvestre, Allison K. Simi, Jeffrey H. Simpson, Andrei Tokmakoff, and John M. Essigmann. Tautomerism provides a molecular explanation for the mutagenic properties of the anti-HIV nucleoside 5-aza-5,6-dihydro-2'-deoxycytidine. *Proceedings of the National Academy of Sciences*, 111(32):E3252–E3259, 2014.
- [15] Chunte Sam Peng, Bogdan I. Fedeles, Vipender Singh, Deyu Li, Tiffany Amariuta, John M. Essigmann, and Andrei Tokmakoff. Two-dimensional IR spectroscopy of the anti-HIV agent KP1212 reveals protonated and neutral tautomers that influence pH-dependent mutagenicity. *Proceedings of the National Academy of Sciences*, 112(11):3229–3234, 2015.
- [16] Sylwester Gawinkowski, Lukasz Walewski, Alexander Vdovin, Alkwin Slenczka, Stephane Rols, Mark R. Johnson, Bogdan Lesyng, and Jacek Waluk. Vibrations and hydrogen bonding in porphycene. *Phys. Chem. Chem. Phys.*, 14:5489–5503, 2012.
- [17] Sylwester Gawinkowski, Maria Pszona, Alexandr Gorski, Joanna Niedziolka-Jonsson, Izabela Kaminska, Wojciech Nogala, and Jacek Waluk. Single molecule Raman spectra of porphycene isotopologues. *Nanoscale*, 8:3337–3349, 2016.
- [18] Jacek Waluk and Emanuel Vogel.
- [19] R.M. Claramunt, C. López, M.D. Santa María, D. Sanz, and J. Elguero. The use of NMR spectroscopy to study tautomerism. *Progress in Nuclear Magnetic Resonance Spectroscopy*, 49(3-4):169–206, 2006.
- [20] J. R. Heath and M. A. Ratner. Molecular Electronics. *Physics Today*, 56(5):43–49, 2003.



- 
- [21] Peter Liljeroth, Jascha Repp, and Gerhard Meyer. Current-Induced Hydrogen Tautomerization and Conductance Switching of Naphthalocyanine Molecules. *Science*, 317(5842):1203–1206, 2007.
- [22] Alexander Sperl, Jörg Kröger, and Richard Berndt. Controlled Metalation of a Single Adsorbed Phthalocyanine. *Angewandte Chemie International Edition*, 50(23):5294–5297, 2011.
- [23] Willi Auwarter, Knud Seufert, Felix Bischoff, David Eciya, Saranyan Vijayaraghavan, Sushobhan Joshi, Florian Klappenberger, Niveditha Samudrala, and Johannes V. Barth. A surface-anchored molecular four-level conductance switch based on single proton transfer. *Nat Nano*, 7(1):41–46, 2012.
- [24] Takashi Kumagai, Felix Hanke, Sylwester Gawinkowski, John Sharp, Konstantinos Kotsis, Jacek Waluk, Mats Persson, and Leonhard Grill. Thermally and Vibrationally Induced Tautomerization of Single Porphycene Molecules on a Cu(110) Surface. *Phys. Rev. Lett.*, 111:246101, 2013.
- [25] Takashi Kumagai, Felix Hanke, Sylwester Gawinkowski, John Sharp, Konstantinos Kotsis, Jacek Waluk, Mats Persson, and Leonhard Grill. Controlling intramolecular hydrogen transfer in a porphycene molecule with single atoms or molecules located nearby. *Nat Chem*, 6(1):41–46, 2014.
- [26] Emanuel Vogel, Matthias Köcher, Hans Schmickler, and Johann Lex. Porphycene - a Novel Porphin Isomer. *Angewandte Chemie International Edition in English*, 25(3):257–259, 1986.
- [27] P. Fita, N. Urbańska, C. Radzewicz, and J. Waluk. Ground- and Excited-State Tautomerization Rates in Porphycenes. *Chemistry - A European Journal*, 15(19):4851–4856, 2009.
- [28] Juergen Braun, Martin Koecher, Martin Schlabach, Bernd Wehrle, Han-Heinrich Limbach, and Emanuel Vogel. NMR Study of the Tautomerism of Porphyrin Including the Kinetic HH/HD/DD Isotope Effects in the Liquid and the Solid State. *Journal of the American Chemical Society*, 116(15):6593–6604, 1994.
- [29] H. Böckmann, S. Liu, J. Mielke, S. Gawinkowski, J. Waluk, L. Grill, M. Wolf, and T. Kumagai. Direct Observation of Photoinduced Tautomerization in Single Molecules at a Metal Surface. *Nano Letters*, 16(2):1034–1041, 2016.
- [30] B. C. Stipe, M. A. Rezaei, and W. Ho. Atomistic studies of O<sub>2</sub> dissociation on Pt(111) induced by photons, electrons, and by heating. *The Journal of Chemical Physics*, 107(16), 1997.

## Bibliography

---

- [31] Peter Maksymovych, Daniel B. Dougherty, X.-Y. Zhu, and John T. Yates. Nonlocal Dissociative Chemistry of Adsorbed Molecules Induced by Localized Electron Injection into Metal Surfaces. *Phys. Rev. Lett.*, 99:016101, 2007.
- [32] Lan Chen, Hui Li, and Andrew Thye Shen Wee. Nonlocal Chemical Reactivity at Organic-Metal Interfaces. *ACS Nano*, 3(11):3684–3690, 2009.
- [33] Jae Ryang Hahn, Sang Hoon Jang, Ki Wan Kim, and Seung Bae Son. Hot carrier-selective chemical reactions on Ag(110). *The Journal of Chemical Physics*, 139(7), 2013.
- [34] P. O. Gartland and B. J. Slagsvold. Transitions conserving parallel momentum in photoemission from the (111) face of copper. *Phys. Rev. B*, 12:4047–4058, 1975.
- [35] P. Müller. Glossary of terms used in physical organic chemistry (IUPAC Recommendations 1994). *Pure and Applied Chemistry*, 66(5):1077–1184, 1994.
- [36] G. V. Nazin, X. H. Qiu, and W. Ho. Visualization and Spectroscopy of a Metal-Molecule-Metal Bridge. *Science*, 302(5642):77–81, 2003.
- [37] Yuji Okawa and Masakazu Aono. Materials science: Nanoscale control of chain polymerization. *Nature*, 409(6821):683–684, 2001.
- [38] Daisuke Takajo, Yuji Okawa, Tsuyoshi Hasegawa, and Masakazu Aono. Chain Polymerization of Diacetylene Compound Multilayer Films on the Topmost Surface Initiated by a Scanning Tunneling Microscope Tip. *Langmuir*, 23(10):5247–5250, 2007.
- [39] Yuji Okawa, Swapan K. Mandal, Chunping Hu, Yoshitaka Tateyama, Stefan Goedecker, Shigeru Tsukamoto, Tsuyoshi Hasegawa, James K. Gimzewski, and Masakazu Aono. Chemical Wiring and Soldering toward All-Molecule Electronic Circuitry. *Journal of the American Chemical Society*, 133(21):8227–8233, 2011.
- [40] Martin Wolf and Petra Tegeder. Reversible molecular switching at a metal surface: A case study of tetra-tert-butyl-azobenzene on Au(111) . *Surface Science*, 603(10-12):1506–1517, 2009.
- [41] J. Prasongkit, A. Grigoriev, R. Ahuja, and G. Wendin. Interference effects in phtalocyanine controlled by H-H tautomerization: Potential two-terminal unimolecular electronic switch. *Phys. Rev. B*, 84:165437, 2011.
- [42] Sherif Abdulkader Tawfik, X. Y. Cui, S. P. Ringer, and C. Stampfl. High on/off conductance switching ratio via h-tautomerization in quinone. *Journal of Chemical Theory and Computation*, 11(9):4154–4158, 2015.

- 
- [43] Daijiro Nozaki, Lokamani, Alejandro Santana-Bonilla, Arezoo Dianat, Rafael Gutierrez, and Gianaurelio Cuniberti. Switchable Negative Differential Resistance Induced by Quantum Interference Effects in Porphyrin-based Molecular Junctions. *The Journal of Physical Chemistry Letters*, 6(19):3950–3955, 2015.
- [44] Jing Zeng, Ke-Qiu Chen, and Mengqiu Long. Hydrogen tautomerization: A simple approach to tune spin-filtering effects in a quinone-based spintronic device. *Organic Electronics*, 35:12 – 16, 2016.
- [45] Uwe Langer, Christof Hoelger, Bernd Wehrle, Lidia Latanowicz, Emanuel Vogel, and Hans-Heinrich Limbach.  $^{15}\text{N}$  NMR study of proton localization and proton transfer thermodynamics and kinetics in polycrystalline porphycene. *Journal of Physical Organic Chemistry*, 13(1):23–34, 2000.
- [46] Lawrence E. Webb and Everly B. Fleischer. Crystal Structure of Porphine. *The Journal of Chemical Physics*, 43(9), 1965.
- [47] Pawel M. Kozlowski, Marek Z. Zgierski, and Jon Baker. The inner-hydrogen migration and ground-state structure of porphycene. *The Journal of Chemical Physics*, 109(14), 1998.
- [48] Yun-Dong Wu, Kyle W. K. Chan, Cong-Ping Yip, Emanuel Vogel, Dietmar A. Plattner, and K. N. Houk. Porphyrin Isomers: Geometry, Tautomerism, Geometrical Isomerism, and Stability. *The Journal of Organic Chemistry*, 62(26):9240–9250, 1997.
- [49] Karsten Malsch and Georg Hohlneicher. The Force Field of Porphycene: A Theoretical and Experimental Approach. *The Journal of Physical Chemistry A*, 101(45):8409–8416, 1997.
- [50] Piotr Ciąćka, Piotr Fita, Arkadiusz Listkowski, Michał Kijak, Santi Nonell, Daiki Kuzuhara, Hiroko Yamada, Czesław Radzewicz, and Jacek Waluk. Tautomerism in Porphycenes: Analysis of Rate-Affecting Factors. *The Journal of Physical Chemistry B*, 119(6):2292–2301, 2015.
- [51] G. Binnig, H. Rohrer, Ch. Gerber, and E. Weibel. Surface Studies by Scanning Tunneling Microscopy. *Phys. Rev. Lett.*, 49(1):57–61, 1982.
- [52] Bert Voigtländer. *Scanning Probe Microscopy*. Springer-Verlag Berlin Heidelberg, first edition, 2015.
- [53] G. Binnig, H. Rohrer, Ch. Gerber, and E. Weibel.  $7 \times 7$  Reconstruction on Si(111) Resolved in Real Space. *Phys. Rev. Lett.*, 50:120–123, 1983.

## Bibliography

---

- [54] Franz J. Giessibl. Atomic Resolution of the Silicon (111)-(7×7) Surface by Atomic Force Microscopy. *Science*, 267(5194):68–71, 1995.
- [55] B. C. Stipe, M. A. Rezaei, and W. Ho. Single-Molecule Vibrational Spectroscopy and Microscopy. *Science*, 280(5370):1732–1735, 1998.
- [56] Yoshiaki Sugimoto, Pavel Jelinek, Pablo Pou, Masayuki Abe, Seizo Morita, Ruben Perez, and Oscar Custance. Mechanism for Room-Temperature Single-Atom Lateral Manipulations on Semiconductors using Dynamic Force Microscopy. *Phys. Rev. Lett.*, 98:106104, 2007.
- [57] D. M. Eigler and E. K. Schweizer. Positioning single atoms with a scanning tunnelling microscope. *Nature*, 344(6266):524–526, 1990.
- [58] M. F. Crommie, C. P. Lutz, and D. M. Eigler. Confinement of Electrons to Quantum Corrals on a Metal Surface. *Science*, 262(5131):218–220, 1993.
- [59] L. Bartels, G. Meyer, and K.-H. Rieder. Basic Steps of Lateral Manipulation of Single Atoms and Diatomic Clusters with a Scanning Tunneling Microscope Tip. *Phys. Rev. Lett.*, 79:697–700, 1997.
- [60] Noriaki Oyabu, Óscar Custance, Insook Yi, Yasuhiro Sugawara, and Seizo Morita. Mechanical Vertical Manipulation of Selected Single Atoms by Soft Nanoindentation Using Near Contact Atomic Force Microscopy. *Phys. Rev. Lett.*, 90:176102, 2003.
- [61] Yoshiaki Sugimoto, Masayuki Abe, Shinji Hirayama, Noriaki Oyabu, Oscar Custance, and Seizo Morita. Atom inlays performed at room temperature using atomic force microscopy. *Nat Mater*, 4(2):156–159, 2005.
- [62] J. Tersoff and D. R. Hamann. Theory and Application for the Scanning Tunneling Microscope. *Phys. Rev. Lett.*, 50:1998–2001, 1983.
- [63] J. Tersoff and D. R. Hamann. Theory of the scanning tunneling microscope. *Phys. Rev. B*, 31:805–813, 1985.
- [64] J. Bardeen. Tunnelling from a Many-Particle Point of View. *Phys. Rev. Lett.*, 6:57–59, 1961.
- [65] A. Selloni, P. Carnevali, E. Tosatti, and C. D. Chen. Voltage-dependent scanning-tunneling microscopy of a crystal surface: Graphite. *Phys. Rev. B*, 31:2602–2605, 1985.
- [66] B. C. Stipe, M. A. Rezaei, and W. Ho. Inducing and Viewing the Rotational Motion of a Single Molecule. *Science*, 279(5358):1907–1909, 1998.

- 
- [67] B. C. Stipe, M. A. Rezaei, and W. Ho. Coupling of Vibrational Excitation to the Rotational Motion of a Single Adsorbed Molecule. *Phys. Rev. Lett.*, 81:1263–1266, 1998.
- [68] Y. Kim, K. Motobayashi, T. Frederiksen, H. Ueba, and M. Kawai. Action spectroscopy for single-molecule reactions - Experiments and theory. *Progress in Surface Science*, 90(2):85 – 143, 2015.
- [69] G. Binnig, C. F. Quate, and Ch. Gerber. Atomic Force Microscope. *Phys. Rev. Lett.*, 56:930–933, 1986.
- [70] Franz J. Giessibl. Advances in atomic force microscopy. *Rev. Mod. Phys.*, 75:949–983, 2003.
- [71] S. Morita, R. Wiesendanger, and E. Meyer. *Noncontact Atomic Force Microscopy*. Springer Berlin Heidelberg, Berlin, Heidelberg, 2002.
- [72] Seizo Morita, Franz J. Giessibl, and Roland Wiesendanger. *Noncontact Atomic Force Microscopy: Volume 2*. Springer Berlin Heidelberg, Berlin, Heidelberg, 2009.
- [73] Seizo Morita, Franz J. Giessibl, Ernst Meyer, and Roland Wiesendanger. *Noncontact Atomic Force Microscopy: Volume 3*. Springer International Publishing, Berlin, Heidelberg, 2015.
- [74] Philip M. Morse. Diatomic Molecules According to the Wave Mechanics. II. Vibrational Levels. *Phys. Rev.*, 34:57–64, 1929.
- [75] J. E. Jones. On the Determination of Molecular Fields. II. From the Equation of State of a Gas. *Proceedings of the Royal Society of London A: Mathematical, Physical and Engineering Sciences*, 106(738):463–477, 1924.
- [76] Teik-Cheng Lim. Long range relationship between Morse and Lennard-Jones potential energy functions. *Molecular Physics*, 105(8):1013–1018, 2007.
- [77] Jacob Israelachvili. *Intermolecular & Surface Forces*. Academic Press Limited, London, second edition, 1991.
- [78] F. London. The general theory of molecular forces. *Trans. Faraday Soc.*, 33:8b–26, 1937.
- [79] H.C. Hamaker. The London-van der Waals attraction between spherical particles. *Physica*, 4(10):1058 – 1072, 1937.
- [80] E. Meyer, H. Heinzelmann, H. Rudin, and H. J. Güntherodt. Atomic resolution on LiF (001) by atomic force microscopy. *Zeitschrift für Physik B Condensed Matter*, 79(1):3–4, 1990.

- [81] E. Meyer, H. Heinzelmann, D. Brodbeck, G. Overney, R. Overney, L. Howald, H. Hug, T. Jung, H.-R. Hidber, and H.-J. Güntherodt. Atomic resolution on the surface of LiF(100) by atomic force microscopy. *Journal of Vacuum Science & Technology B*, 9(2), 1991.
- [82] Gerhard Meyer and Nabil M. Amer. Optical-beam-deflection atomic force microscopy: The NaCl (001) surface. *Applied Physics Letters*, 56(21), 1990.
- [83] F. Ohnesorge and G. Binnig. True Atomic Resolution by Atomic Force Microscopy Through Repulsive and Attractive Forces. *Science*, 260(5113):1451–1456, 1993.
- [84] Franz J. Giessibl. Atomic resolution on Si(111)-(7×7) by noncontact atomic force microscopy with a force sensor based on a quartz tuning fork. *Applied Physics Letters*, 76(11), 2000.
- [85] Franz J. Giessibl. Forces and frequency shifts in atomic-resolution dynamic-force microscopy. *Phys. Rev. B*, 56:16010–16015, 1997.
- [86] John E. Sader and Suzanne P. Jarvis. Accurate formulas for interaction force and energy in frequency modulation force spectroscopy. *Applied Physics Letters*, 84(10), 2004.
- [87] Hudlet, S., Saint Jean, M., Guthmann, C., and Berger, J. Evaluation of the capacitive force between an atomic force microscopy tip and a metallic surface. *Eur. Phys. J. B*, 2(1):5–10, 1998.
- [88] Lord Kelvin, G.C.V.O., D.C.L., LL.D., F.R.S., and M.R.I. V. Contact electricity of metals. *Philosophical Magazine Series 5*, 46(278):82–120, 1898.
- [89] Scienta Omicron GmbH. *Omicron Low Temperature SPM*. <http://www.scientaomicron.com/en/products/low-temperature-spm/instrument-concept>. Visited 22. Aug. 2016.
- [90] SPECS Zurich GmbH. *Nanonis Control Systems*. <http://www.specs-zurich.com/en/SPM-Control-System.html>. Visited 22. Aug. 2016.
- [91] A. Roth. *Vacuum Technology*. North-Holland Publishing Company, 1976.
- [92] Nigel S. Harris. *Modern Vacuum Practice*. McGRAW-HILL Book Company (UK) Limited, 1989.
- [93] A. Chambers, R. K. Fitch, and B.S. Halliday. *Basic Vacuum Technology*. IOP Publishing Ltd, 1989.
- [94] John F. O’Hanlon. *A User’s Guide to Vacuum Technology*. John Wiley & Sons, Inc., third edition, 2003.

- 
- [95] Karl Jousten. *Handbook of Vacuum Technology*. WILEY-VCH Verlag GmbH & Co., 2008.
- [96] Franz J. Giessibl. *Principles and Applications of the qPlus Sensor*; In: Seizo Morita, Franz J. Giessibl, and Roland Wiesendanger. *Noncontact Atomic Force Microscopy: Volume 2*, pages 121–142. Springer Berlin Heidelberg, Berlin, Heidelberg, 2009.
- [97] Boris J. Albers, Marcus Liebmann, Todd C. Schwendemann, Mehmet Z. Baykara, Markus Heyde, Miquel Salmeron, Eric I. Altman, and Udo D. Schwarz. Combined low-temperature scanning tunneling/atomic force microscope for atomic resolution imaging and site-specific force spectroscopy. *Review of Scientific Instruments*, 79(3), 2008.
- [98] Zsolt Majzik, Martin Setvín, Andreas Bettac, Albrecht Feltz, Vladimír Cháb, and Pavel Jelínek. Simultaneous current, force and dissipation measurements on the Si(111)  $7\times 7$  surface with an optimized qPlus AFM/STM technique. *Beilstein Journal of Nanotechnology*, 3:249–259, 2012.
- [99] Jan Berger, Martin Švec, Martin Müller, Martin Ledinský, Antonín Fejfar, Pavel Jelínek, and Zsolt Majzik. Characterization of the mechanical properties of qPlus sensors. *Beilstein Journal of Nanotechnology*, 4:1–9, 2013.
- [100] MaTecK GmbH. *Metal single crystals*. <http://www.mateck.de/index.php?lang=en&Itemid=7>. Visited 22. Aug. 2016.
- [101] Micol Alemani, Maike V. Peters, Stefan Hecht, Karl-Heinz Rieder, Francesca Moresco, , and Leonhard Grill. Electric Field-Induced Isomerization of Azobenzene by STM. *Journal of the American Chemical Society*, 128(45):14446–14447, 2006.
- [102] C. Silien, N. Liu, , W. Ho, J. B. Maddox, S. Mukamel, B. Liu, , and G. C. Bazan. Reversible Switching among Three Adsorbate Configurations in a Single [2.2]Paracyclophane-Based Molecule. *Nano Letters*, 8(1):208–213, 2008.
- [103] P. A. Sloan, S. Sakulsermsuk, and R. E. Palmer. Nonlocal Desorption of Chlorobenzene Molecules from the Si(111)-( $7\times 7$ ) Surface by Charge Injection from the Tip of a Scanning Tunneling Microscope: Remote Control of Atomic Manipulation. *Phys. Rev. Lett.*, 105:048301, 2010.
- [104] A. Bellec, D. Riedel, G. Dujardin, O. Boudrioua, L. Chaput, L. Stauffer, and Ph. Sonnet. Nonlocal Activation of a Bistable Atom through a Surface State Charge-Transfer Process on Si(100)-( $2\times 1$ ):**H**. *Phys. Rev. Lett.*, 105:048302, 2010.

- [105] B.N.J. Persson and Ph. Avouris. The effects of the electric field in the STM on excitation localization. Implications for local bond breaking. *Chemical Physics Letters*, 242(4-5):483 – 489, 1995.
- [106] Ph. Avouris, R.E. Walkup, A.R. Rossi, H.C. Akpati, P. Nordlander, T.-C. Shen, G.C. Abeln, and J.W. Lyding. Breaking individual chemical bonds via STM-induced excitations. *Surface Science*, 363(1-3):368 – 377, 1996.
- [107] M. Cranney, A.J. Mayne, A. Laikhtman, G. Comtet, and G. Dujardin. STM excitation of individual biphenyl molecules on Si(100) surface: DIET or DIEF? *Surface Science*, 593(1-3):139 – 146, 2005.
- [108] M. A. Rezaei, B. C. Stipe, and W. Ho. Atomically resolved adsorption and scanning tunneling microscope induced desorption on a semiconductor: NO on Si(111)-(7×7). *The Journal of Chemical Physics*, 110(10):4891–4896, 1999.
- [109] J. I. Pascual, A. Dick, M. Hansmann, H.-P. Rust, J. Neugebauer, and K. Horn. Bulk Electronic Structure of Metals Resolved with Scanning Tunneling Microscopy. *Phys. Rev. Lett.*, 96:046801, 2006.
- [110] Jascha Repp, Francesca Moresco, Gerhard Meyer, Karl-Heinz Rieder, Per Hyldgaard, and Mats Persson. Substrate Mediated Long-Range Oscillatory Interaction between Adatoms: Cu /Cu(111). *Phys. Rev. Lett.*, 85:2981–2984, 2000.
- [111] S.Å. Lindgren, J. Paul, and L. Walldén. Surface state energy shifts by molecular adsorption: CO on clean and Na covered Cu(111). *Surface Science*, 117(1-3):426–433, 1982.
- [112] Felix Bischoff, Knud Seufert, Willi Auwärter, Sushobhan Joshi, Saranyan Vijayaraghavan, David Écija, Katharina Diller, Anthoula C. Papageorgiou, Sybille Fischer, Francesco Allegretti, David A. Duncan, Florian Klappenberger, Florian Blobner, Runyuan Han, and Johannes V. Barth. How Surface Bonding and Repulsive Interactions Cause Phase Transformations: Ordering of a Prototype Macrocyclic Compound on Ag(111). *ACS Nano*, 7(4):3139–3149, 2013.
- [113] Wheeler P. Davey. Precision Measurements of the Lattice Constants of Twelve Common Metals. *Phys. Rev.*, 25:753–761, 1925.
- [114] Jacek Waluk, Monika Muller, Petra Swiderek, Matthias Kocher, Emanuel Vogel, Georg Hohlneicher, and Josef Michl. Electronic states of porphycenes. *Journal of the American Chemical Society*, 113(15):5511–5527, 1991.
- [115] T. Komeda, Y. Kim, Maki Kawai, B. N. J. Persson, and H. Ueba. Lateral Hopping of Molecules Induced by Excitation of Internal Vibration Mode. *Science*, 295(5562):2055–2058, 2002.



- 
- [116] R. M. Feenstra. Electrostatic potential for a hyperbolic probe tip near a semiconductor. *Journal of Vacuum Science & Technology B*, 21(5), 2003.
- [117] C. J. Chen. *Introduction to Scanning Tunneling Microscopy*. Oxford University Press, second edition, 2007.
- [118] J. A. Knapp, F. J. Himpsel, and D. E. Eastman. Experimental energy band dispersions and lifetimes for valence and conduction bands of copper using angle-resolved photoemission. *Phys. Rev. B*, 19:4952–4964, 1979.
- [119] R. Temirov, S. Soubatch, A. Luican, and F. S. Tautz. Free-electron-like dispersion in an organic monolayer film on a metal substrate. *Nature*, 444(7117):350–353, 2006.
- [120] Geoffrey Rojas, Scott Simpson, Xumin Chen, Donna A. Kunkel, Justin Nitz, Jie Xiao, Peter A. Dowben, Eva Zurek, and Axel Enders. Surface state engineering of molecule-molecule interactions. *Phys. Chem. Chem. Phys.*, 14:4971–4976, 2012.
- [121] Per Hyldgaard and Mats Persson. Long-ranged adsorbate-adsorbate interactions mediated by a surface-state band. *Journal of Physics: Condensed Matter*, 12(1):L13, 2000.
- [122] N. Knorr, H. Brune, M. Epple, A. Hirstein, M. A. Schneider, and K. Kern. Long-range adsorbate interactions mediated by a two-dimensional electron gas. *Phys. Rev. B*, 65:115420, 2002.
- [123] Takashi Yokoyama, Tomonori Takahashi, Kazuteru Shinozaki, and Masakuni Okamoto. Quantitative Analysis of Long-Range Interactions between Adsorbed Dipolar Molecules on Cu(111). *Phys. Rev. Lett.*, 98:206102, 2007.
- [124] Martin K. Beyer and Hauke Clausen-Schaumann. Mechanochemistry: The Mechanical Activation of Covalent Bonds. *Chemical Reviews*, 105(8):2921–2948, 2005.
- [125] Peter G. Gillespie and Richard G. Walker. Molecular basis of mechanosensory transduction. *Nature*, 413(6852):194–202, 2001.
- [126] Charles R. Hickenboth, Jeffrey S. Moore, Scott R. White, Nancy R. Sottos, Jerome Baudry, and Scott R. Wilson. Biasing reaction pathways with mechanical force. *Nature*, 446(7134):423–427, 2007.
- [127] Douglas A. Davis, Andrew Hamilton, Jinglei Yang, Lee D. Cremer, Dara Van Gough, Stephanie L. Potisek, Mitchell T. Ong, Paul V. Braun, Todd J. Martinez, Scott R. White, Jeffrey S. Moore, and Nancy R. Sottos. Force-induced activation of covalent bonds in mechanoresponsive polymeric materials. *Nature*, 459(7243):68–72, 2009.

## Bibliography

---

- [128] Cheng-Hui Li, Chao Wang, Christoph Keplinger, Jing-Lin Zuo, Lihua Jin, Yang Sun, Peng Zheng, Yi Cao, Franziska Lissel, Christian Linder, Xiao-Zeng You, and Zhenan Bao. A highly stretchable autonomous self-healing elastomer. *Nat Chem*, 8(6):618–624, 2016.
- [129] Armando del Rio, Raul Perez-Jimenez, Ruchuan Liu, Pere Roca-Cusachs, Julio M. Fernandez, and Michael P. Sheetz. Stretching Single Talin Rod Molecules Activates Vinculin Binding. *Science*, 323(5914):638–641, 2009.
- [130] GU Lee, LA Chrisey, and RJ Colton. Direct measurement of the forces between complementary strands of DNA. *Science*, 266(5186):771–773, 1994.
- [131] Ch. Loppacher, M. Guggisberg, O. Pfeiffer, E. Meyer, M. Bammerlin, R. Lüthi, R. Schlittler, J. K. Gimzewski, H. Tang, and C. Joachim. Direct Determination of the Energy Required to Operate a Single Molecule Switch. *Phys. Rev. Lett.*, 90:066107, 2003.
- [132] Yoshiaki Sugimoto, Pablo Pou, Oscar Custance, Pavel Jelinek, Masayuki Abe, Ruben Perez, and Seizo Morita. Complex Patterning by Vertical Interchange Atom Manipulation Using Atomic Force Microscopy. *Science*, 322(5900):413–417, 2008.
- [133] Markus Ternes, Christopher P. Lutz, Cyrus F. Hirjibehedin, Franz J. Giessibl, and Andreas J. Heinrich. The Force Needed to Move an Atom on a Surface. *Science*, 319(5866):1066–1069, 2008.
- [134] Adam Sweetman, Sam Jarvis, Rosanna Danza, Joseph Bamidele, Subhashis Gangopadhyay, Gordon A. Shaw, Lev Kantorovich, and Philip Moriarty. Toggling Bistable Atoms via Mechanical Switching of Bond Angle. *Phys. Rev. Lett.*, 106:136101, 2011.
- [135] Shiro Yamazaki, Keisuke Maeda, Yoshiaki Sugimoto, Masayuki Abe, Vladimír Zobač, Pablo Pou, Lucia Rodrigo, Pingo Mutombo, Ruben Pérez, Pavel Jelínek, and Seizo Morita. Interplay between Switching Driven by the Tunneling Current and Atomic Force of a Bistable Four-Atom Si Quantum Dot. *Nano Letters*, 15(7):4356–4363, 2015.
- [136] G. Langewisch, J. Falter, H. Fuchs, and A. Schirmeisen. Forces During the Controlled Displacement of Organic Molecules. *Phys. Rev. Lett.*, 110:036101, 2013.
- [137] Shigeki Kawai, Matthias Koch, Enrico Gnecco, Ali Sadeghi, Rémy Pawlak, Thilo Glatzel, Jutta Schwarz, Stefan Goedecker, Stefan Hecht, Alexis Baratoff, Leonhard Grill, and Ernst Meyer. Quantifying the atomic-level mechanics of single long physisorbed molecular chains. *Proceedings of the National Academy of Sciences*, 111(11):3968–3972, 2014.

- 
- [138] Christian Lotze. *Fundamental Processes in Single Molecule Junctions - Interplay of Forces and Electronic Effects*. Dissertation at the Freie Universität Berlin, 2013. [http://www.diss.fu-berlin.de/diss/receive/FUDISS\\_thesis\\_000000096508](http://www.diss.fu-berlin.de/diss/receive/FUDISS_thesis_000000096508); Visited July 2016.
- [139] Han-Qing Mao, Na Li, Xi Chen, and Qi-Kun Xue. Mechanical properties of H<sub>2</sub>Pc self-assembled monolayers at the single molecule level by noncontact atomic force microscopy. *Journal of Physics: Condensed Matter*, 24(8):084004, 2012.
- [140] M. A. Lantz, H. J. Hug, R. Hoffmann, P. J. A. van Schendel, P. Kappenberger, S. Martin, A. Baratoff, and H.-J. Güntherodt. Quantitative Measurement of Short-Range Chemical Bonding Forces. *Science*, 291(5513):2580–2583, 2001.
- [141] Markus Ternes, César González, Christopher P. Lutz, Prokop Hapala, Franz J. Giessibl, Pavel Jelínek, and Andreas J. Heinrich. Interplay of Conductance, Force, and Structural Change in Metallic Point Contacts. *Phys. Rev. Lett.*, 106:016802, 2011.
- [142] Fabian Mohn, Leo Gross, and Gerhard Meyer. Measuring the short-range force field above a single molecule with atomic resolution. *Applied Physics Letters*, 99(5), 2011.
- [143] Yoshiaki Sugimoto, Ayhan Yurtsever, Masayuki Abe, Seizo Morita, Martin Ondráček, Pablo Pou, Ruben Pérez, and Pavel Jelínek. Role of Tip Chemical Reactivity on Atom Manipulation Process in Dynamic Force Microscopy. *ACS Nano*, 7(8):7370–7376, 2013.
- [144] D. M. Eigler, C. P. Lutz, and W. E. Rudge. An atomic switch realized with the scanning tunnelling microscope. *Nature*, 352(6336):600–603, 1991.
- [145] Juarez L. F. Da Silva, Catherine Stampfl, and Matthias Scheffler. Xe adsorption on metal surfaces: First-principles investigations. *Phys. Rev. B*, 72:075424, 2005.
- [146] G. Kresse and J. Furthmüller. Efficient iterative schemes for *ab initio* total-energy calculations using a plane-wave basis set. *Phys. Rev. B*, 54:11169–11186, 1996.
- [147] G. Kresse and D. Joubert. From ultrasoft pseudopotentials to the projector augmented-wave method. *Phys. Rev. B*, 59:1758–1775, 1999.
- [148] M. Dion, H. Rydberg, E. Schröder, D. C. Langreth, and B. I. Lundqvist. Van der Waals Density Functional for General Geometries. *Phys. Rev. Lett.*, 92:246401, 2004.
- [149] Guillermo Román-Pérez and José M. Soler. Efficient Implementation of a van der Waals Density Functional: Application to Double-Wall Carbon Nanotubes. *Phys. Rev. Lett.*, 103:096102, 2009.

- [150] Jiří Klimeš, David R Bowler, and Angelos Michaelides. Chemical accuracy for the van der Waals density functional. *Journal of Physics: Condensed Matter*, 22(2):022201, 2010.
- [151] Jiří Klimeš, David R. Bowler, and Angelos Michaelides. Van der Waals density functionals applied to solids. *Phys. Rev. B*, 83:195131, 2011.
- [152] Jens Falter, Marvin Stiefermann, Gernot Langewisch, Philipp Schurig, Hendrik Hölscher, Harald Fuchs, and André Schirmeisen. Calibration of quartz tuning fork spring constants for non-contact atomic force microscopy: direct mechanical measurements and simulations. *Beilstein Journal of Nanotechnology*, 5:507–516, 2014.
- [153] T. Kumagai, M. Kaizu, S. Hatta, H. Okuyama, T. Aruga, I. Hamada, and Y. Morikawa. Direct Observation of Hydrogen-Bond Exchange within a Single Water Dimer. *Phys. Rev. Lett.*, 100:166101, 2008.
- [154] Xiangzhi Meng, Jing Guo, Jinbo Peng, Ji Chen, Zhichang Wang, Jun-Ren Shi, Xin-Zheng Li, En-Ge Wang, and Ying Jiang. Direct visualization of concerted proton tunnelling in a water nanocluster. *Nat Phys*, 11(3):235–239, 2015.
- [155] Gregory Mills, Hannes Jónsson, and Gregory K. Schenter. Reversible work transition state theory: application to dissociative adsorption of hydrogen . *Surface Science*, 324(2-3):305 – 337, 1995.
- [156] Graeme Henkelman, Blas P. Uberuaga, and Hannes Jónsson. A climbing image nudged elastic band method for finding saddle points and minimum energy paths. *The Journal of Chemical Physics*, 113(22), 2000.
- [157] L. Bartels, G. Meyer, K.-H. Rieder, D. Velic, E. Knoesel, A. Hotzel, M. Wolf, and G. Ertl. Dynamics of Electron-Induced Manipulation of Individual CO Molecules on Cu(111). *Phys. Rev. Lett.*, 80:2004–2007, 1998.
- [158] H. J. Lee and W. Ho. Single-Bond Formation and Characterization with a Scanning Tunneling Microscope. *Science*, 286(5445):1719–1722, 1999.
- [159] Leo Gross, Fabian Mohn, Nikolaj Moll, Peter Liljeroth, and Gerhard Meyer. The Chemical Structure of a Molecule Resolved by Atomic Force Microscopy. *Science*, 325(5944):1110–1114, 2009.
- [160] Fabian Mohn, Bruno Schuler, Leo Gross, and Gerhard Meyer. Different tips for high-resolution atomic force microscopy and scanning tunneling microscopy of single molecules. *Applied Physics Letters*, 102(7), 2013.

- [161] Adam Sweetman, Samuel P. Jarvis, Philipp Rahe, Neil R. Champness, Lev Kantorovich, and Philip Moriarty. Intramolecular bonds resolved on a semiconductor surface. *Phys. Rev. B*, 90:165425, 2014.
- [162] Leo Gross, Bruno Schuler, Fabian Mohn, Nikolaj Moll, Niko Pavliček, Wolfram Steurer, Ivan Scivetti, Konstantinos Kotsis, Mats Persson, and Gerhard Meyer. Investigating atomic contrast in atomic force microscopy and Kelvin probe force microscopy on ionic systems using functionalized tips. *Phys. Rev. B*, 90:155455, 2014.

## Bibliography

---

## Publications

### Publications related to this thesis

- *Janina N. Ladenthin, Thomas Frederiksen, Mats Persson, John C. Sharp, Sylwester Gawinkowski, Jacek Waluk and Takashi Kumagai. **Force-induced tautomerization in a single molecule.** *Nature Chemistry*, 8(10): 935–940, 2016.*
- *Janina N. Ladenthin, Leonhard Grill, Sylwester Gawinkowski, Shuyi Liu, Jacek Waluk and Takashi Kumagai. **Hot Carrier-Induced Tautomerization within a Single Porphycene Molecule on Cu(111).** *ACS Nano*, 9(7): 7287-7295, 2015.*

### Publications not related to this thesis

- *Paul Stoll, Matthias Bernien, Daniela Rolf, Fabian Nickel, Qingyu Xu, Claudia Hartmann, Tobias R. Umbach, Jens Kopprasch, Janina N. Ladenthin, Enrico Schierle, Eugen Weschke, Constantin Czekelius, Wolfgang Kuch, and Katharina J. Franke. **Magnetic anisotropy in surface-supported single-ion lanthanide complexes.** *submitted 2016.**
- *T. R. Umbach, I. Fernandez-Torrente, J. N. Ladenthin, J. I. Pascual and K. J. Franke. **Enhanced charge transfer in a monolayer of the organic charge transfer complex TTF-TNAP on Au(111).** *Journal of Physics: Condensed Matter*, 24: 354003, 2012.*

## Presentations

- **DPG Spring Meeting** – Condensed Matter Section, Regensburg, Germany, 6. – 11.03.2015.  
Talk: Force-induced tautomerization in a single molecule.
- **UK-Japan Symposium on Atomic and Molecular Manipulation: Force and Tunnel Current in Scanning Probe Microscopy** University of Nottingham, UK, 15 – 16.12.2015.  
Talk: Force-induced tautomerization in a single molecule.
- **Seminar, Group of Prof. Hiroshi Okuyama** Kyoto University, Japan, 4.12.2015.  
Talk: Direct observation of intramolecular hydrogen transfer by using scanning probe microscopy.
- **Workshop "Surface Interface Spectroscopy 2015"**, Saitama, Japan, 27. – 28.2015.  
Poster: Force-Induced Tautomerization in a Single Molecule.  
*Winner of student prize.*
- **Seminar, Group of Prof. Maki Kawai**, The University of Tokyo, Japan, 25.11.2015.  
Talk: Direct observation of intramolecular hydrogen transfer by using scanning probe microscopy.
- **International workshop: "Theory, measurement and creation of porphyrinoid compounds as soft molecular systems"**, NIMS, Tsukuba, Japan, 1.10.2015.  
Talk: Hot Carrier-Induced Tautomerization within a Single Porphycene Molecule on Cu(111).
- **18th International Conference on non-contact Atomic Force Microscopy**, Cassis, France, 7. – 11.09.2015.  
Talk: Mechanically-induced Intramolecular H-atom Transfer Studied by nc-AFM.



- **The 15th International Conference on Vibrations at Surfaces**, Donostia-San Sebastián, Spain, 22. – 26.06.2015.  
Poster: Hot-carrier induced intramolecular H-atom transfer reaction studied by scanning tunneling microscopy.
- **Seminar, Group of Prof. Katharina J. Franke**, Freie Universität Berlin, Germany, 27.04.2015.  
Talk: Direct observation of intramolecular H-atom transfer reaction by scanning tunneling microscopy.
- **DPG Spring Meeting** – Condensed Matter Section, Berlin, Germany, 15. – 20.03.2015.  
Talk: Direct observation of intramolecular H-atom transfer reaction by scanning tunneling microscopy.
- **XXI International Summer School "Nicolas Cabrera"** – New Frontiers in Scanning Force Microscopy: From Ultrahigh-Vacuum to Biological Material, Madrid, Spain, 14.07. – 18.07.2014.  
Poster: Precise control of intermolecular H-atom reactions using scanning probe microscopy.  
*1. prize at the poster awards.*



## Acknowledgments

Firstly, I would like to thank my dissertation supervisor Prof. Martin Wolf for giving me the opportunity to do this dissertation research project in the Department of Physical Chemistry of the Fritz-Haber Institute. I also want to thank Prof. Katharina J. Franke for being my second supervisor and introducing me to SPM research.

I would like to express my deep gratitude to my group leader Takashi Kumagai for mentoring this research project in the Nanoscale Surface Chemistry Group, his invaluable academic guidance and always treating me as a colleague.

Further, I am grateful for the fruitful discussions about my research with Prof. Delroy A. Baugh and Prof. Leonhard Grill.

Thanks to my group colleagues, Hannes Böckmann, Stefan Böttcher, Matthias Koch, Shuyi Liu, Johannes Mielke, Christophe Nacci, Maria Pszona, Alex Saywell, Akitoshi Shiotari, and my other colleagues in the department for the great research environment.

Special thanks to Oscar Custance and Tomoko Shimizu for the opportunity to join their research in the Nanomechanics Group at National Institute for Materials Science in Tsukuba, Japan for three months and sharing their expert knowledge about AFM with me.

I want to thank Thomas Frederiksen, Sylwester Gawinkowski, Mats Persson, John C. Sharp, Jacek Waluk for the fruitful collaboration. Many thanks to Adam Sweetman for the valuable discussions about the AFM setup.

Thanks to Wibke Bronsch and Gero Thole for proofreading this thesis.

Last but not least, I would like to express all my gratitude to my family and friends for always supporting me.